Fluid Dynamic Assessment of Sensor Geometry For Micro System Applications

Mohamed Hassan

Ph.D. Thesis

In

The Department

of

Mechanical and Industrial Engineering

Presented in Partial Fulfillment of the Requirements

for the Degree of Doctor of Philosophy at

Concordia University

Montreal, Quebec, Canada

September, 2015

CONCORDIA UNIVERSITY

School of Graduate Studies

This is to certify that the thesis prepared

By: **Mohamed Hassan**

Entitled: **Fluid Dynamic Assessment of Sensor Geometry for Micro System Applications**

and submitted in partial fulfillment of the requirements for the degree of

Doctor of Philosophy

complies with the regulations of the University and meets the accepted standards with respect to originality and quality.

Signed by the examining committee:

---------- Dr. (chair)

---------- Dr. Metin Yaras (External Examiner)

---------- Dr. Samuel Li (Ext.-to-Program)

---------- Dr. Hoi Dick Ng (Examiner)

---------- Dr. Ion Stiharu (Examiner)

---------- Dr. Georgios Vatistas (Examiner)

---------- Dr. Wahid Ghaly (Supervisor)

Approved by ----------

Department Chair or Graduate Program Director

----------2015----------

Dean, Faculty of Engineering and Computer Science

ABSTRACT

Fluid Dynamic Assessment of Sensor Geometry for Micro System Applications

Mohamed Hassan, PhD.
Concordia University, 2015

In this work, the fluid dynamic behaviour around a proposed micro-sensor geometry is assessed. The sensor is intended for use in micro devices and is represented by two cubes (or elements) set in tandem. The flow is described by the Navier-Stokes equations and is solved by Direct Numerical Simulation (*DNS*) using *ANSYS-CFX*. Flow visualization using an existing experimental setup is carried out to visualize the flow pattern around the sensor using the soap film technique, where the flow is considered to be two-dimensional incompressible. This visualization is intended to verify the DNS that is carried out for the same cases. Results for the flow pattern and the vortex shedding frequency that are obtained from both numerical simulations and experimental investigations compare favorably, for three different values of Reynolds number, which verifies the numerical approach.

A parametric study on the effect of geometry in the limit of *2D* incompressible flow of water is carried out. This study shows that the inter-element spacing strongly affects the flow in the inter-element cavity; it also shows that the thickness of the downstream element affects the downstream shear layer. Both of these geometric parameters control the vortex shedding in the wake and the drag coefficient particularly on the downstream element. This parametric study also suggests that a 'general' linear correlation between Strouhal and Reynolds numbers (modified to include geometric parameters) is valid for all variables investigated in this work.

The DNS of air in the limit of *2D* and *3D* flow is considered at three subsonic inflow Mach numbers. The flow simulation results are verified against basic flow physics, available experimental data and interpretations of vortex shedding behaviour particularly in *3D* flow. For air flow in the *2D* limit, the vortex shedding frequency expressed in terms of Roshko number (rather than Strouhal number) correlates well with Reynolds number at

all Mach numbers. For both *2D* and *3D* flows, the vortex shedding frequency, flow behavior and drag coefficient compare reasonably well with available experimental data.

The drag coefficient and Strouhal number computed from *DNS* will serve as a first step towards inferring the flow pressure and velocity, when the proposed sensor is built. Hence achieving one of the main goals of this work.

DEDICATION

This thesis is dedicated to my mother, my wife and my children.

ACKNOWLEDGEMENTS

First and foremost, all praise be to Allah.

I gratefully and sincerely acknowledge the continued support, guidance and encouragement provided over the years by my supervisor Dr. Wahid Ghaly. He spent many hours helping and teaching me during the course of my PhD study at Concordia University. I thank him for all the lessons and precious advice provided throughout the research.

I would also like to thank the Egyptian Ministry of Defense for giving me the opportunity to go through my PhD study at Concordia University.

Moreover, I would like to thank all members of the MIE department, the faculty and staff for all the support and encouragement (and tolerance) they have shown towards me throughout the years of my tenure at Concordia.

Special thanks go to Dr. Mohamed Fayed for his consistent support in carrying out the experimental work.

Also great thanks to Dr. Vatistas and Dr. Ng for letting me use the lab and the instruments.

I would also like to thank my colleagues for having a good working environment and providing me with valuable assistance, encouragement and friendship; in particular, Raja Ramamurthy.

Finally, the ultimate acknowledgement is to my parents, my wife, my children and my sisters for their continuous and unending love, prayer and support.

TABLE OF CONTENTS

LIST OF FIGURES

LIST OF TABLES

LIST OF SYMBOLS

English Symbols:

a	Speed of sound	(m/s)
C_p	Specific heat at constant pressure	(kJ/Kg K)
C_v	Specific heat at constant volume	(kJ/Kg K)
C_m	Mean molecular velocity	(m/s)
C_d	Drag coefficient	(-)
d	Width of bluff body	(m)
f	Vortex shedding frequency	(Hz)
h	Cube side length	(m)
k	Turbulent kinetic energy	(m^2/s^2)
Kn	Knudsen number	(-)
M	Mach number	(-)
p	Pressure	(Pa)
R	Gas Constant	(kJ/Kg K)
Re	Reynolds number	(-)
Re^*	Unit Reynolds number	(-)
Re_M	Modified Reynolds number	(-)
Ro	Roshko number	(-)
S	Separation distance	(m)
S_E	A source of energy per unit volume per unit time	(Kg/m s^3)
S_M	A source of momentum per unit volume per unit time	(Kg/m^2 s^2)
St	Strouhal number	(-)
St_M	Modified Strouhal number	(-)
t	Time	(s)
t_η	Kolmogorov time scale	(s)
T	Temperature	(K)

U	Soap film velocity (i.e. Experimental main velocity)	(m/s)
u	Streamwise velocity component	(m/s)
v	Velocity component in y-direction	(m/s)
w	Crossflow velocity component	(m/s)
x	Distance	(m)
y	Distance	(m)
z	Distance	(m)

Greek Symbols:

μ	Dynamic viscosity of fluid	(Kg/m s)
γ	Ideal-gas specific heat ratio	(-)
δ	boundary layer thickness	(m)
η	Kolmogorov length scale	(m)
λ	Mean free path	(m)
ν	Kinematic viscosity of fluid	(m^2/s^2)
ρ	Density of fluid	(kg/m^3)
τ	Stress tensor	(N/m^2)
τ_m	Mean time between collisions	(s)

Superscripts:

$'$	Fluctuation around the mean value
$\bar{}$	Mean or ensemble average value

Subscripts:

∞	Far upstream
abs	Absolute
exp	Experimental
num	Numerical
sf	Soap film
tot	Total
τ	Friction

w	Water

Acronyms:

2D	Two-Dimensional
3D	Three-Dimensional
ACARE	Advisory Council for Aviation Research and Innovation in Europe
BE	Blocking element
CFD	Computational Fluid Dynamics
DES	Detached Eddy Simulation
DFT	Discrete Fourier Transform
DNS	Direct Numerical Simulation
EARSM	Explicit Algebraic Reynolds Stress Model
GTE	Gas Turbine Engine
LES	Large Eddy Simulation
LRR	Launder, Reece and Rodi Isotropization of Production model Reynolds Stress
QI	Launder, Reece and Rodi Quasi-Isotropic model Reynolds Stress
RANS	Reynolds Averaged Navier-Stokes
RMS	Root mean square
SE	Sensitive element
SiCN	Silicon Carbon-Nitride
SSG	Speziale, Sarkar and Gatski Reynolds Stress
TE	Trailing edge
URANS	Unsteady Reynolds Averaged Navier-Stokes

Chapter 1
INTRODUCTION AND LITERATURE REVIEW

1.1 Introduction

There are many applications in everyday life and in industry that involve fluid flow. In the past few decades, controlling fluid flow in order to achieve optimum performance in these applications, has become an area of interest for many researchers. Velocity, pressure and temperature are important parameters to describe the flow field. By measuring these parameters it is possible to determine the flow field to a high degree of accuracy and therefore to control it. Also due to the ever-increasing computational power, more flow field details are captured through numerical flow simulations. In the present work, micro fluid devices, the micro scale gas turbine engine and the gas turbine engine are the subject of interest for the writer. The gas turbine engine will be taken as an example to show how important it is to be able to have reliable flow measurements.

In this section, micro sensor applications will be discussed. Then the literature on velocity and pressure sensing will be presented.

1.1.1 Sensor applications

The main purpose of this work is to characterize the fluid flow around a new micro-sensor configuration that can potentially be used in the following three applications:

Micro fluid devices

Fluid flow through micro devices (i.e. small channels) has become a popular research topic due to the emergence of biochemical systems and micro electromechanical system (MEMS) fabrication technologies. Therefore it is important to measure the fluid flow

parameters inside these channels in order to obtain high performance operation. Examples of these devices include micro channel condensers, micro mixers and micro pumps.

Micro gas turbine

In the last few years, there have been many attempts to produce the micro scale gas turbine engine (*GTE*) and micro bipropellant regenerative rocket engine for use in military and space applications. To ensure that these applications are operating at optimum performance, the flow parameters need to be closely monitored using micro sensors.

Gas turbine engine

Fluid parameters are key to controlling any heat engine such as a gas turbine engine. The gas turbine engine is based on the Brayton cycle. The efficiency of each part in the *GTE* depends mainly on inlet and outlet temperature and pressure. In the last three decades there has been notable improvement in *GTE* efficiency, but in recent years it seems that a plateau has been reached in the latest generations of *GTE* (civil and military) due to physical limitations of the materials being used [1]. So what is the future of the *GTE*? The answer depends on what the needs are. *Advisory Council for Aviation Research and Innovation in Europe* (*ACARE*) summarizes future needs for civil air traffic as follows [1]:

- Reduce accident rate by *80%*.
- Achieve zero hijack success.
- Halve the time to market (by reducing operational costs).
- Reduce travel cost by reducing specific fuel consumption by *15%* to *20%*.
- Increase the movements of aircrafts by a factor of three.
- Reduce perceived noise by half, i.e. by about *10 dB* per operation.
- Reduce *NO* emissions by *80%*.
- Reduce CO_2 emissions by *50%*.

And, for future military engines [1]:

- Enable long-range strike missions.
- Combine efficiency for high altitude cruise and low altitude high-speed attack.

All these requirements can be achieved by building more intelligent *GTE*. This can be accomplished by using active control in the following *GTE* parts:

- Intake: control of flow separation.
- Fan: noise reduction, flow control, vibration.
- Compressor: flow control, surge margin improvement, tip leakage reduction.
- Combustor: combustion improvement, emissions.
- Turbines: cooling optimization, tip clearance leakage reduction, control flow.
- Exhaust / Afterburners: noise reduction, stability.
- Nozzle: flow control.

Active control can be performed by embedding mini or micro sensors and actuators to support an on board real time engine dynamic model which is used to monitor the engine health and adapt the engine control for optimum performance. But more sensors and actuators means more weight and cost. Using *MEM* sensors will reduce the weight and cost problems will be reduced. Questions remain regarding velocity and pressure sensing technology as well as the challenges for sensors operating within the gas path for example.

1.1.2 Background of velocity sensing

Flow velocity meters can be divided into two categories:

Measurement of local velocity

The meter measures the local velocity at a point in the fluid flow such as pitot static tube and hot wire anemometer.

Measurement of mean velocity

The meter measures the mean velocity over a finite flow area, such as cup anemometer, vane anemometer, current meter, turbine meter and reed anemometer. The vortex flow meter fits under this category and will be discussed later in this chapter.

1.1.3 Background of pressure sensing

There are two basic categories of analog pressure sensors.

Mechanical pressure sensors

These types of pressure sensors basically consist of two elements. The first element is a mechanical element (sensing element) such as a diaphragm, piston, plate, shell, tube, or

bellow. It is designed and constructed to deflect when pressure is applied. This is the basic mechanism converting pressure to physical movement. The second element (transducer element) is responsible for converting this movement to an electrical or other form of output. The second element can be one of the following types:

- Strain Gauge (Piezoresistive) Pressure Sensors

  Strain gauge sensors originally used strain gauges bonded to a metal diaphragm. A strain gauge measures the strain in a material subjected to applied stress. Semiconductor strain gauges are widely used, they are either bonded or integrated into a silicon diaphragm, because the response to applied stress is an order of magnitude larger than that of a metallic strain gauge. Generally [2], four strain gauges are connected to form a Wheatstone bridge configuration with a voltage excitation source to enhance the sensor sensitivity by maximizing the output voltage. Also, the small size of the sensing element means that it has a wide frequency response and may be used for dynamic pressure measurements without concern for errors (i.e. mechanical vibration and acceleration have a negligible effect). This is the most commonly employed sensing technology for general purpose pressure measurement. Generally, these technologies are suited to measure absolute, gauge, vacuum, and differential pressures.

- Capacitive Pressure Sensors

  This type of sensors uses a thin diaphragm and a pressure cavity to create a variable capacitor to detect strain due to applied pressure. Common technologies use metal, ceramic, and silicon diaphragms. Generally, these technologies are mostly used for low pressures (absolute, differential and gauge) because the device has to be fairly large to obtain a usable signal, frequency response. This may be a problem in some applications.

- Inductive (Electromagnetic) Pressure Sensors

  In this type, the displacement of a diaphragm due to applied pressure is measured by means of a change in inductance according to the eddy current principle.

- Piezoelectric Pressure Sensors

  Piezoelectric elements are bi-directional transducers capable of converting stress into an electric potential and vice versa. They consist of metalized quartz or ceramic

materials; they provide a pressure reading only when the input is changing with time. Therefore they are commonly employed in highly dynamic conditions.

- Optical Pressure Sensors

  Optical sensors depend on two principles:

  Firstly an optical sensor can measure the deflection of an elastic element such as a diaphragm or cantilever by detecting light reflected from that element.

  Secondly, optical fibers can be used as sensors to measure strain, temperature, pressure and other quantities by modifying a fiber so that the quantity to be measured modulates the intensity, phase, polarization, and wavelength or transit time of light in the fiber. Sensors that vary the intensity of light are the simplest, since only a simple light source and detector are required. Such sensors exhibit several useful features such as they have low power consumption, are highly remote, can operate in high temperatures, are inherently immune to electromagnetic interference, are highly sensitive, have a high frequency response, and are small in size. Optical sensors however suffer from temperature sensitivity problems [3] due to the thermal expansion and the shape changing of elastic element (sensitive element of pressure). Furthermore, aligning the optics and calibrating the sensors can be challenging and expensive. In addition, optical sensors need a clean environment which is not available in harsh environments (e.g. *GTE*).

- Potentiometric Pressure Sensor

  Potentiometric pressure sensors use a Bourdon tube, capsule, or bellows to drive a wiper arm on a resistive element. For reliable operation the wiper must bear on the element with some force, which leads to repeatability and hysteresis errors. These devices are very low cost, however, and are used in low-performance applications such as dashboard oil pressure gauges [4].

Other pressure sensors

Other pressure sensors detect the change in non-mechanical properties. There are numerous ways to derive pressure from other fluid properties such as speed of sound, mass, index of refraction, thermal conductivity, changes in resonant frequency and ionization.

1.1.4 Sensor challenges

Table 1.1, produced by Stiharu [5], summarizes the harsh environments and demanding requirements that sensors need to withstand.

Table 1.1: Sensor requirements [Stiharu, [5]].

Generic Sensor Requirements		
Sensed Variable	**Sensor Operation**	
	Environment	**Requirements**
Temperature	700 - 1700°C	± 5 C accuracy ,< 1 Hz bandwidth, resolution 5°C , 0-10 Hz bandwidth
Pressure	15 - 106 kPa, -60°C to +65°C	pres. +3 bar, res. ± 0.1%
	15 - 106 kPa, -60°C to +65°C	res. ± 0.25%, 500 Hz bandwidth
	15 - 1800 kPa, -60°C to 500°C	35 kPa dynamic, ± 0.2% resolution, 5 - 40 kHz bandwidth
	15 - 1800 kPa, -60°C to 700°C	
	15 - 1800 kPa, -60°C to 500°C	35 kPa dynamic, ± 0.5% resolution, 1 Hz bandwidth
	15 - 1800 kPa, -60°C to 700°C	
	300 - 4000 kPa, 700°C to 1700°C	10 kPa dynamic, ± 5% resolution, 1000 Hz bandwidth
Vibration (accelerometer)	15 - 300 kPa, -60°C to +65°C	3%, 40 kHz, 1000g range
	300 - 4000 kPa, 700°C to 1700°C	3%, 40 kHz, 1000g range
Emission Species	300 - 4000 kPa, 700°C to 1700°C	COx, NOx, 5% resolution, 5 Hz bandwidth
Tip Clearance	15 - 1800 kPa, -60°C to 700°C	2.5 mm range, 25 µm resolution, 50 kHz
	300 - 4000 kPa, 700°C to 1700°C	2.5 mm range, 25 µm resolution, 50 kHz
Flow	15 - 300 kPa, -60°C to +150°C	1% resolution, 1 ml/sec min. flow
Torque	15 - 300 kPa, -60°C to +150°C	10.000-20,000 Nm, 10 Hz
Position/Arrival time	15 - 1800 kPa, -60°C to 700°C	capacitive or inductive, 50 kHz bandwidth, resolution
Fuel Flow	300 - 4000 kPa, 700°C to 1700°C	1 % resolution, > 6 Hz bandwidth
Fuel Properties	300 - 4000 kPa, 700°C to 1700°C	±0.5% resolution, quasistatic
Exhaust gas composition, COx, NOx	20 - 200 kPa, 300°C - 500°C	resolution ±1%, quasistatic

Table 1.1 shows that the future pressure sensors should be able to measure up to *35 kPa*, with a resolution of *±5%* and a bandwidth of up to *1000 Hz* in an environmental temperature of up to *1700°C*. Currently available technologies of materials used in manufacturing pressure sensors are limited to operate in environmental temperatures of up to *750°C* [5].

1.2 Literature review

In this section, several recent pressure and velocity (or flow rate) sensors will be discussed first from the point of view of material, construction, and fluid dynamics. The vortex flow meter will then be discussed since its principle of operation is based on vortex shedding

behind an obstacle, which is the focus of the present work. Finally several papers, having one or two bluff body arrangement, will be discussed. These papers investigate the flow field experimentally and/or numerically using *CFD* tools.

1.2.1 Pressure sensor

In a gas turbine environment, high temperature is usually accompanied with high pressure exposing the pressure sensor to difficult conditions due to:

- Lateral thermal diffusion affecting microelectronics and requiring high insulation to shield the wiring and signal transmission.
- Thermal stresses and overload.
- Shape change due to anisotropic/ thermal expansion coefficients.
- Thermal oxidation.

Multilayered thin film insulator for harsh environments

A typical multilayered thin film is composed of five films shown in Figure 1.1.

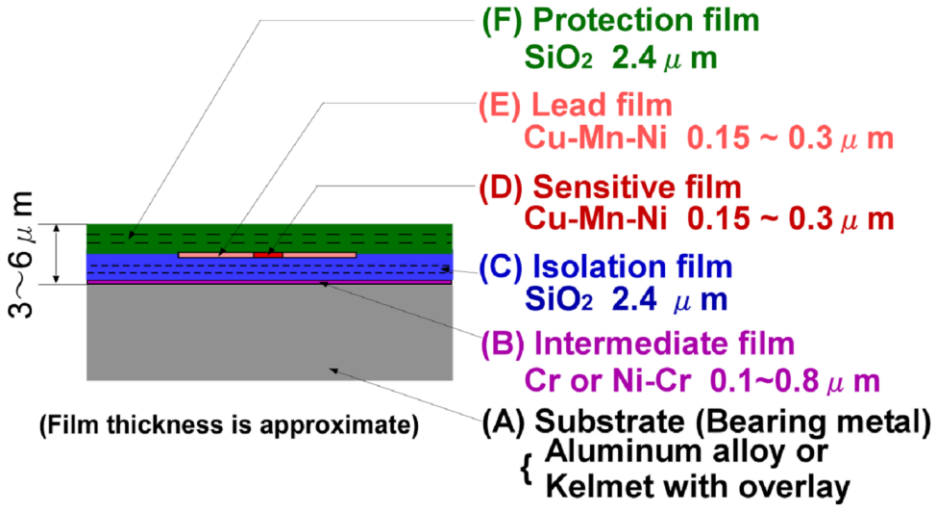

Figure 1.1: Basic structure of multilayer thin film sensor [6].

The use of thin films to electrically insulate thin film sensors on engine components minimizes the sensor intrusiveness and allows for a more accurate measurement. Investigations [7] on using a variety of insulating films to prevent electrical shorting caused by failure of the insulation layer between the sensor and the component have demonstrated that thin film sensors have several advantages over wire or foil sensors. The former do not require special machining of the components on which they are mounted, and their

thickness can be less than $10\ \mu m$ [7]. Being considerably thinner than foils ($525\ \mu m$), thin film sensors are thus much less intrusive. They are also light-weight and consume less power. Several thin film sensors have been tested up to $1100^{\circ}C$ in different engine conditions at *NASA* Glenn Research Center [8]. There are currently investigations on the use of several coating metals of the thin film to prevent the oxidization due to the reaction of the surface of hot metal with the working environment. Some metals like platinum and gold resist oxidation up to a temperature of $900^{\circ}C$. For temperatures over $900^{\circ}C$ two serious challenges arise. Firstly, a developed model of film will be lost due to volatile oxidation. Secondly, over time the evaporation will affect the resistance of the thin films to these temperatures and they will fail to maintain their calibration [9].

Micro pressure sensor for high temperature applications

Leo *et al.* [10] present the development of a micro pressure sensor that would be capable of operating in a high temperature environment using Silicon Carbon-Nitride (*SiCN*). There are three important issues discussed in [10]: material technology, sensor construction and experimental assessment. In terms of material, Silicon Carbon-Nitride (*SiCN*) is a recently developed ceramic whose mechanical properties remain stable up to $1400^{o}C$ even in a corrosive environment [11]. It is also easy to make any shape from *SiCN* because it is molded from liquid phase. However the stress during the joining process and its electric non-conductivity are two disadvantages for *SiCN*. There are attempts to reduce the stress during the joining [12, 13] and make *SiCN* electrically conductive [14]. *SiCN* has many advantages for use in *MEMS* and is very suitable for use in a high temperature environment. From the construction viewpoint, the sensor consists of two main elements: a blocking element (*BE*) and a sensitive element (*SE*) with a small gap in between. Both elements are treated as cantilever beams. The reason why a cantilever beam is used instead of a diaphragm is summarized as follows [10]:

- The manufacturing of a micro cantilever beam is easier than that of a diaphragm.
- A cantilever beam is more sensitive than a diaphragm of the same size because it will exhibit more deflection for the same load.

- The cantilever model dimension is smaller than the diaphragm for the same dynamic and static performance. The length of the cantilever beam is 0.58 times the radius of the diaphragm.
- The sensitivity of a cantilever can be changed without changing its natural frequency by changing its width and its cross section. But in the case of a diaphragm only the radius can be changed.
- Sensitive element overloading will make it stick to the blocking element, preventing the plastic deformation which may occur with the diaphragm.

It is clear that, by using *SiCN*, the pressure sensor can withstand a high temperature up to *1400°C*. Also this paper presented a new structure of pressure sensor but it did not give the characteristics or accuracy of the sensor.

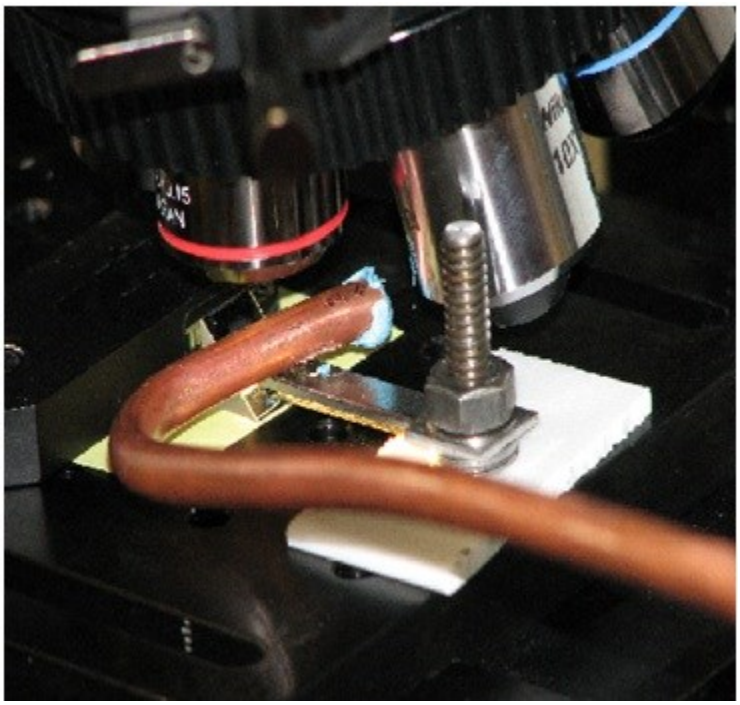

Figure 1.2: Sensitive element under the microscope, [Leo, [10]].

1.2.2 Velocity (flow rate) sensor

The last section summarized the advantages of a cantilever structure when used as a pressure sensor in a high temperature environment in terms of overcoming the effect of

thermal expansion and overload. In this section, the cantilever sensor used to get the flow rate and flow direction will be surveyed in more details.

MEMS-based micro-sensor for flow rate and flow direction

In this section, the use of the micro-sensor to measure pressure, flow rate and flow direction by measuring the cantilever beam deflection is discussed. Recent research has investigated the importance of interface between flow and the elastic element in the micro-sensor in the development of a high accuracy sensor. In Lee *et al.* [15], the flow moves on the top surface of the sensor, shown in Figure 1.3, thus bending the cantilever tip slightly upward or downward. The beam deflection can be transformed into an electrical signal due to the difference between the thermal conductivities of the silicon nitride film (colored green) and the silicon beam (colored pink). Also by arranging eight cantilever beams on an octagonal platform the flow direction can be determined. The authors carried out the numerical modeling of octagonal sensor platform, shown in Figure 1.3, using *ANSYS-FLUENT* where the Reynolds Averaged Navier Stokes *(RANS)* Equations are solved for steady incompressible flow.

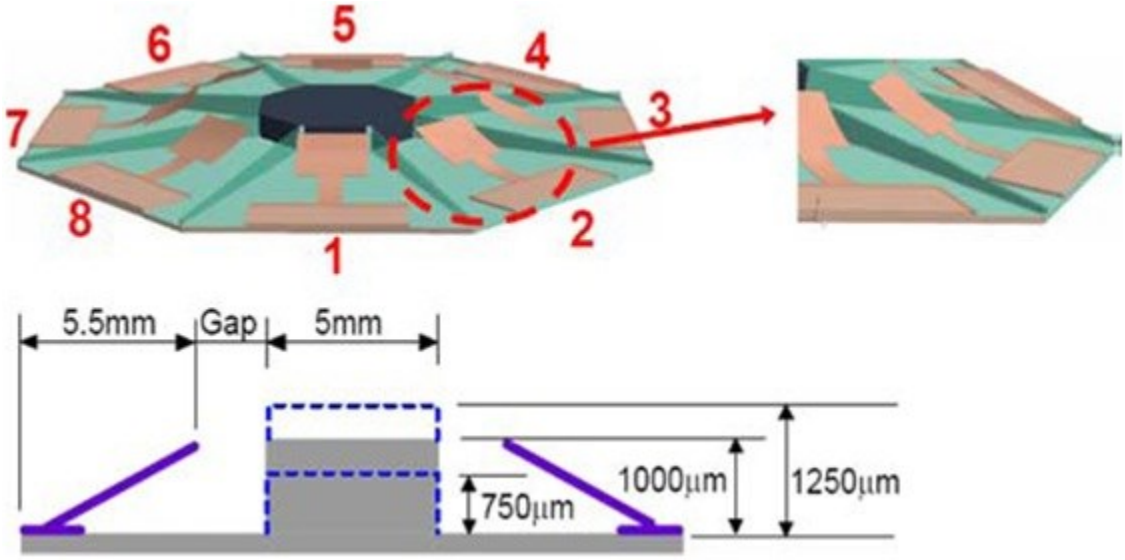

Figure 1.3: Schematic of octagonal micro-sensor, [Fu, [15]].

Lee *et al.* [15] performed their experiment in the wind tunnel but on a single cantilever beam to examine the numerical modeling accuracy. The experimental results show that, at

a resistor length of 4 mm and a temperature of 30^oC, the flow-rate sensor has an average sensitivity of *0.0785 Ω/m/s*, a maximum detection error of *2*% and a measurement range of *0 - 45 m/s*. Given these results, this sensor suffers from two disadvantages:

- If the flow exceeds the *45 m/s* limit under the experimental conditions.
- The experiment temperature of 30^oC is rather low and does not demonstrate the diaphragm's ability to sustain a high temperature environment.

1.2.3 Vortex flow meter

The vortex flow meter will be reviewed in some detail since it shares some flow features with the sensor proposed in this work namely, the flow measurement using the vortex shedding frequency and the drag force behind bluff bodies. This review will focus on two points: the principle of operation and the vortex meter design.

The principle of operation

The vortex meter is based on vortex shedding behind a bluff body placed in the flow. Due to viscosity, a boundary layer develops on the bluff body and separates on both sides of it. Vortices form on both sides of the bluff body and are then shed alternately into the downstream flow at a given frequency. The frequency was found to be directly proportional to the upstream flow velocity [16].

$$U_\infty = \frac{f\ d}{S_t} \qquad 1.1$$

Where U_∞ is the upstream flow velocity, d is the width of the bluff body and S_t is the Strouhal number.

This relation shows that the vortex shedding phenomenon is not sensitive to the physical properties of the fluid like viscosity and density, at least in the context of the work carried out in [16]. The shed vortices appear as a disturbance in the local velocity and pressure fields. The bluff body width is constant and as shown in Fig. 1.5 S_t number downstream of the body was found to be constant (≈ 0.19) in a wide range of Reynolds number ranging from 3×10^2 to 1.5×10^5, see [17]. Hence, for the conditions present in [16], the velocity can be found by measuring the vortex shedding frequency at around 10d in the wake downstream of the bluff body.

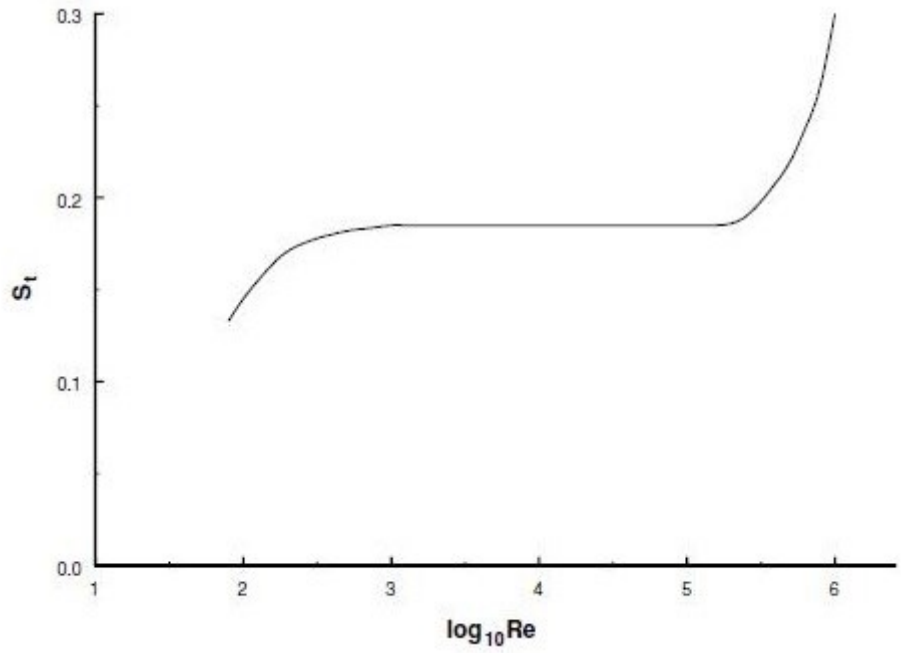

Figure 1.4: Strouhal number versus Reynolds number, [Yamasaki, [17]].

Several other researchers obtained a similar variation of Strouhal number with Reynolds number [16]. However, they differ in the geometry of the bluff body and in the corresponding flow observations related to e.g. the variation of Strouhal number with distance downstream of the body, solution bifurcation downstream of the body.

Kim and Durbin [18] give a physical interpretation of the vortex shedding which goes as follows. For large values of Strouhal number (of order 1) in the near-wake region, viscosity dominates the fluid flow resulting in a collective oscillating movement of the fluid "plug". For small Strouhal numbers e.g. of order 10^{-4}, the high-speed flow dominates the oscillation. At intermediate Strouhal numbers, the oscillation is characterized by vortex buildup and subsequent shedding. For spheres in uniform flow where the Reynolds number range is $800 < Re < 100{,}000$, there co-exist two values of the Strouhal number. The lower frequency is attributed to the large-scale instability in the wake. It is independent of the Reynolds number and measures approximately 0.2. The higher frequency Strouhal number is caused by small-scale instabilities resulting from the separation of the shear layer; these instabilities grow exponentially in the near wake region.

The vortex flow meter that is proposed in this thesis consists of a bluff body, a sensor element and a signal processing system. In what follows, each of these components is discussed.

a) Bluff body

This is the main or primary device. It is responsible for generating strong and regular vortices shedding. So its shape and its geometric dimensions are very important to achieve good quality vortices. The vortex shedding and the signal quality were found to be more regular and stronger for shorter bluff bodies [19] and bodies having end plates [20], respectively. Many researchers have been trying to improve the vortex shedding and the signal quality by changing the bluff body configuration:

- Cousins [20] tested three different shapes of bluff bodies experimentally. He recommended that the optimal ratio of bluff body hydraulic diameter *d* to pipe diameter *D* be between *0.33* and *0.38* for circular cylinders, *0.29* to *0.32* for equilateral triangular cylinders, and *0.24* to *0.28* for rectangular cylinders.
- Bentley *et al.* [21-23] investigated experimentally the dual and triple bluff body arrangements, as shown in Figure 1.5 and Figure 1.6, in two-dimensional flow and they optimized the dimensions of the dual bluff body. These bodies are long rectangular cylinders, placed normal to the flow direction, So that the flow behaviour is close to a two-dimensional flow. They ran their experiments at two levels of turbulence intensity: *5.5* % and *1.5* %. With the dual bluff body arrangement the signal quality is improved and the pressure loss is reduced.

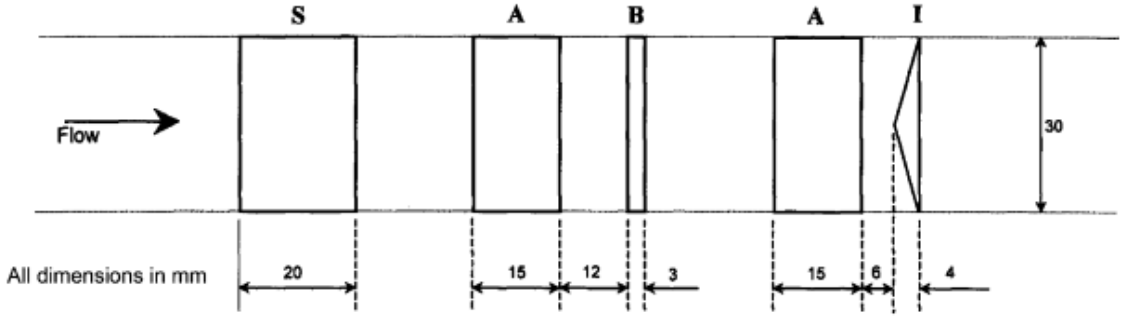

Figure 1.5: The dual bluff bodies' combination tested [23].

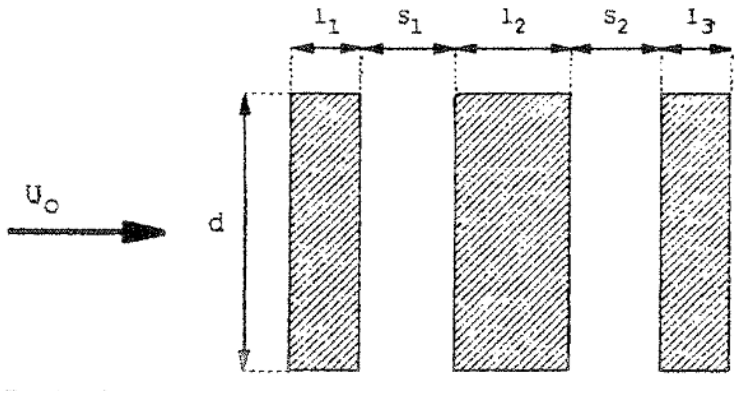

Figure 1.6: The triple bluff body arrangement [21].

b) Sensor element

This is also referred to as a secondary device. It is responsible for transforming the flow disturbances into an electrical signal. Vortex shedding is accompanied by velocity and pressure fluctuations in incompressible flow. Hence if there is change in velocity there is a change in pressure. The sum of pressure and velocity squared is approximately constant (form Bernoulli equation) hence the velocity and pressure fluctuations exhibit a phase shift of around 180^o. Compressible flow involves also a change in density, so when designing a velocity sensor for use in a gas environment, pressure and density can be used to detect vortices. The location of the sensor is very important because the sensor should be located at the point where the vortex shedding is the strongest and the most regular. In practice there are three places: inside the bluff body, in the pipe wall, and outside the bluff body (as a separate part located downstream of the bluff body).

c) Signal processing systems

This component will be developed in the next phase of this work. In general, signal processing systems are responsible for getting the output value of vortex shedding frequency. They depend on the kind of sensor that is used.

1.2.4 Survey of turbulence models

The turbulence model is a key element in *CFD*. There are about six main categories of methods to predict turbulent flows [24]; four of these models will be discussed here.

Reynolds Averaged Navier-Stokes (*RANS*) equations

RANS equations are obtained by ensemble averaging (In experiments, ensemble averaging refers to repeating the experiment several times and averaging the instantaneous values obtained from the different runs of the same experiment.) of the equations governing the fluid motion. Since the momentum and energy equations are nonlinear, six additional terms appear in the momentum equations representing the ensemble average of the product of the fluctuations of every two velocities. These terms are modeled and the approach used in this modeling is referred to as a turbulence model. Four categories of turbulence models as outlined below, have evolved to solve for these additional unknowns:

- Algebraic models, or zero equation models, e.g. mixing length model.
- One equation models.
- Two equation models, e.g. k-epsilon (*k-ε)* model and k-omega (*k-ω)* model [25].
- Second order closure models [26].

  This includes Reynolds stress models e.g. *SSG* Reynolds Stress Model *(SSG)*, *QI* Reynolds Stress Model *(LRR-IQ)* and Reynolds Stress Model *(LRR-IP)*, as well as algebraic stress model e.g. Explicit Algebraic Reynolds Stress Model.

Space filtered equations of motion

These turbulence models depend on the size of computational mesh and consist of:

- Large Eddy Simulations (*LES*)

  Where the large eddies are computed and the smaller eddies are modeled Spalart *et al.* [27] .
- Detached Eddy Simulation (*DES*)

  LES requires an extremely fine mesh size when compared with the RANS mesh size, therefore Spalart *et al.* [27] attempted to improve the predictive capabilities of turbulence models in highly separated regions while reducing the mesh size by using a hybrid approach that would combine features of classical *RANS* formulation with elements of *LES* method. The concept has been termed *DES* is based on the idea of covering the boundary layer by a *RANS* model and switching the model to *LES* mode in detached regions. Ideally, *DES* would predict flow separation from the underlying *RANS* model, and would capture the unsteady dynamics of the

separated shear layer by resolving only those scales that have not been filtered out. Note that *DES*, compared to classical *LES* methods, saves orders of magnitude of computing power for high Reynolds number flows. Also the *RANS* formulation does not provide any information on turbulent flow structures and spectral distribution that might be important to predict flow-induced noise or vibrations.

Space- and time-resolved equations of motion

This approach is referred to as Direct Numerical Simulation (*DNS*) where the momentum, energy and continuity equations are solved to resolve phenomena occurring at all space and time scales. However *DNS* requires an extremely fine space mesh (of the order of $Re^{9/4}$) and time step. *DNS* will be performed in this work so as to capture flow phenomena occurring at all time and space scales. The need to have a better understanding of vortex shedding behind a bluff body is implicitly acknowledged by the amount of experimental work done on this seemingly simple flow configuration. More details will be pointed out in the next chapters.

DNS, LES and *DES* can provide valuable detailed information about the vortex dynamics that exceeds by far those obtained from the *RANS* simulations, however they require relatively large computing resources.

1.2.5 Survey of the wake structure behind a single body

The following survey represents some investigations for flow field around a circular cylinder and around a cube:

- Oertel [28] studied the wake behind bluff bodies from a flow instability point. The region behind the blunt bodies, sphere, is divided into two types of instabilities: absolute and convective. He performed a numerical simulation of wake flows using the impulse response to investigate the existence of an absolutely unstable region in the wake. The absolutely unstable region in a saturated state is defined on the basis of a quasi-steady Navier-Stokes solution. The key to controlling the wake behind bluff bodies is the quantitative determination of the unstable wake region. He also concluded that the development of the von Karman vortex street can be suppressed by using base bleed, suction, splitter plates, and other geometrical manipulations in order to avoid the absolutely unstable wake region.

- Williamson [29] reviewed the *2D* and *3D* wake of steady uniform flow past a circular cylinder. He carried out several measurements for the bluff body wake. He discussed the vortex shedding regimes based on the plots of base suction coefficient over a large range of Reynolds number. He divided these flow regimes into seven regimes based on the Reynolds number. In *3D* flow, he reviewed analytical approaches to vortex shedding involving stability theory. He reported that many other researchers were interested in relating vortex shedding with the stability theory. He found that the vortex might be shed in oblique and parallel modes. In the oblique mode the vortex shedding makes an angle with the cylinder axis typically 15^o to 20^o. Moreover, for Reynolds number values ranging from 49 to 194, vortex shedding was found to be discontinuous. He discussed also many phenomena that happened in *3D* vortex dynamics such as cellular shedding, vortex dislocations, oblique shedding, phase shocks and expansions, and vortex loop. Finally, he raised many questions about the *3D* vortex dynamics need to be answer.
- Roshko [30] investigated experimentally the flow past a large circular cylinder at high Reynolds number (from 10^6 to 10^7) in a pressurized wind tunnel. Two pressure values of *1 atm* and *2 atm* were used. The flow was limited to a Mach number of *0.25* to avoid compressibility effects. The values of velocity, drag coefficient, pressure coefficient and Strouhal number were corrected for wind tunnel interference. He noticed that vortex shedding began at values equal to or higher than $Re = 3.5\times10^6$. When he added a splitter plate behind the cylinder, the vortex shedding disappeared and the drag coefficient decreased. The pressure distribution on the cylinder however was the same.
- Achenbach [31] investigated experimentally the flow past spheres for a Reynolds number range $5\times10^4 \leq Re \leq 6\times10^6$. He measured the total drag, the local static pressure and the local skin friction distributions. All cases were done at a constant turbulence intensity level of about *0.45%*. A string with small diameter was used to support the test sphere from the downstream flow side so as to produce the least effect on the flow. All spheres have smooth surfaces to avoid the effect of surface roughness. He noticed that, an increase in Reynolds number resulted in four regimes of drag coefficient: subcritical, critical, super-critical and trans-critical. He

also measured the separation angle and found that the boundary layer is function of Reynolds number.

- Breuer [32] used the turbulent Von Karman vortex street past a circular cylinder as an experimental test case to evaluate *LES* results. This case was done at a Reynolds number of *Re=140,000* while the flow is still considered subcritical. He used two different curvilinear meshes: one coarse and one fine. Both the Smagorinsky and the dynamic sub-mesh scale model were used in establishing these meshes. He compared the numerical computation results with the experimental data. The *LES* gave a good agreement with the experimental data especially in the near wake behind the circular cylinder. He observed that for a coarse mesh, LES has large deviations in the far wake. He also found that the sub-mesh scale modeling is important for high *Re* flow compared with low *Re* flow.
- Murakami *et al.* [33] investigated numerically the unsteady *2D* and *3D* flow past a fixed square cylinder at $Re=10^5$ using *LES*. The computational results of *2D* and *3D* flow simulations were compared with published experimental data that had been done by other researchers for the same case. The results for 4 different parameters are compared, namely the mean surface pressure coefficients, the *RMS* values of the fluctuating pressure, the power spectrum of the fluctuating lift and drag forces and the flow patterns near the side face. The *3D LES* computations give a good agreement with the published experimental data from all points of view while the *2D* computation compared poorly with the published experimental data. The power spectrum of the *2D* computation near the side face has a sharp peak while the power spectrum of the *3D* computation has a wide band. So the energy transfer mechanism throughout a wide spectrum range cannot be reproduced by the *2D* computations. The vortex stretching, which can only occur in *3D* flow, plays an important role in the energy cascading effect near the side face. He assessed the results obtained from different turbulent models with those obtained from *LES* for vortex shedding at $Re=2.2\times10^4$. The standard k-ε model did not succeed in reproducing the vortex shedding at all. However, the modified k-ε model succeeded in reproducing it well, with an accurate prediction of some parameters. The Reynolds stress model reproduced the vortex shedding rather well, but the results show many

discrepancies with the experimental results, such as the overestimation of periodic fluctuation. As expected, *LES* shows the best agreement with the experimental results.

- Sohankar *et al.* [34] investigated *DNS* of *2D* and *3D* unsteady flow past a fixed square cylinder at *Re=150–500*. The implicit fractional step finite-volume method was used with second-order accuracy in space and time. All numerical simulations were done with a blockage ratio of *5.6%*. For all cases, the authors obtained an unsteady periodic flow after at least *50* shedding periods, which took about *320* time steps. For *Re=200* and *250*, two typical values of the span length *10 and 6 times* the cylinder diameter were investigated and the effects on the results were found to be negligible. The *2D* flow simulations gave laminar shedding flow at *Re=150* while, for the *3D* flow simulations, the shedding started at *Re=200*. Results of the *3D* flow simulations gave a good agreement with the existing experimental data for Strouhal number and drag coefficient; the agreement was less good for those obtained from the *2D* flow simulations.
- Yen *et al.* [35] investigated experimentally the drag coefficient and vortex-shedding characteristics behind a single square cylinder and two side-by-side square cylinders. They used an open loop wind tunnel. *Re* varied between *2,262* and *28,000*, and the ratio of the cylinder spacing to the diameter, the ratio gap, varied in range *0–12*. The experiments were done at free stream velocity ranging from *1.8 m/s* to *9.8 m/s*. The smoke wire scheme was used to visualize the flow pattern using a high-speed camera. They found that the flow behind the two side-by-side square cylinders can be classified into three modes: single mode, gap-flow mode and couple vortex-shedding. A pressure transducer and a hot wire anemometer were used in measuring the surface pressure and vortex shedding frequency. The anti-phase vortex shedding appeared in the gap flow mode while the in-phase vortex shedding appeared in the couple vortex shedding mode. It was found that the drag coefficient and St in the gap-flow mode are less than those occurring in the couple vortex shedding mode and the maximum value occurred in the single mode, while St was found to be the smallest in the gap flow mode.

- Yamagishi *et al.* [36] investigated the flow around a square cylinder, with side *d*, numerical and experimental results were obtained for several values of the chamfer dimension, *C*, and the angle of attack. They investigated also the effect of changing the chamfer dimensions and angle of attack on the drag coefficient and the Strouhal number. They applied the *RNG k-ε* turbulence model. The oil film and mist flow method were used to visualize the surface flow pattern. Both numerical and experimental results were presented in the range of $Re=10^3–6\times10^4$. Four types of cylinders were used with several cutoff length to cylinder side ratios (*C/d*) *0*, *0.033*, *0.1* and *0.167*. They found that the drag coefficient decreased suddenly at an angle of attack of approximately 0^o to 10^o in the case of *C/d=0.1* and *0.167*. For angle of attack 0^o, the drag coefficient was found to be constant at *2* in the range *C/d=0* to *0.033*, it then decreased to a minimum value of 1.2 for *C/d=0.1*.The authors noticed that, for *C/d=0.167*, the tangential velocity was larger than that for *C/d=0.*1 and enlarged the separation area of square cylinder side face.

1.2.6 Two bluff bodies in tandem arrangement

The following survey represents some investigations for the flow field around bluff body arranged in tandem, which is a configuration that resembles the micro-sensor that is proposed in this work.

- Martinuzzi *et al.* [37-39], reported on experimental studies of the periodic vortex shedding behind two square cylinders (*2D*) and two surface-mounted cubes (*3D*) in tandem. The cubes are of dimension *H=0.04 m*, and are mounted on a thin flat plate (3mm thick) at a distance of *2H* from the leading edge, see Figure 1.7. These two cubes were tested in a suction-type wind tunnel with separation space (*S*) varying from *1.5H* to *2.5H*; the air velocity (*U*) equals *8.8 m/s* and the Reynolds number based on cube height (*H*) and free stream velocity (*U*) is *22,000*. They investigated experimentally the effect of the separation distance on the vortex shedding and Strouhal number at this Reynolds number and found that:
    - The intermittent regime, *S <1.5H*, where vortex shedding is interrupted by periods of random fluctuations.

- The cavity-locked regime, $1.5 < S < 2.5$, where vortex shedding is continuous and the frequency scales inversely with S.
- The vortex-locked regime, $4 < S < 6$, where shedding from the downstream cube locks with onto those vortices shed from the upstream cube, producing a strong harmonic signal.
- For $S > 6$ the cubes shed independently and the frequency approaches that of a single obstacle

So they concluded that the vortex shedding is very sensitive to the distance separating the two cubes.

- Havel *et al.* [37] studied experimentally two square cylinders in tandem (*2D* flow) and 2 cubes (*3D* flow) in a thin boundary layer and they identified three regimes: alternate reattachment, lock-in (*3D* only) and quasi-isolated. For the lock-in regime, the shear layer motion over the top of the cubes is strongly coupled to the lateral shear layer motion.
- Sakamoto and Haniu [40] investigated experimentally the aerodynamic forces acting on two surface-mounted square cylinders, their height being *3 times* their side. The Reynolds number is *150,000* and the boundary layer is turbulent and its thickness is *0.8* the cylinder height. Based on drag coefficient, lift coefficient and vortex shedding behaviour at *Re=150,000*, they identified several regimes as a function of the inter-cylinder spacing (*S/h*):
  - Regime 1 for $S/h < 1$, stable reattachment, the separated shear layers are extended along the two sides of the prism as a one obstacle. So no vortex shedding is detected.
  - Regime 2 for $S/h > 1$, unstable reattachment when the flow reattaches on the second obstacle, vortices are shed from its wake. Otherwise, vortices are shed from the first obstacle (i.e. a part of the separated shear layers are rolling up between the two prisms).
  - Regime 3 for $S/h > 2.5$, stable synchronized shedding (where separated shear layers periodically roll up in the inter-cylinder cavity), it is described by synchronized vortex shedding triggered by the first prism

- Regime 4 for unstable synchronized shedding where an additional Strouhal frequency appears on the downstream prism, suggesting binary vortex shedding. There is some indication, however, that Regime 4 and the quasi-isolated regime of Martinuzzi *et al.* [37-39] are very similar.

Although not explicitly stated in the paper, the fact that the boundary layer covers *80%* of the height (which is *3 times* the cube side) the flow behavior is more typical of a three-dimensional flow.

- Farhadi *et al.* [41] used the *LES* to investigate the flow around two cubic bluff bodies in tandem arrangement. Two values of the separation distance between the two cubes: *H* and *2H* are used at a fixed Reynolds number (*Re=22,000*). In both cases the authors emphasized the effect of the separation distance (*S*) on horse shoe vortices and vortex regions around the cubes. They found that when the separation increased between two cubes, the upstream and the stream above the first cube were not affected. But the downstream and the stream above the second cube were affected. They also observed no significant difference in Reynolds stress contours as separation increases.

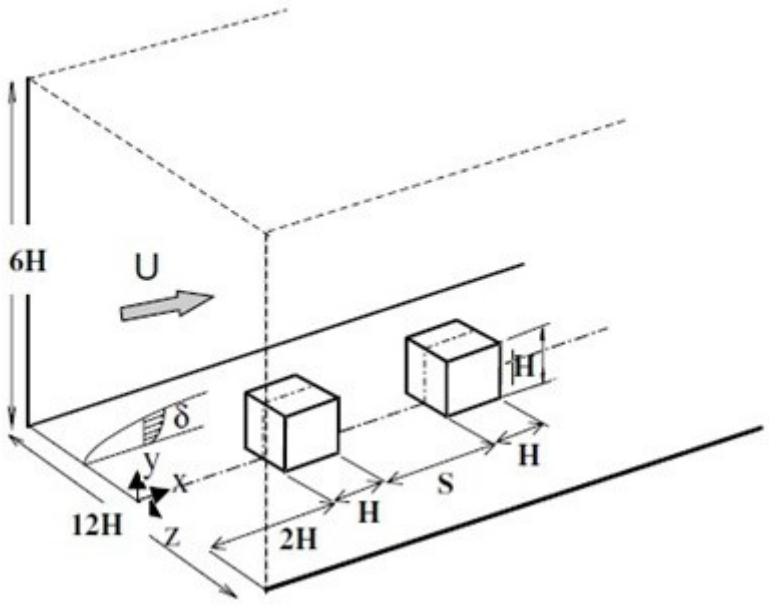

Figure 1.7: Schematic representation of the set up and nomenclature [39].

- Paik *et al.* [42] made a good comparison of applying the unsteady Reynolds-average Navier-Stokes (*URANS*) and several versions of Detached Eddy Simulation (*DES*) as turbulence models around two cubes in tandem. They focused on two values of the separation distance (*S*) between the two cubes: *2H* and *4H* for a fixed Reynolds number (*Re = 22,000*), where H is the cube side. They concluded that *DES* gave results that are more accurate than *URANS* results.

Both Paik *et al.* (2009) and Farhadi *et al.* (2008) used the experimental work of Martinuzzi *et al.* (from 2000 to 2004). Hence all of them worked with the fixed Reynolds number, low velocity range and ambient pressure and temperature conditions. So it is clear that there is a gap of knowledge regarding the flow around two cubes in tandem arrangement at moderate Reynolds number. This Reynolds number is based on micro length scale and high velocity range. In the previous discussions Reynolds number was based on the macro length scale and low velocity range. Also there is a lack of investigation on the effect of Mach number on the Strouhal number.

1.3 Motivation

From the previous discussion it is clear that, in a high temperature environment, pressure sensors made from *SiCN* can withstand temperatures up to $1400^{o}C$ and the cantilever structure is better than any other structure [10]. There have been two attempts to investigate the cantilever pressure sensor but they used low velocity and temperature values. The flow around bluff bodies has been studied due to its practical significance in many engineering applications where most of these studies are mainly in heat transfer and in building engineering. *DES* and *LES* were used to model the turbulent flow around two cubes in tandem arrangement. However no attempt was made at using *DNS* of the flow for that arrangement. *DNS* was done only on flow around one cubic body [43].

Hence there are gaps in knowledge

- The available sensors do not achieve the sensor requirements given in **Error! Reference source not found.**.
- No research investigates the flow around two micro scale bluff bodies in a tandem arrangement at high velocity and temperature.

- No research investigates the fluid dynamics of compressible, turbulent flow field around *MEMS*-based sensors.
- No research investigates the two bluff bodies in tandem using *DNS*.

1.3.1 Proposed new sensor

The experimental work of Leo *et al.* [10] suggested that it may be possible to use two cantilevers in tandem to measure the upstream flow velocity, their thesis being that as the upstream flow velocity increased, the sensitive element (*SE*) placed behind a blocking element (*BE*) would deflect towards the *BE*. They supported their thesis with experimental measurements but because the focus was on the structural side of the proposed sensor, no aerodynamic data was collected.

This experiment intrigued the writer and led to a computational effort to simulate the flow that would prevail in this experiment. A computational domain was set up and the flow was simulated using *ANSYS-CFX*. The *URANS* equations were used to model this flow and several turbulence models of the *DES* type were used. Two interesting results came out of this exercise:

- The sensitive element did deflect forward (towards the blocking element) in a way similar to the experimental observations.
- It was possible to observe vortex shedding from the cantilevers; this shedding was manifested in the experiment as buffeting of the sensitive element. A detailed account of this work can be found in Appendix A.

In this work a micro-scale sensor is proposed to achieve most of the sensor requirements that were listed earlier. As indicated in Figure 1.7, this sensor consists of two micro-scale bluff bodies in tandem both made of Silicon Carbon-Nitride (*SiCN*) to withstand temperatures up to *1400°C*. The bodies are bot cantilevers and are: a blocking element (*BE*) followed by a sensitive element (*SE*). The blocking element faces the flow and induces a wake behind it. The sensitive element deflects due to the difference in pressure across its faces; this deflection can be used as a measure of the pressure difference across the element. The fluid temperature can be measured by detecting the thermal expansion using a strain gauge covered with a multilayer thermal insulation. Finally the flow direction can be measured by using a rudder behind the sensitive element that would orient the sensor along

the flow direction. It can be installed in many environments but the main purpose in this research is to install it in the hot end of gas turbine engines, typically upstream of the 1st turbine vane so as to measure the highest temperature in the turbine. It would generally be fixed to the casing where there may be a need for monitoring or actively controlling the engine. It may also be used in other components such as an intake, a compressor, a cooling-air path in a turbofan engine, a combustion chamber, a turbine or a nozzle for active control purposes.

A full study of all the functionality intended for this sensor is clearly beyond the scope of this work. As a first step, the focus is set on the feasibility of inferring the flow pressure and velocity from the measured deflection and buffeting of the sensitive element due to vortex shedding.

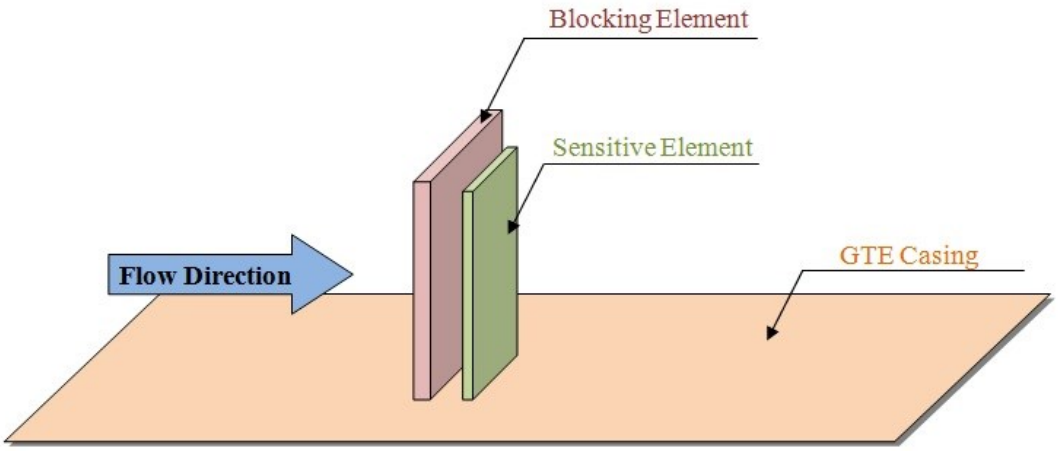

Figure 1.8: Sketch of proposed sensor.

The performance of a cantilever-based sensor depends on:

- The geometry and size of the blocking and the sensitive elements, namely their length, width, and thickness
- The gap distance between the blocking and the sensitive elements

The effect of these 7 parameters on the sensor performance will guide in customizing the sensor for a given application. This study will be carried out numerically by simulating the flow field around the sensor using *CFD*. For the purpose of this work, the geometric parameters are reduced to two by using two similar cubes placed in tandem. In the

parametric study carried out in Chapter 3, the number of parameters is relaxed to 4 parameters.

In the numerical flow simulation, the sensor size is set to be in the micro-scale level so as to reduce the number of computational mesh nodes since the *DNS* needs a very fine mesh, which can be a prohibiting factor for the simulations. For several size sensors, the π-theorem can be used to scale the numerical results up or down.

1.4 Research objectives

This work aims at studying the fluid dynamics aspects of the flow around two blunt bodies set in tandem with the goal of using this configuration in designing a micro-sensor suitable for use in the gas turbine environment. The flow in this configuration is three-dimensional and unsteady, involving flow separation, horseshoe vortex formation, quasi-periodic vortex shedding in the shear layer and wake, and multiple recirculation zones. In fact, the *CFD* Society of Canada had set this problem as the Challenge Problem for the 2012 conference [44]. It is a complex flow with flow structures occurring at several length scales, which calls for the use of *DNS* to resolve all these scales. The resulting flow simulations, after verification against flow physics and available experimental data, will provide a tool for computing the vortex shedding frequency and the drag force on the obstacles. This work is a first step towards the development of a micro-sensor that can be used in measuring the pressure and velocity starting from the measured deflection and buffeting of the sensitive element together with the computed vortex shedding frequency and the drag force on the sensitive element.

1.5 Concluding remarks

From the previous discussion, there is a need to develop a micro-sensor for mini- and micro-systems that should be able to measure V, p, T and flow direction. It is suggested that this micro-sensor be composed of two cantilevers in tandem: a blocking element and a sensitive element, involving 7 geometric parameters.

Some of the challenges facing this research are the flow simulation using *DNS*, the inherent *3D* nature of the flow and its impact on vortex shedding, and the effects of compressibility. The aim is to assess the micro-sensor performance in terms of the effect of Reynolds Number and Mach number on Strouhal Number. To this end, the following work is carried out:

- Investigate experimentally the flow around two cubes in tandem using soap film flow visualization (essentially *2D* incompressible flow).
- Simulate the *2D* and *3D* flow around two cubes in tandem using *DNS*.
- Verify the numerical simulations against experimental observations
- Carryout a parametric study on the effect of geometry and flow parameters on the vortex shedding and on the forces acting on the sensitive element (2^{nd} cube)

As a first step reduce the number of geometry parameters from seven to two by using two similar cubes in tandem.

1.6 Research plan

The research objectives can be implemented through the following steps:

- Flow visualization around two cubes in tandem arrangement by using vertical falling soap film.
- Investigation of the two-dimensional incompressible (water) flow field around two cubes in a tandem arrangement using *DNS*.
- Assessment of the *DNS* results in *2D* incompressible flow of water against soap film flow results and against other available experimental results
- Investigation of the inter-cube spacing on Strouhal number in *2D* incompressible flow.
- Investigation of the two-dimensional compressible flow field around two cubes set in tandem using *DNS* at several Mach and Reynolds numbers.
- Carryout a parametric study on the effect of inter-cube spacing, Reynolds number and Mach number in two-dimensional flow
- Investigation of three-dimensional compressible flow field around two cubes in tandem arrangement using *DNS*.

- Investigate the effect of Reynolds number and Mach number on Strouhal number for *3D* and *2D* flow fields.
- Compare with previous work whenever available

1.7 Thesis outline

This thesis consists of five chapters; Chapter 1 gives the introduction and literature survey of various pressure sensors and techniques for controlling and solving the flow field around bluff bodies. The use of *MEMS*-based sensor to possibly measure flow rate, pressure, temperature and flow direction is also introduced, and the main objective of the present work is presented. In Chapter 2, the test rig used to carry out the experimental work is described, and the experimental results are introduced and compared with other experimental works. Chapter 3 is devoted to the study of two-dimensional simulations of incompressible water flow around two bluff bodies set in tandem. It includes a theoretical investigation and verification of all parameters used in the *DNS* and a comparison between the numerical and experimental results. A parametric study is also carried out to study the effect of geometry and Reynolds number on Strouhal number and drag coefficient. Chapter 4 presents a study of the compressible *2D* and *3D* flow of air around two bluff bodies in tandem. Interesting *2D* and *3D* phenomena are identified and interpreted from the numerical results. In Chapter 5, concluding remarks, recommendations, important contributions and suggestions for future work are presented.

Chapter 2

EXPERIMENTAL WORK

2.1 Introduction

The study of engineering problems is currently carried out analytically or numerically then usually complemented with experimental work for verification and assessment of the analytical or numerical results. In the present research, the experimental work is based on flow visualization, which is recorded using a high-speed camera. A vertically falling soap film is used to visualize the fluid flow around two cubes in a tandem arrangement. The soap film is considered to be the nearest physical approximation of two-dimensional flow due to its rather small thickness (of the order of a few microns). The nature of soap film is well described by Rutgers *et al.* [45]. The experimental investigation in the present study was carried out in the Fluid Dynamics Research Laboratory in the Mechanical and Industrial Engineering Department at Concordia University.

2.2 The test rig

Figure 2.1 is a pictographic representation of the experimental test rig. This rig was recently developed by Dr. Ng, of the MIE Department. Dr. Fayed, also of the MIE Department, assisted the author in running the experiment and collecting the data.

Figure 2.1: The test rig.

A schematic diagram indicating the major components of this rig is shown in Figure 2.2.

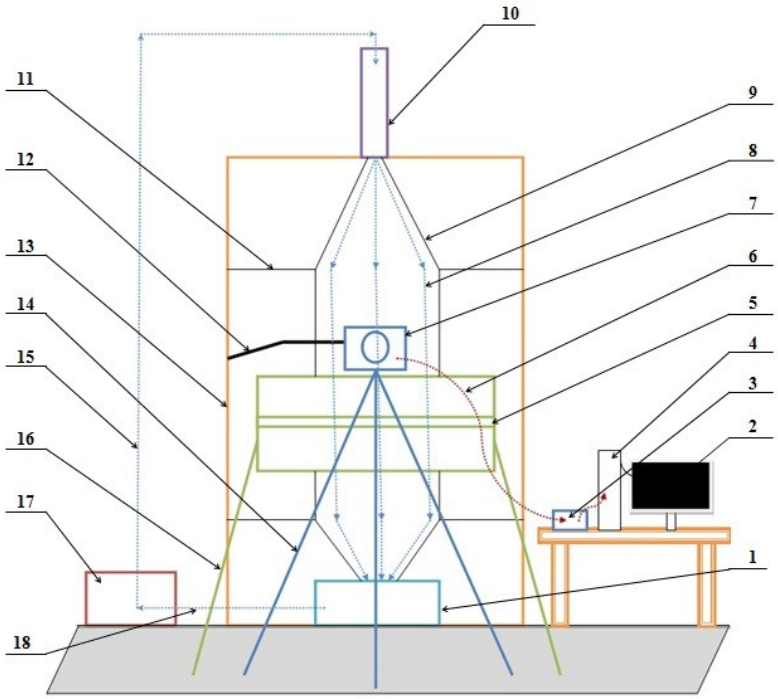

Figure 2.2: Test rig schematic diagram.

Where:

1. Sump tank.
2. Computer monitor to observe the flow through the digital camera.
3. Power supply for the high speed camera.
4. CPU of the computer to storage the data.
5. Low pressure sodium lamp (Philips 50X135W).
6. Data cable from high speed camera to PC.
7. Digital high speed *10bit CMOS* camera system (the type is pco.*1200hs*) is characterized by:
    - Capture speed of *636* frames per second (*fps*) at high resolution and *1357 fps* at VGA resolution.
    - High resolution is *1280×1024 Pixel*.
    - Exposure time range 50 ± 5 *s*.
    - Image memory in camera is camRAM up to *4 GB*.
8. Soap film flow.

9. Thin wire *0.5 mm* providing the boundary of the soap film.
10. Scaled tube.
11. Thin wire to adjust the width/speed of the soap film.
12. Carrier to fix and adjust the two cubes (*BE* and *SE*) inside the soap film flow.
13. Wood frame to assemble the experimental parts.
14. Tripod of the high-speed camera.
15. Hose from the pump to the scale tube.
16. Stand for the low-pressure sodium lamp.
17. Peristaltic pump with controller (Millipore Peristaltic Masterflex Pump, model No. *7017*).
18. Hose from sump tank to the pump.

2.3 Preparing the test rig

Setting up the test rig to obtain good visualization involves the following steps:

1. Preparation of a soap film consisting of *98.5 %* water and *1.5 %* concentrated dish-washing liquid. This fluid is prepared separately in a scaled vessel. It is then mixed out slowly to reduce soap bubbles and put in the sump tank.
2. Low pressure sodium lamp, shown in Figure 2.3, is turned on *10* to *15 minutes* before the visualization starts in order to warm up. It emits a bright yellow light as the sodium metal is vaporized, (Figure 2.1.). The monochromaticism of this light, is a very important property for fluid visualization, and is distributed using tracing paper.

Figure 2.3: Low pressure sodium lamp before warming.

3. Fixing the high speed camera on a tripod and adjusting its zoom to get accurate visualization of the flow phenomena.
4. Turning on the Peristaltic pump, shown in Figure 2.4, which works by compressing and relaxing a hose that is positioned between a rotating device and circular pump housing.

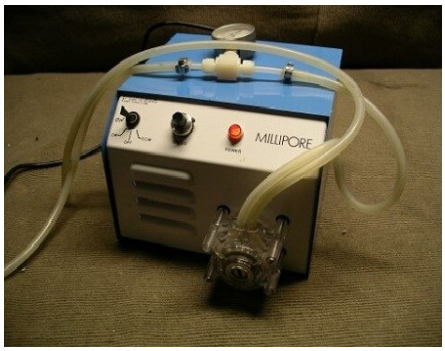

Figure 2.4: Peristaltic pump with controller.

5. Fixing and adjusting of the blocking and sensitive elements on a carrier to keep them in tandem, parallel to one another and orthogonal to the upstream flow direction.

At this point, the test rig is ready for visualization.

2.4 Visualization procedures

By turning on the pump the flow is pumped into the scaled vessel. The fluid then falls down between the two boundary thin wires and across the two cubes. The high speed camera simultaneously records the flow pattern and transfers the data to the computer. The flow pattern can be observed on the computer monitor and saved on hard disk.

2.5 Discussion of the results

In the present experimental work, two cubes, representing the blocking element (*BE*) followed by the sensitive element (*SE*), are tested at several flow speeds. The visualization is done for two sets of steel cubes of several dimensions namely *1/8"* (*3.17 mm*) and *3/16"* (*4.76 mm*). The spacing between them is set equal to the element side. A large number of flow images showing the flow around and downstream of the cubes, is recorded. A sample

of these images is shown in Section 2.5.1. These images allow for the computation of the flow velocity and the vortex shedding frequency, as discussed in Sections 2.5.2 and 2.5.3.

2.5.1 Experimental flow field images

The high-speed camera captured about *18,000* to *20,000* images that are *1ms* apart in about *18* to *20* seconds. Figure 2.5 and Figure 2.6 show the flow pattern around the *1/8″* and the *3/16″* cubes at several Reynolds numbers. A lot of information can be extracted from these two figures, some of which is discussed here, and some later when this flow is simulated numerically. The flow, vortex shedding and flow instability depend strongly on Reynolds number. This dependence can be categorized as three regions:

- For low *Re*, as shown in Figure 2.5a and Figure 2.6a, the flow is rather steady and is characterized by a limited recirculation zone downstream of the blocks. Note that the shear layer that is shed from the right side of the 1st cube reattaches on the 2nd cube and a low speed recirculating flow can be clearly seen on the left side of the cavity. Hence the inter-block cavity is isolated from the rest of the flow.
- As *Re* increases, as shown in Figure 2.5(b, c) and Figure 2.6(b,c), there is a strong periodic vortex shedding pattern in the far-wake region. It develops and convects downstream. The convection speed and the interaction between the vortex shedding from the *BE* and the *SE* is Re dependent. Note the vortex formation and shedding behind each of the cubes, as indicated. in the gap between the cubes as well as downstream of the 2nd cube.
- Finally, at high *Re*, as shown in Figure 2.5d and Figure 2.6d, the boundary layers and the wakes are clearly turbulent and the vortex shedding starts to become a destabilizing factor for the film.

Note that, as Reynolds number increases, the vortex shedding becomes a destabilizing factor for the fluid film. For this reason it was decided to present the *2D* experimental results at *3* values of Reynolds number: *7301*, *10,000* and *14,660*. This fact limits in part our ability to compare the present experimental results with most of the previous work as it falls at higher values of Reynolds number.

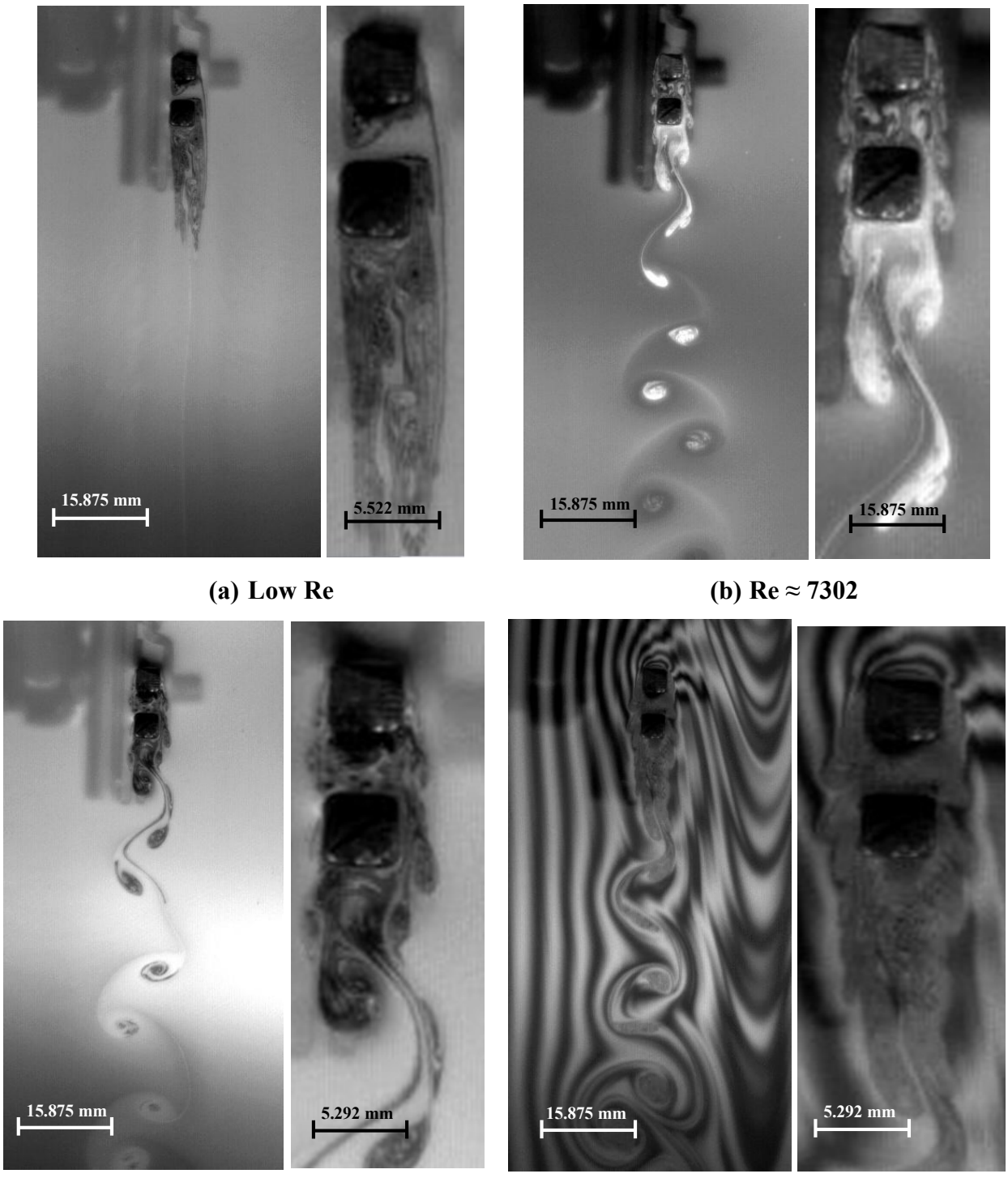

(a) Low Re **(b) Re ≈ 7302**

(c) Re ≈ 8255 **(d) Re ≈ 14605**

Figure 2.5: Flow field around BE and SE with h=1/8'' at several Re, in the far wake (left) and near wake (right).

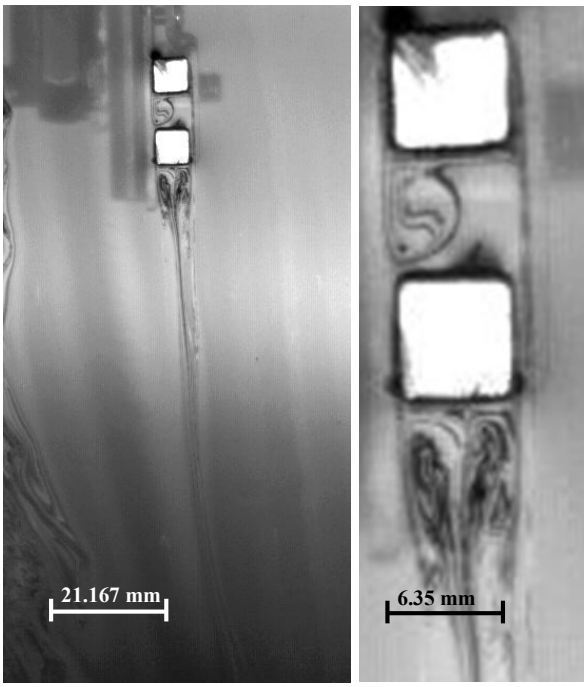

(a) Low *Re*

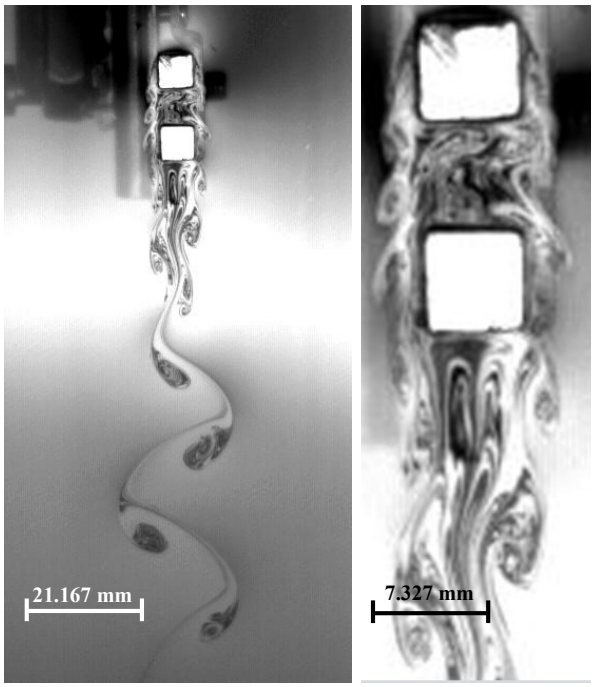

(b) Re≈16668

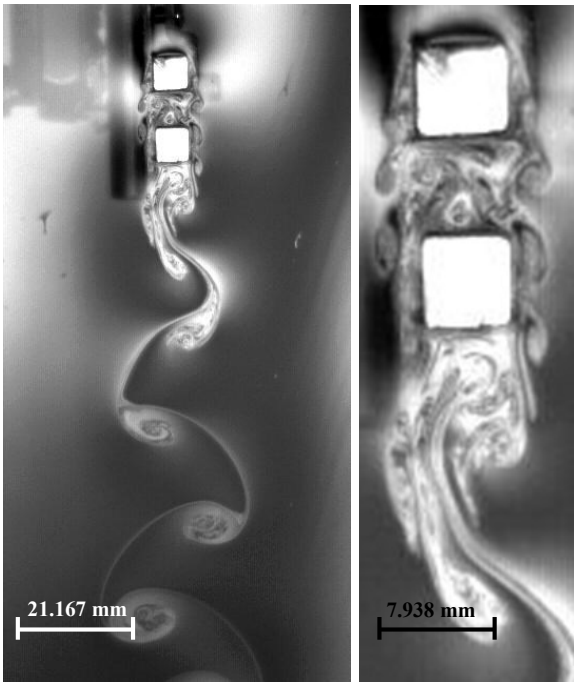

(c) Re≈17621

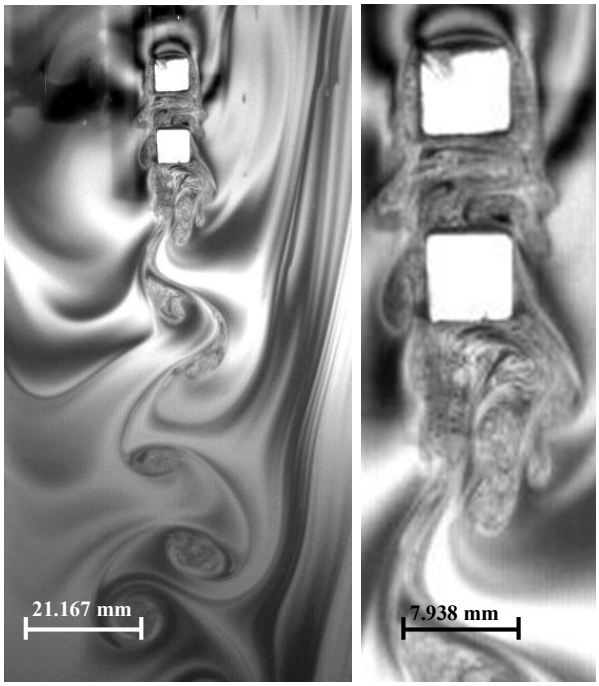

(d) Re≈18574

Figure 2.6: Flow field around *BE* and *SE* with *h=3/16"* at several *Re*, in the far wake (left) and near wake (right).

2.5.2 Calculation of the soap film velocity

Given that the vortex lines are material lines, the flow velocity can be estimated reasonably well from the advance velocity of the vortices. By importing the sequential images from the high-speed camera into the *AutoCAD®* program, each vortex core is traced and the distance between its old and new positions is measured. The velocity of each vortex core is then calculated by dividing the distance between the two positions by the elapsed time, namely *1ms*. This process is repeated for 7 to 10 times and the resulting velocities are averaged out to eliminate possible errors.

2.5.3 Calculation of vortex shedding frequency

The vortex shedding frequency is calculated by importing one thousand images shot by the high-speed camera into the 'Picture Viewer' software and marking the space location of a vortex core in the first image. The core of any vortex can be observed as a brightness or darkness spot. This mark is considered as a fixed point in space. The rest of the thousand images are moving, ascending with time (i.e. in a given order), relative to the fixed point thus allowing the number of vortices that pass through this fixed point to be counted. Since the elapsed time for one thousand images to pass by is one second, the number of vortices that pass through the fixed point is equal to the vortex shedding frequency.

2.5.4 A sample experimental case

In the present experimental work, 30 to 40 sets of images are taken at each soap film velocity. By applying calculations in sections 2.5.2 and 2.5.3 on one set of images where $h=1/8''$, the film velocity (U_{exp}) was found to be *2.24 m/s* and the vortex shedding frequency (f_{exp}) equal to *146.5 Hz*. Since the kinematic viscosity of soap film ν_{sf} can be taken as that of water $\nu_w=10^{-6}\ m^2/s$, then:

- Experimental Reynolds number (Re_{exp}):

$$Re_{exp} = \frac{U_{exp}\, h_{exp}}{\nu_{sf}} = 7103 \qquad 2.1$$

- Experimental Strouhal number (St_{exp}):

$$St_{exp} = \frac{f_{exp}\, h_{exp}}{U_{exp}} \qquad 2.2$$

2.5.5 Experimental uncertainty

Given the importance of the soap film velocity and the vortex shedding frequency in determining the Reynolds and Strouhal numbers, this section will discuss the measurement error and/or the uncertainty of these two quantities.

Vortex shedding frequency uncertainty

From section 2.5.3, the vortex shedding frequency depends mainly on the vortex count in a one-second interval where *1000* pictures are taken. Since the vortex shedding in the experimental work is clearly observable, there is no error or the uncertainty in counting the vortices, and hence no vortex shedding frequency uncertainty.

Soap film velocity uncertainty

The soap film velocity uncertainty depends mainly on how the velocity is measured which in turn can be affected by the thickness variation in the film.

The soap film velocity can be measured by two major methods. The first is by using an instrument such as a Laser Doppler velocimetry, hot wire anemometry, Fiber velocimetry, Homodyne correlation spectroscopy and particle imaging velocimetry. The second, which is in fact the one being used in this work, is image processing. Image processing however depends on the flow visualization and is therefore subject to optical interference in thin films that occurs between the front and back surfaces. A quarter wavelength changes in film thickness will change the interference condition from constructive to destructive. Thickness variations in the film are therefore visible as dark and bright fringes, especially when viewed under monochromatic light. Researchers such as Rutgers *et al* [44] have estimated the change in the thickness to be about *5%* to *10%*. This change affects the dark and bright parts of the film thus leading to an uncertainty in the flow velocity by a corresponding amount.

As explained in Appendix C, the velocity of each vortex core is calculated by tracing each vortex core in the images and dividing the distance between the two old and new positions by *1ms*. In order to reduce the above mentioned experimental uncertainty in the present work, the process is repeated several times and the resulting velocities are averaged out. First, groups are established from the images taken by the high-speed camera. Each group consists of at least seven images, each two images produce one velocity. Each image in the

group includes at least three clear vortices. Second, the velocity of each vortex is calculated as stated above. So each vortex has six velocities that are calculated in one group. To reduce the error the average vortex velocity is taken. So in each group, three average vortex velocities are calculated. Therefore, three Strouhal numbers are calculated. It is observed that the standard division between them is less than *0.001*. Again the average Strouhal number is calculated from each group. By repeating this for ten groups, ten Strouhal numbers are calculated. Finally, by taking the average of these ten Strouhal numbers the final exponential Strouhal number is calculated. So, using more than 210 vortices, *180* vortex velocities and 180 Strouhal numbers are calculated and averaged culminating in the final exponential Strouhal number which equals *0.21* with standard deviation equal to *0.52%.*

2.6 Concluding remarks

The soap film gives a good visualization of the flow patterns using the high speed camera. The experimental measurement of the vortex shedding falls within *5%* of experimental data available in the literature. The uncertainty in measuring the shedding frequency is around *0.5%.* Therefore it will be used to verify the numerical flow simulations in the *2D* incompressible flow limit.

Chapter 3

TWO DIMENSIONAL INCOMPRESSIBLE FLOW SIMULATION USING DNS

In this chapter, the flow development around two similar cubes in tandem, which was visualized using the soap film technique, is numerically computed using direct numerical simulation of the governing flow equations using *ANSYS-CFX* and assuming two-dimensional flow. The results of the numerical simulations are compared with experimental observations qualitatively and quantitatively in order to assess both. The assessed program is then used to carry out a parametric study of the effects of geometry and compressibility on the flow features of the configuration in question; see Figure 3.1. The effect of compressibility will be discussed in the next chapter. Note that the word 'cube' is loosely used in this chapter instead of 'square cylinder', since the object used in the experiments is literally a cube, while the soap film flow is considered to be a *2D* flow.

3.1 Flow governing equations

The flow governing equations assuming incompressible Newtonian fluid are written as [26]:

Continuity equation

$$\vec{\nabla} . \vec{U} = 0 \qquad 3.1$$

Momentum equations

$$\frac{\partial \vec{U}}{\partial t} + \vec{\nabla} . \left(\vec{U} \otimes \vec{U} \right) = - \vec{\nabla} p + \vec{\nabla} . \bar{\bar{\tau}} \qquad 3.2$$

Where the stress tensor, $\bar{\bar{\tau}}$, is given by:

$$\bar{\bar{\tau}} = \mu \left(\vec{\nabla} \vec{U} + \left(\vec{\nabla} \vec{U} \right)^T \right) \qquad 3.3$$

For incompressible flow, the density is constant hence it is eliminated from the continuity and momentum equations, and the energy equation decouples from continuity and momentum. The equations are solved in the Cartesian coordinate system and the velocity vector is two-dimensional.

3.2 Numerical implementation

The flow governing equations are integrated in space using a second order accurate finite volume approach, in which the control volume is node-centered, and the finite element approach is used to integrate the equations in space. The resulting equations are linearized and are integrated in space using an iterative approach. The problem is considered converged when the normalized *RMS* (root mean square) value of the residuals is less than 10^{-8}. For unsteady flow simulations, the equations are integrated in time using a second order backward Euler scheme (also known as Gear scheme), which is an implicit scheme in time. More details are given in the *CFX-solver* 'Theory Documentation' [26].

3.2.1 Computational domain

A configuration of the computational domain with two cubes in tandem is shown in Figure 3.1 where:

- h is the cube side and the reference length (i.e. characteristic length scale). It is set to $40\ \mu m$ in all cases
- S is the separation distance between the two cubes and is varied between 0 and $3h$.

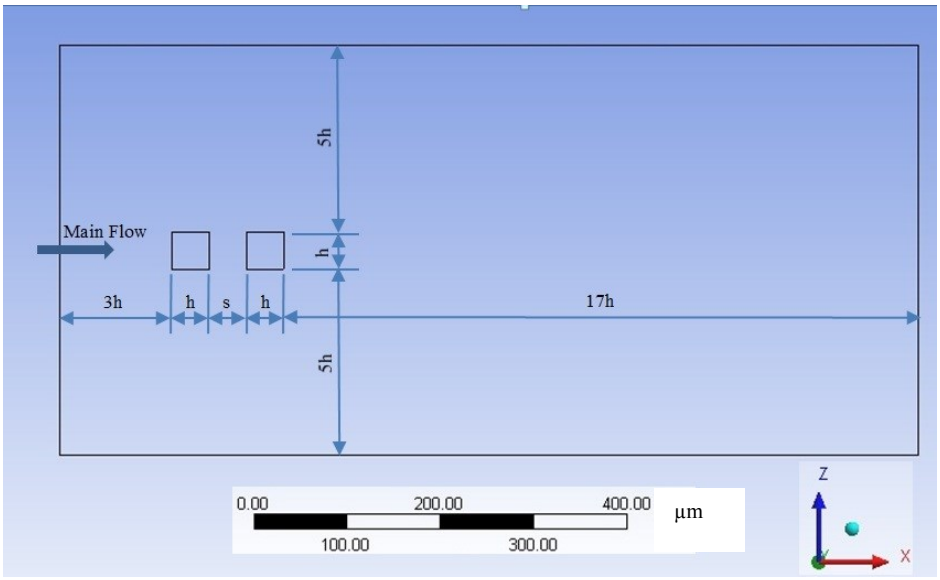

Figure 3.1: Schematic representation of the setup and *2D* nomenclature.

The computational domain extends *23h* in the streamwise direction *x*. In a series of trials, the distance was varied between *5h* and *2h* and its effect on the flow pattern was found to be negligible. The inlet flow boundary therefore is taken at *3h* upstream of the blocking element (i.e. at $x/h=-3$) where, due to the above, the flow is considered to be uniform and parallel to the *x*-axis. In the *y*-direction, the flow domain extends a distance $y=\pm 0.0125h$ from the symmetry plane $z=0$, and the flow is assumed to be symmetric there. The flow is bounded by two walls that are located at a distance $z=\pm 5.5h$ from the symmetry plane $y=0$. This distance ensures that the effect of boundary layer thickness at the two side-walls is negligible. The boundary layer thickness is calculated in Appendix B assuming that it is similar to a flat plate *B.L.*; it is found that the boundary layer is small relative to the domain size in the spanwise direction namely, *11h*. So the effect of the side-walls on the flow is negligible.

Since *CFX* cannot deal explicitly with a *2D* geometry, the computational domain is three-dimensional with 0.025h depth in the y-direction, and both planes at $y=\pm 0.0125h$ are set as symmetry planes. This treatment enforces the *2D* assumption implicitly. The depth of *0.025h* is taken to give good aspect ratio of the mesh elements. The origin of axes is taken at the centre of the leading edge of the blocking element (*BE*) (i.e. first cube). The first cube is located at $0 \leq x \leq h$. The second one is located at $h+S \leq x \leq 2h+S$.

3.2.2 Mesh resolution

Since the flow governing equations are simulated directly, the mesh must be of the order of the Kolmogorov length scale (η) so as to capture all flow features. At the same time the continuum assumption must be respected. Hence the mesh size depends on the Reynolds number (which implicitly implies the Kolmogorov length scale) and the mesh quality such as aspect ratio and skewness. Before prescribing the mesh size, the Kolmogorov length scale should be estimated and the continuum assumption should be verified.

Kolmogorov length scale (η)

The Kolmogorov length scale is calculated as follows [25] (page 314):

$$\eta = \left(\frac{\nu_w^3}{\epsilon}\right)^{1/4} \text{(m)} \qquad 3.4$$

Where ν_w is the kinematic viscosity of water ($10^{-6}\ m^2/s$) and ϵ is the turbulence kinetic energy dissipation rate.

It is rather difficult to estimate ϵ because it is case-dependent, however Wilcox [25] (page 318) mentions that, in channel flow, the average dissipation is:

$$\epsilon \approx \frac{2\,u_\tau^2\,U_m}{H}\ (m^2/s^3) \qquad 3.5$$

Where U_m is the average velocity across the channel (m/s) and u_τ is the friction velocity [25].

$$u_\tau = \frac{U_m}{20}\ (m/s) \qquad 3.6$$

H is the channel height (m), which should be sufficient to accommodate the largest turbulence scale. The present case can be considered as a channel flow so that ϵ can be estimated from Eq.3.5 after replacing U_m with U_∞. Also here in the *2D* case, H refers to the domain width not the height, which follows from the physical meaning of H therefore H will be taken to be $H=h$ since this is the largest eddy in *2D*. So Eq. 3.5 becomes:

$$\epsilon \approx \frac{2\,u_\tau^2\,U_\infty}{H}\ (m^2/s^3) \qquad 3.7$$

The Kolmogorov length scale for water can then be calculated as follows:

1. Calculate U_m by enforcing geometric and dynamic similarity between experimental and numerical flow configurations, using dimensional analysis (i.e. Buckingham Π-theorem) [46]

$$Re_{exp} = Re_{numerical} \tag{3.8}$$

$$\frac{U_{exp}\, h_{exp}}{\nu_{sf}} = \frac{U_\infty\, h}{\nu_w} \tag{3.9}$$

From Sec. 2.5.4, $U_{exp}=2.24\ m/s$, $h_{exp}=3.175\times10^{-3}m$ and $\nu_{sf}=10^{-6}m^2/s$. and for the computational domain $h=40\mu m$ and $\nu_w=10^{-6}m^2/s$. By substitution into Equation 3.9, we get

$$U_\infty = 177.6\ m/s \tag{3.10}$$

2. Calculate u_τ from Eqs.3.6 and 3.10, hence

$$u_\tau = \frac{U_\infty}{20} = 8.88\ m/s \tag{3.11}$$

3. Since $H=h=40\mu m$, then

$$H = 40\ \mu m \tag{3.12}$$

4. By substitution into Eq. 3.7 and from steps 1, 2 and 3, the turbulence kinetic energy dissipation rate (ϵ) equals

$$\epsilon \approx \frac{2\, u_\tau^2\, U_\infty}{H} \approx 7\times10^8\ (m^2/s^3) \tag{3.13}$$

5. From Eq. 3.4, the Kolmogorov length scale (η) equals

$$\eta = \left(\frac{\nu_w^3}{\epsilon}\right)^{1/4} = 0.194\ \mu m \tag{3.14}$$

The energy dissipation is taking place at this value of η which will be used in the mesh generation to ensure proper representation of all length scales.

Continuum assumption

For liquids, the concept of mean free path (as interpreted for gases) does not apply since the liquid molecules experience a strong inter-molecular attraction force. Therefore the Knudsen number (*Kn*) cannot be defined in a manner similar to that for gas flows. Also the distance between molecules is very short since they can be considered to be in a constant state of collision [47] (page 49). Nguyen and Wereley [48] (page 17) stated that for water at standard conditions, the continuum assumption is valid for length scale higher than 10nm.

The mesh can be established by knowing the Kolmogorov length scale. Wilcox [25] (page 320) stated that the peak dissipation near the surface occurs from 6η to 10η. Moser and Moin [49] also noted that most of the dissipation in a curved channel happens at scales greater than 15η. Mesh resolution can be divided into three regions in both z- and x-directions as shown in Table 3.1 and Table 3.2 where γ denotes the mesh spacing normalized by the Kolmogorov length scale. Table 1.1 and Table 3.2 show that the mesh scales are less than 5.4η near the cubes and increase to about 10.73η further away from the cubes. The mesh is generated using *ICEM-CFD* under *ANSYS 12.1*. Finally, mesh skewness and aspect ratio are checked by *ICEM-CFD.* Typical values for the skewness are 1, since the mesh is rectangular and typical values for the aspect ratio range from *0.48* to *0.975*. The above-mentioned procedures are used in mesh properties for all other inter-cubes spacing and cube width.

Table 3.1: Mesh discretization in z-direction.

S/h	Region	Δz (μm)		γ_z	
		Max.	Min.	Max.	Min.
1, 1.5, 2	$-5.5 \leq z/h \leq -0.5$	2.073	1.048	10.69	5.4
	$-0.5 \leq z/h \leq 0.5$	1.026		5.29	
	$0.5 \leq z/h \leq 5.5$	2.073	1.048	10.69	5.4

Table 3.2: Mesh discretization in x-direction.

S/h	Region	*Δx (μm)*		γ_x	
		Max.	Min.	Max.	Min.
1	*-3 ≤ x/h ≤ 0*	2.081	1.048	10.73	5.4
	0 ≤ x/h ≤ 3	1.026		5.29	
	3 ≤ x/h ≤ 20	2.072	1.048	10.68	5.4
1.5	*-3 ≤ x/h ≤ 0*	2.081	1.048	10.73	5.4
	0 ≤ x/h ≤ 1	1.026		5.29	
	1 ≤ x/h ≤ 2.5	1.017		5.24	
	2.5 ≤ x/h ≤ 3.5	1.026		5.29	
	3.5 ≤ x/h ≤ 20.5	2.072	1.048	10.68	5.4
2	*-3 ≤ x/h ≤ 0*	2.081	1.048	10.73	5.4
	0 ≤ x/h ≤ 4	1.026		5.29	
	4 ≤ x/h ≤ 21	2.072	1.048	10.68	5.4

The mesh resolution effect on the results should be verified for mesh independent solution. The Strouhal number is calculated for three mesh resolutions; *85k* nodes, *223k* nodes and *387k* nodes and its typical value is *0.21*, *0.22* and *0.19* respectively as shown in Figure 3.2. It is clear that the Strouhal number is almost constant since the deviation between the maximum value and minimum value is in the order of *9%*. But because the mesh resolution provides more details of the flow pattern, the fine mesh is used in computing the following results.

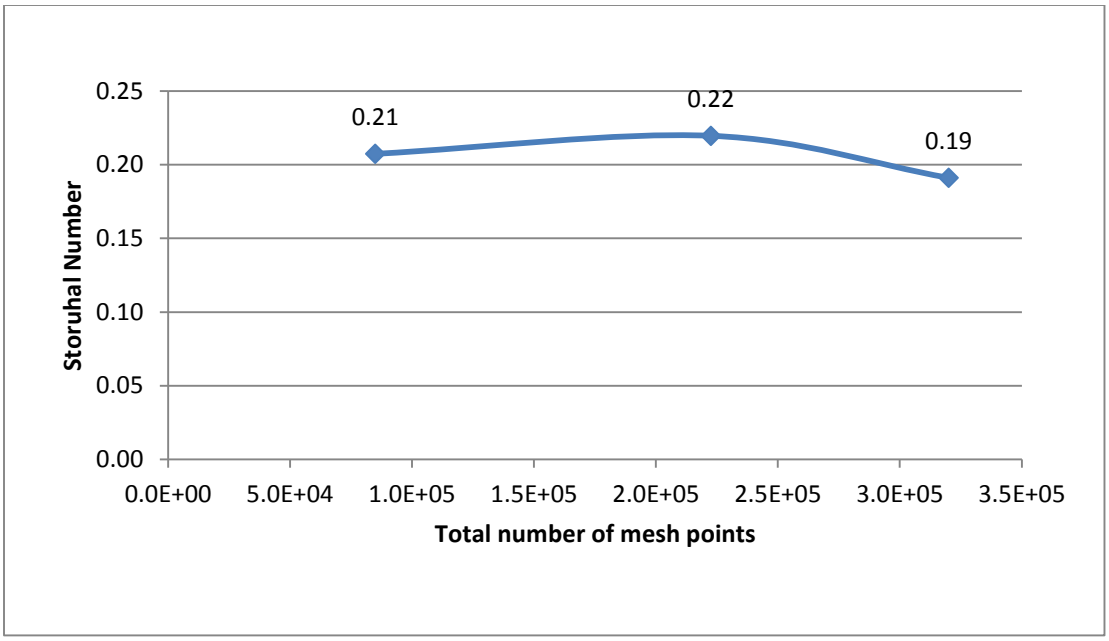

Figure 3.2: Change of Strouhal Number versus number of mesh points.

3.2.3 Boundary conditions

The inlet of the computational domain is located at $x=-3h$ where the inlet velocity is uniform and its value is $u=177.6$ *m/s* (Eq. 3.10) in the x-direction. The ambient pressure and temperature are $P=100$ *kPa* and $T=20\ ^oC$, respectively. (The flow field was found to be rather insensitive to upstream inlet distances larger than 3h, as mentioned in 3.2.1.).

Since the inlet velocity is taken to be uniform and normal to the boundary, the flow direction must be parallel to the boundary surface which is calculated at each element face on that boundary during the execution of the *CFX-Solver* [26]. The exit of the computational domain is located at $x=20h$ and is set as an 'open boundary' where the pressure and temperature are set to ambient values. The *CFX-Manual* [26] recommends that, when the numerical 'outflow boundary' passes through a region where the flow may be re-entering the computational domain such as a recirculation region or a vortex shedding region, one of the two following options should be considered: either to move the boundary away from the recirculation region (since the outflow *B.C.* does not allow the flow to re-enter) or to use the 'opening boundary' condition where simultaneous inflow and outflow

may occur. The domain side-walls at $z=\pm 5.5h$ and the cubes surfaces are set as no slip walls and the boundaries at $y=\pm 0.0125h$ are set as symmetry planes.

Initial conditions and temporal resolution

The steady state solution obtained on the same mesh and with the same boundary conditions is taken as the initial condition for the time accurate *DNS* computation. The steady state solution is assumed to be converged either when the normalized *RMS* of the governing equations drops to 10^{-8} or after *2,000* iterations, whichever happens first.

The total physical time is chosen to be $t_{tot}=10^{-4}s$, and the time step is given by the Kolmogorov time scale (t_η) and is calculated as follows [25]:

$$t_\eta = \left(\frac{\nu_w}{\epsilon}\right)^{1/2} = \frac{\eta^2}{\nu_w} \qquad 3.15$$

By substituting for η from Eq. 3.14, then $t_\eta=8.45\times10^{-8}s$. Accordingly, the time step used in all cases was set $\Delta t=10^{-8}s$ which results in 10^4 time steps. At each time step, the number of iterations on the stationary problem is set to a maximum of *10* or is stopped when the $RMS=10^{-8}$.

The effect of the time step on the Strouhal number is checked by taking three values of time step; 10^{-6}, 10^{-7} and 10^{-8} *s* for the same mesh resolution as shown in Figure 3.3. The vortex shedding is not detected at the larger time step, 10^{-6}, but it is detected at the other two values, which are less than or close to the Kolmogorov time scale ($t_\eta=8.45\times10^{-8}s$). Moreover, the smaller time step, 10^{-8}, gives a more detailed flow pattern. In other words, the transient nature of the flow is well captured when the time step is equal to or less than the Kolmogorov time scale. This nature is characterized by the appearance of shear layers downstream of the cubes, leading to the shedding, splitting, merging and finally the dissipating of vortices. But when the time step is larger than the Kolmogorov time scale, these temporal features are either poorly captured or completely missed, which is reflected in Figure 3.3 where the Strouhal number values are misleading.

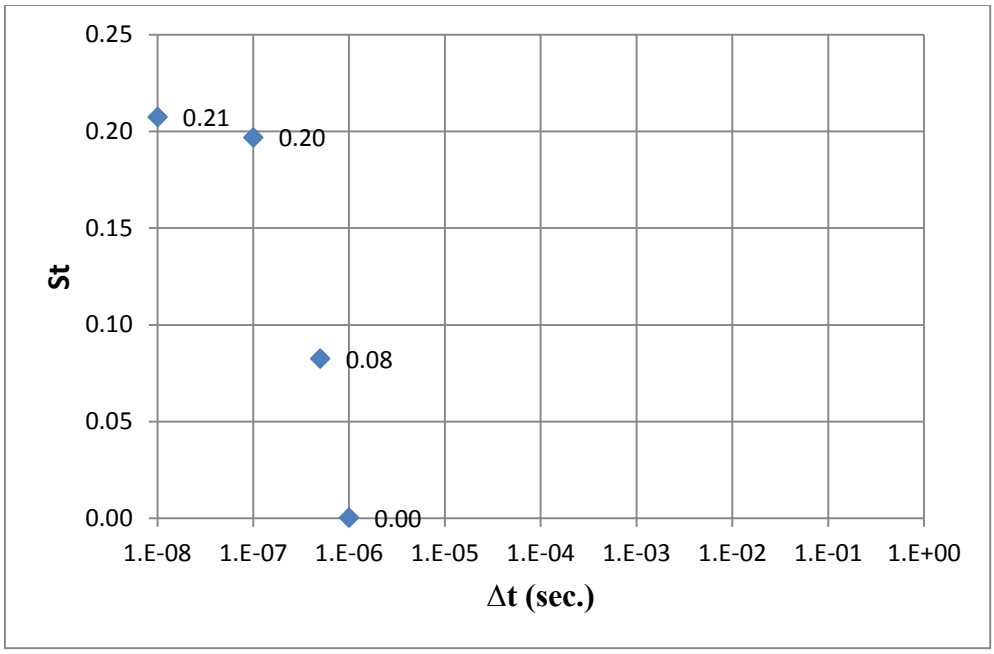

Figure 3.3: Strouhal number versus time step.

As the physical time advances, the flow field is captured and recorded into a file every $10^{-6}s$ resulting in *100* instantaneous flow fields. Moreover, probing points at pre-selected space locations are used to monitor all the flow properties and variables at each time step. A sensitivity analysis of the spacing between the two cubes was carried out only numerically, and the corresponding computational domain, mesh size and information on computing time, are given in Table 3.3.

Table 3.3: Computational domain, mesh and CPU data.

S/h	Domain $L_x \times L_y \times L_z$	Total no. of nodes	No. of *CPU*		*CPU* hours	
			Steady	Unsteady	Steady	Unsteady
1	*23h* × *11h* × *h*	386,992	4	32	17.78	3,283.39
1.5	*23.5h* × *11h* × *h*	399,152	28	40	62.72	3,388.89
2	*24h* × *11h* × *h*	410,704	36	36	68.5	3,500

The physical implication of the block spacing will be discussed in the following section.

3.3 Results and discussion

3.3.1 Numerical validation

In this section, the *2D* numerical solution is compared with the experimental work qualitatively and quantitatively in terms of flow pattern and vortex shedding frequency, respectively.

Figure 3.4 presents a qualitative comparison of an instantaneous flow field for the same geometry and Reynolds number (see Figure 2.5b) where both “Panel a” and “Panel b” have very similar flow patterns. In region "A", vortices are shed from the sides of the cubes and from the inter-cube region. Vortices shed on the right side of the cubes are stronger than those shed on the left side. In Region "B", vortex shedding starts in the near-wake region behind the downstream cube in the form of small vortices. Both figures have vortex "C" with a small tail. Region "F", shown in the two figures, represents a region of more developed vortex shedding and has the same vortex number and behavior. One can conclude that the numerical flow field gives very good qualitative agreement with the experimental one.

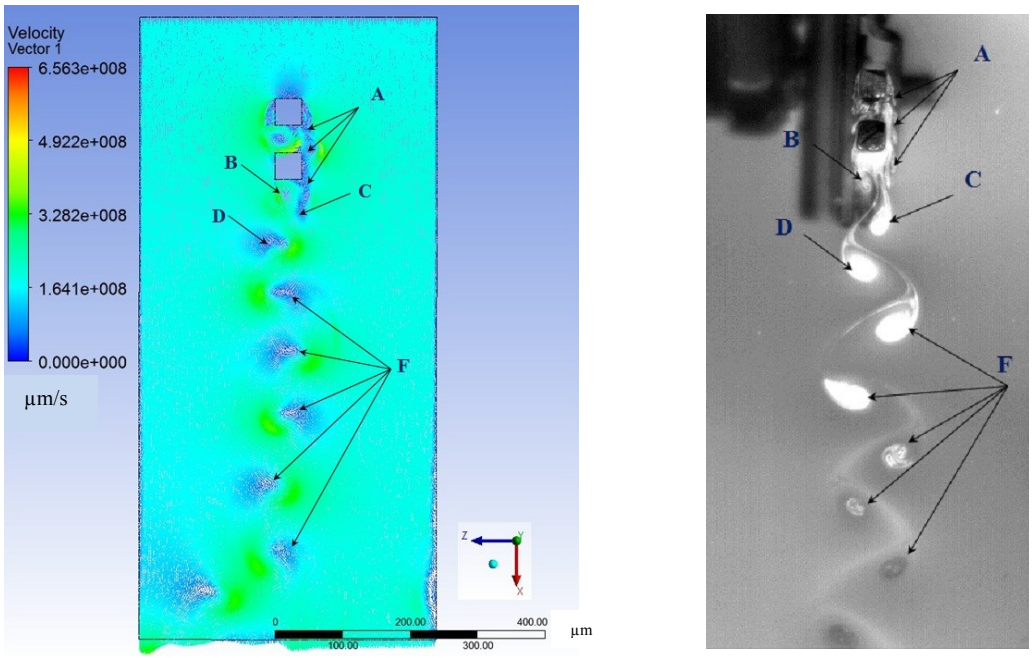

(a) Numerical flow field. (b) Experimental flow field.

Figure 3.4: Comparison between the numerical and experimental instantaneous flow field at *Re=7103* and *S/h=1*.

The vortex shedding frequency equals $5.332\times10^{6}\ rad/s$ (i.e. $f_{num}=848.61\ kHz$) as calculated in the next section hence the numerical value of Strouhal number is:

$$St_{num} = \frac{f_{num}\, h}{U_{num}} = 0.19 \qquad 3.16$$

Comparing this numerical value with the experimental one, given as *0.2* in Eq. 2.2, one finds that the agreement is within *5%*. Therefore one can conclude that the numerical solution achieved an acceptable qualitative and quantitative agreement with the experimental results.

3.3.2 Two-dimensional numerical cases

In this section, the results obtained for the *2D* cases are presented and discussed.

Vortex shedding frequency

Several probing points are spread along the streamwise (x) and spanwise (z) directions, as shown in Figure 3.5. The distribution of probing points differs slightly with the different spacing cases.

Eighteen flow variables and fluid properties are captured at each probing point during the simulation time, with the cross flow velocity, w, being used to demonstrate the temporal flow variation. This velocity, w, was chosen as it is directly related to the vortex shedding. In other words, the value of this velocity would be approximately zero in the absence of any vortex shedding. Figure 3.6a, b and Figure 3.6c show the variation of the crossflow velocity component, w, versus time at a probing point located at $z/h=0$ (symmetry plane) and $x/h=5$ downstream of the second cube, for several values of cube spacing. Fluctuation in the value of the velocity, w, typically indicates a vortex passing by these points.

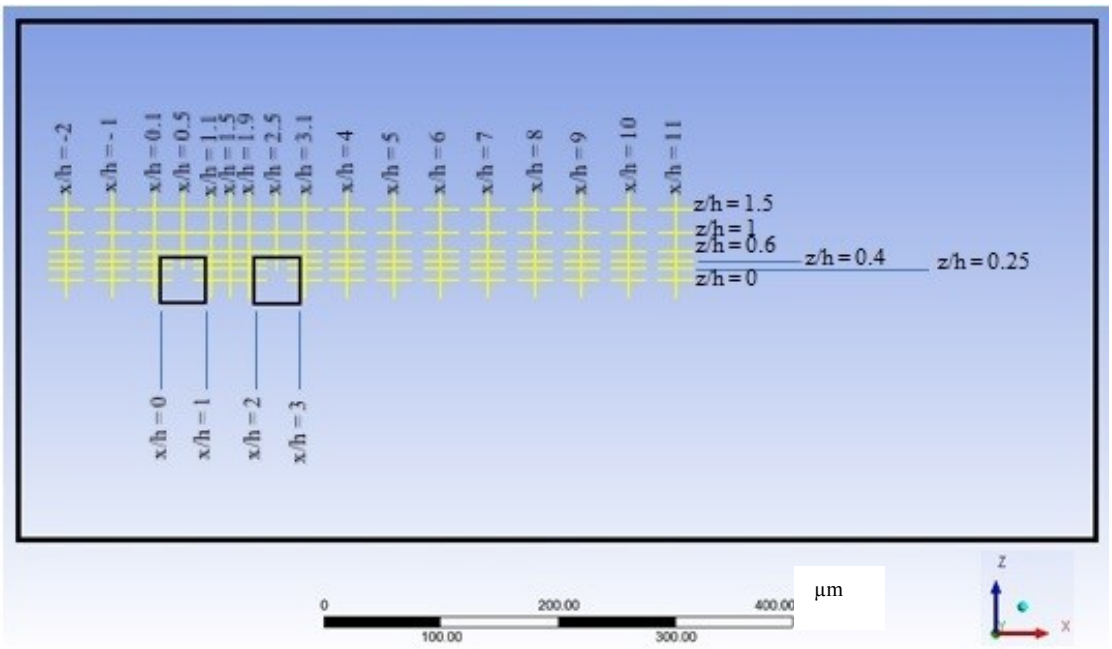

Figure 3.5: The probing points distribution in the computational domain for *S/h=1*.

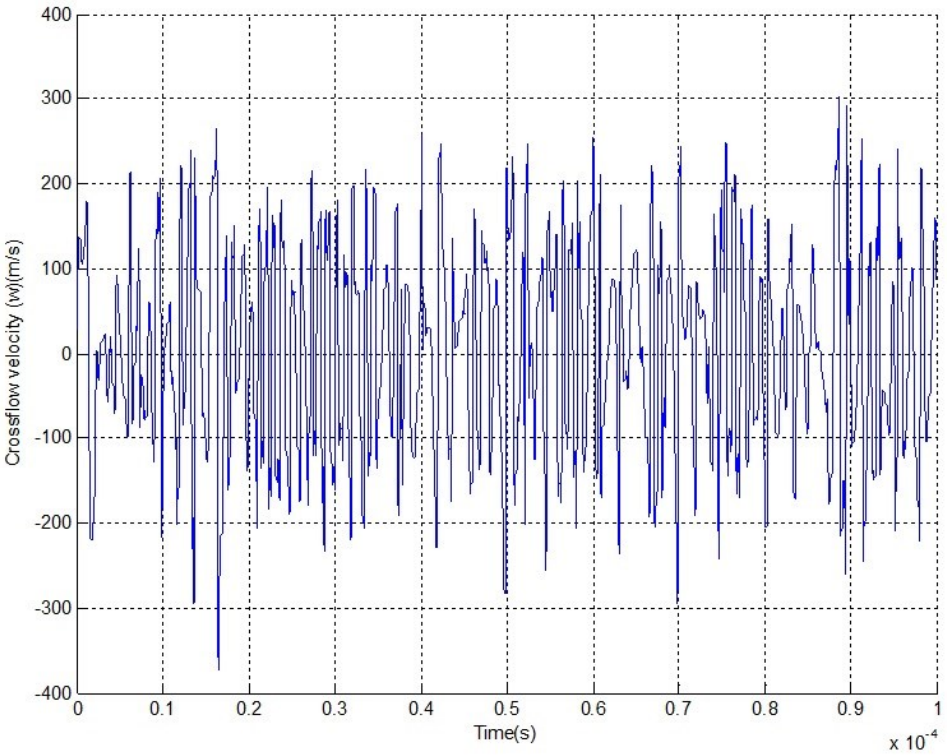

(a) S/h=1

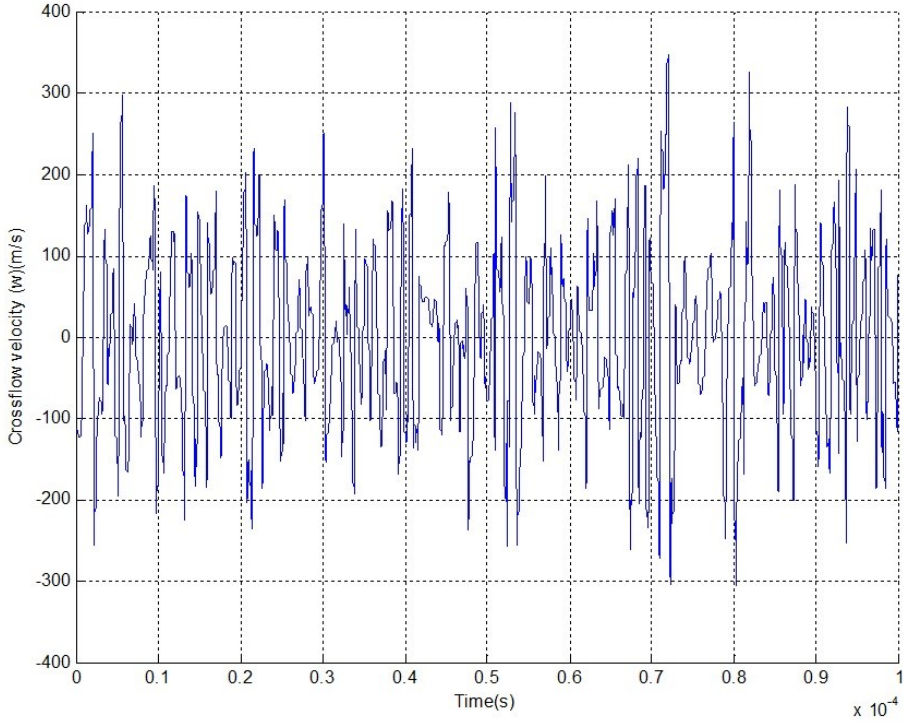

(b) S/h=1.5

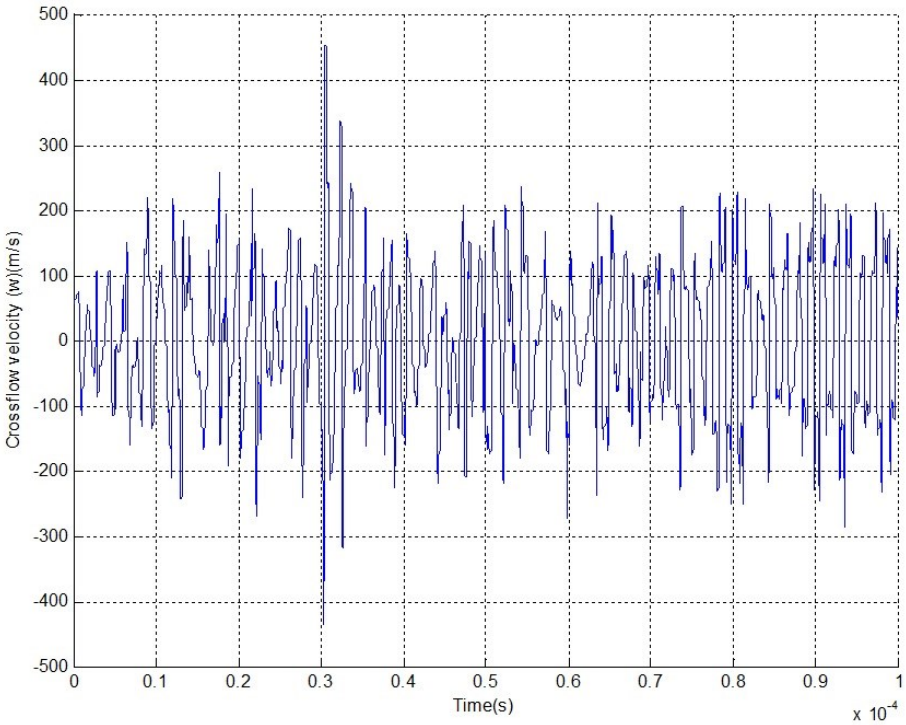

(c) *S/h=2*

Figure 3.6: Time trace of the crossflow velocity (*w*) on the symmetry plane (*z/h=0*) at *x=5h* downstream of the second cube.

The Discrete Fourier Transform (*DFT*) is a very powerful tool used in physics to detect the dominant frequency components of a temporal signal or the momentum distributions of particles; its purpose being to decompose a temporal function into an infinite sine or cosine series (which are orthonormal Eigen functions). In the present work, it is applied to the time trace of the cross-flow velocity, *w*, at all probing points to examine the frequency content in the signal. The *DFT* is computed using *Matlab R2009b*. The *DFT* revealed that there is either one or two dominant frequencies, or that there is no dominant harmonic signal, depending on the inter-cube spacing and Reynolds number. Figure 3.7 show the frequency spectrum of the cross-flow velocities given in Figure 3.6. Figure 3.7a shows that there is a range of dominant frequencies at that downstream location, *x/h=5*. Moreover, Table 3.4 shows that there are two dominant frequencies, one in the near field (*St=0.101*) and one in the far field (*St=0.171*).

It could be that the vortex shedding is intermittent, as observed by Havel *et al.* [37]. For *S/h=1.5*, Figure 3.7b shows that there is one dominant frequency (from Table 3.4, *St=0.108* in the near and far field) and possibly *2* or more secondary ones. When *S/h=2*, Figure 3.7c shows that there is only one dominant frequency (*St=0.149*, see Table 3.4).

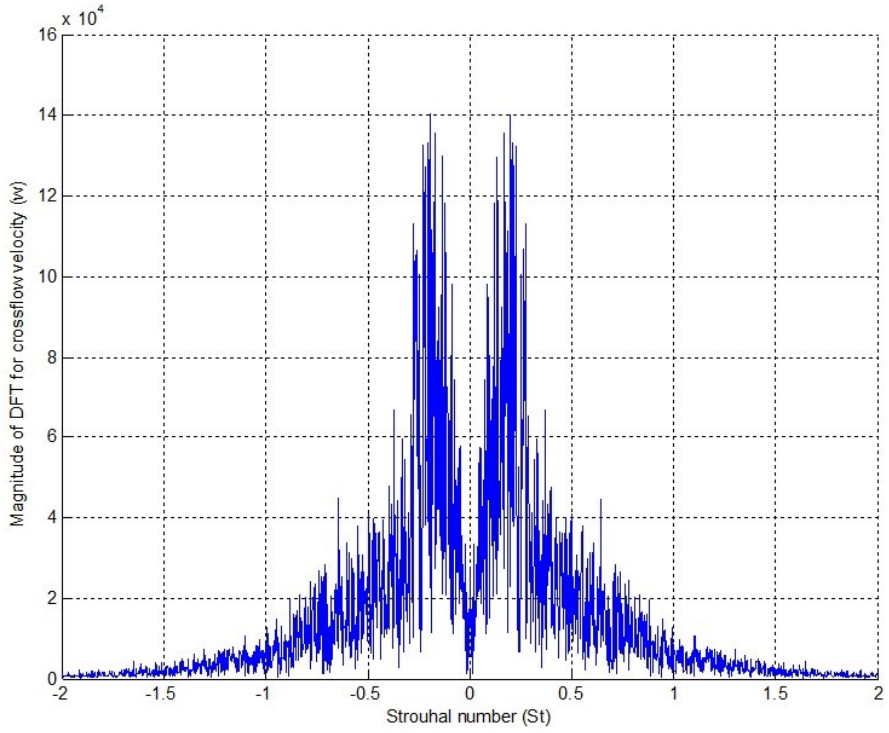

(a) S/h=1

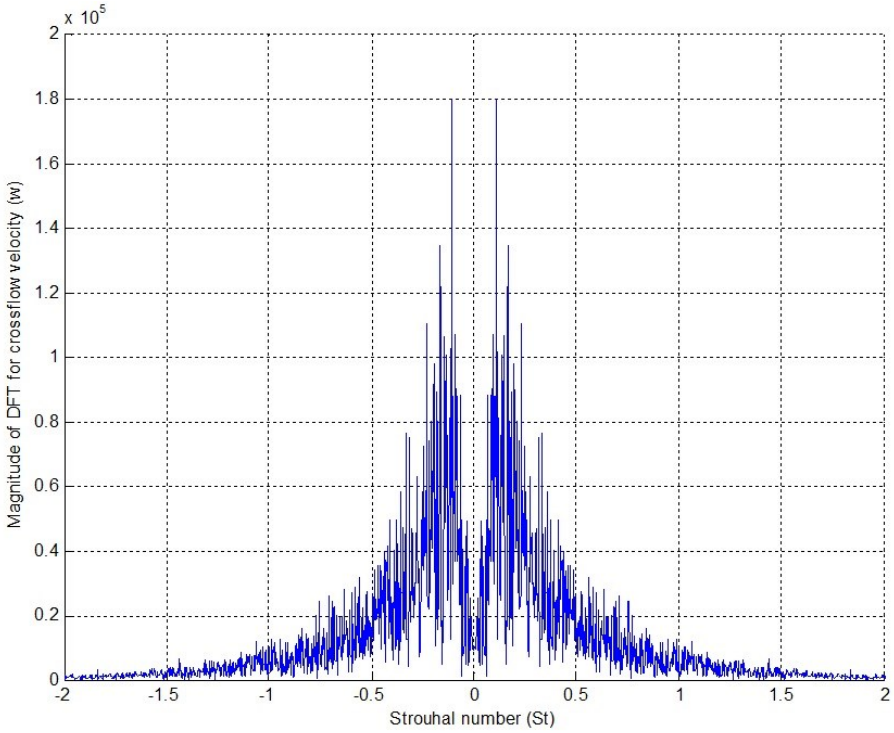

(b) S/h=1.5

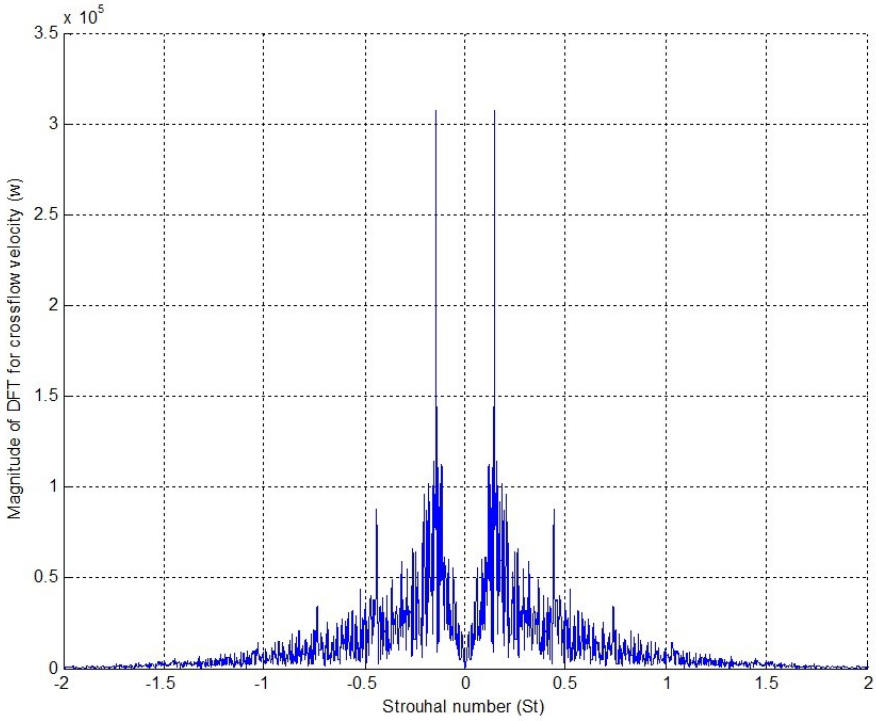

(c) *S/h=2*

Figure 3.7: Strouhal number on the symmetry plane (*z/h=0*) at *x=5h* downstream of the second cube.

The observations made on Figure 3.7 are supported by the values of *St* in the near wake and far wake regions given in Table 3.4. One observation to be made from Table 3.4: is that the Strouhal number starts at a *0.171* at *S/h=1*, drops to *0.108* and then increases asymptotically with increasing *S/h* towards *St* for *S/h*≈∞. This trend is also observed experimentally by Havel *et al.* [37].

Table 3.4: Local Strouhal number at *Re=7103*, *2D* flow.

S/h	Near-Field	Far-Field
1.0	0.101	0.171
1.5	0.108	0.108
2.0	0.149	0.149
2.5	0.151	0.171
3.0	0.194	0.194

The total number of probing points behind *SE* is *54* for *S/h=1* and *102* for both *S/h=1.5* and *S/h=2*.

Figure 3.8 shows the variation of the dominant Fourier component for each crossflow velocity, *w*, downstream of the second cube. The signal behavior is similar in the different *z*-planes, however it is strongly affected by the cubes spacing, *S/h*. Figure 3.8 shows that the dominant Fourier component, in cases of *S/h=1*, *2*, *2.5* and *3*, first increases downstream of the second cube up to *x/h=0.5-1* and then decreases continuously. This is the near wake region (*x/h=0-1*) behind the second cube where small-scale instabilities resulting from the separation of the shear layer and floe recirculation result in a large unsteady transverse velocity. As *x/h* increases indefinitely, the crossflow velocity amplitude seems to be decreasing at a constant rate reflecting the diffusion of these vortices into the flow as it convects downstream.

In the case of *S/h=1.5* the signal behavior is, to a certain extent, reversed. The dominant Fourier component increases at around 7h downstream of the second cube, as shown in Figure 3.8b. It is believed that, for the case of *S/h=1.5*, this increase in the *DFT* of the crossflow velocity beyond *x/h=10* is non-physical; rather it is numerical, and can be interpreted as follows. The interaction of the vortices that are shed from the two cubes

increase the vortex disturbance in the exit flow region where an 'open boundary' condition is applied. For an 'open boundary' the value of static pressure is interpreted as relative total pressure for inflow - a poor assumption in an exit flow with a relatively strong vortex convecting downstream - and relative static pressure for outflow. Along part of the 'open boundary' where the flow is entering into the computational domain, the velocity component normal to the boundary must also be specified which results in the development of a mass influx over that part of the 'open boundary'. The magnitude of the velocity at the 'open boundary' is then part of the solution and propagates into the exit flow region contaminating it with errors.

One last observation on Figure 3.8 is that, downstream of the maximum signal, the cross-flow velocity is highest (on average) on the cubes centerline *z/h=0* for all spacing values.

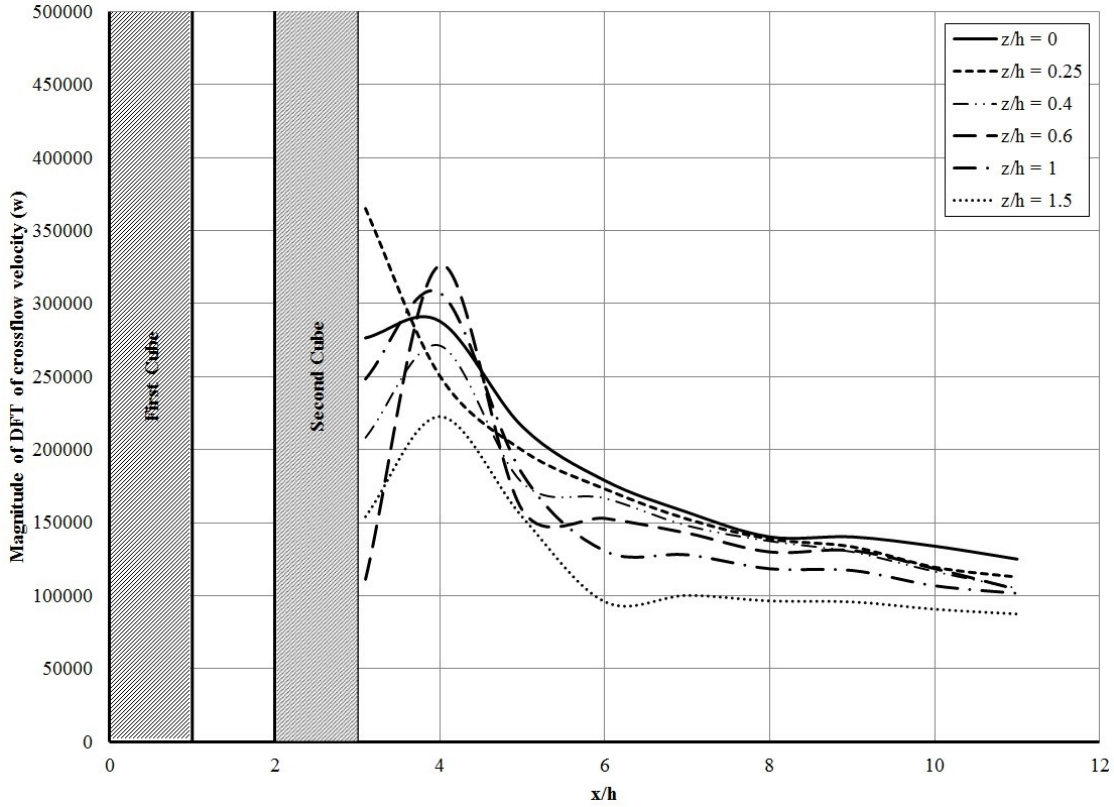

(a) S/h=1

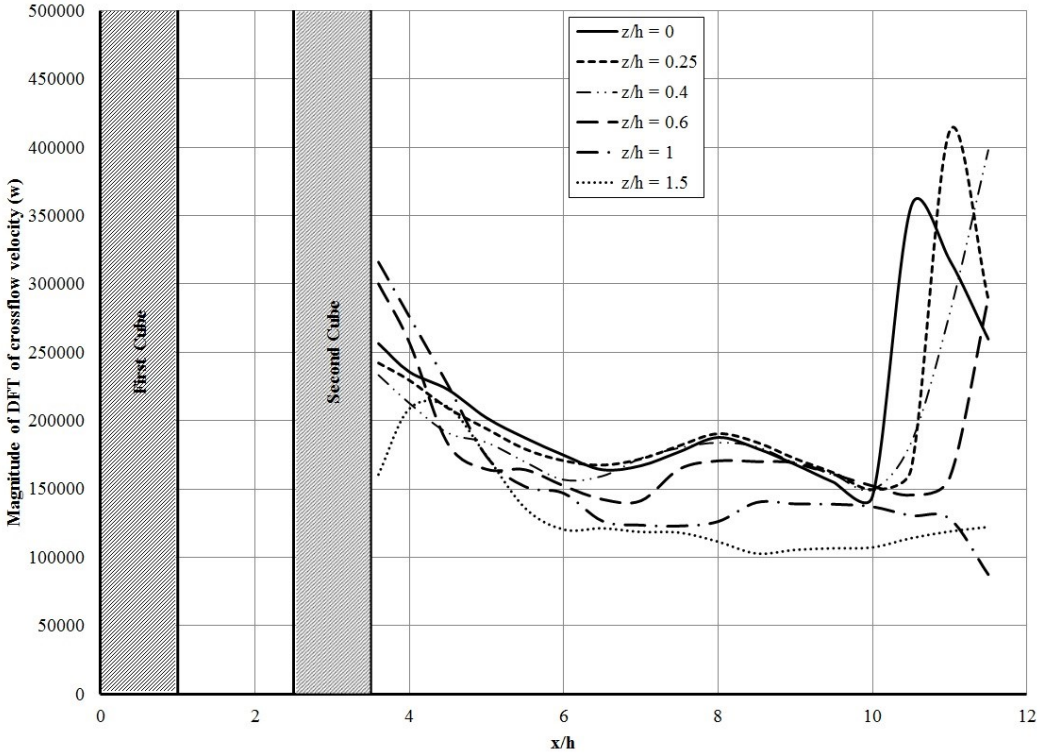
z/h = 0
z/h = 0.25
z/h = 0.4
z/h = 0.6
z/h = 1
z/h = 1.5
First Cube
Second Cube
Magnitude of DFT of crossflow velocity (w)
x/h
0
50000
100000
150000
200000
250000
300000
350000
400000
450000
500000
0
2
4
6
8
10
12

(b) S/h=1.5

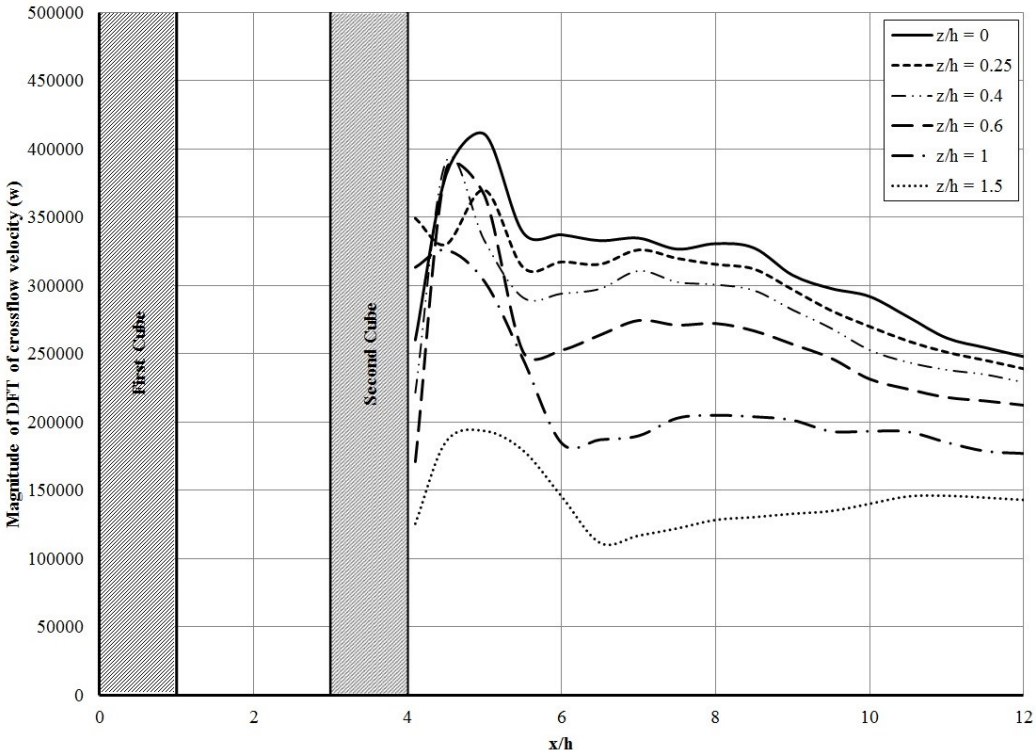
z/h = 0
z/h = 0.25
z/h = 0.4
z/h = 0.6
z/h = 1
z/h = 1.5
First Cube
Second Cube
Magnitude of DFT of crossflow velocity (w)
x/h
0
50000
100000
150000
200000
250000
300000
350000
400000
450000
500000
0
2
4
6
8
10
12

(c) *S/h=2*

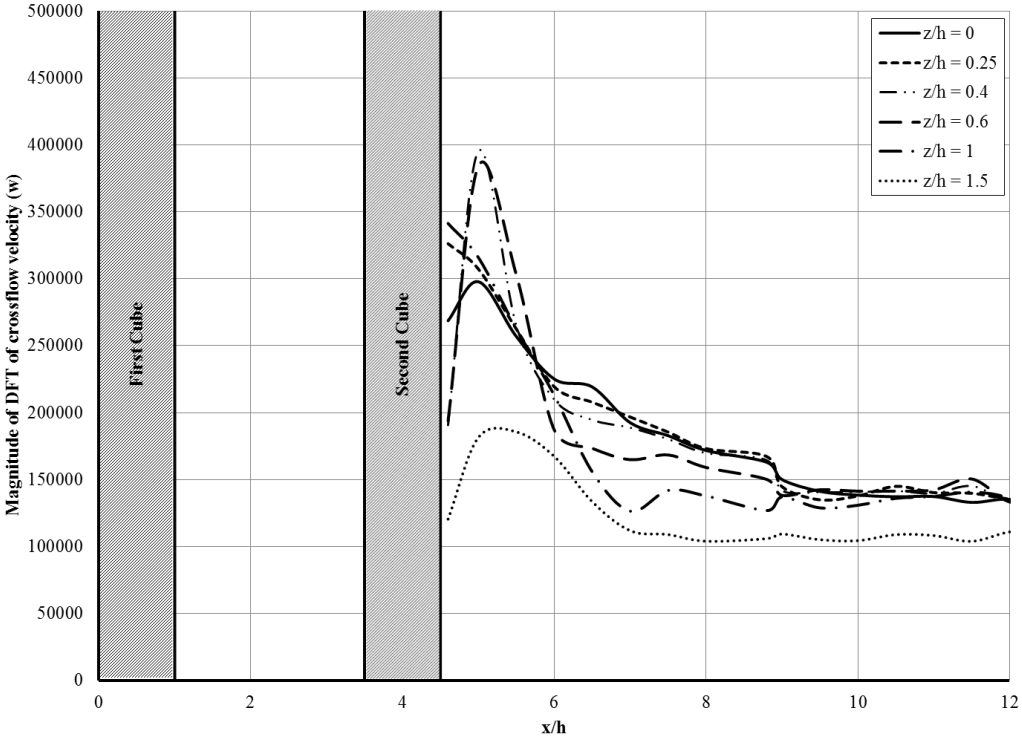

(d) *S/h=2.5*

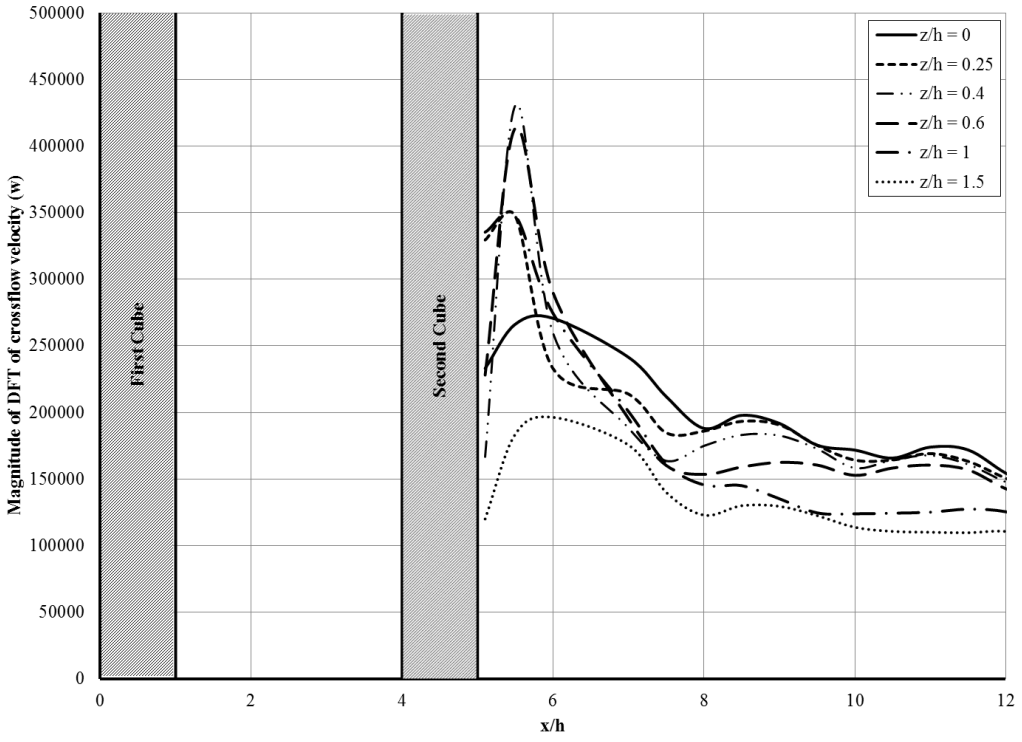

(e) *S/h=3*

Figure 3.8: Dominant Fourier component of the crossflow velocity w.

Figure 3.9 shows the downstream variation of Strouhal number corresponding to the dominant Fourier component of the crossflow velocity, *w*. It is worth noting that Strouhal number is roughly constant at the probing points located on the symmetry line *z/h=0* (symmetry plane in *3D*) for values of *x/h>6*.

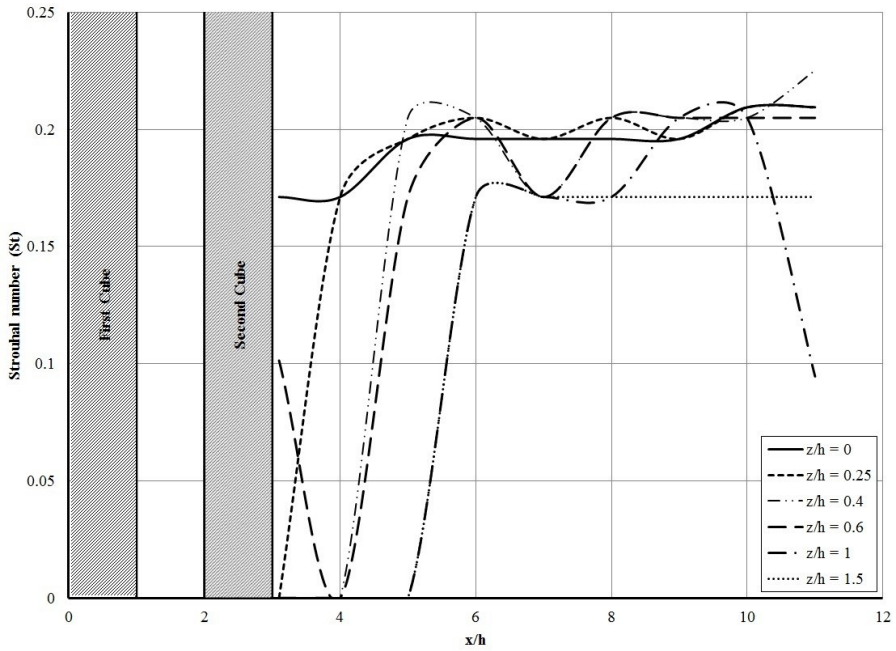

(a) S/h=1

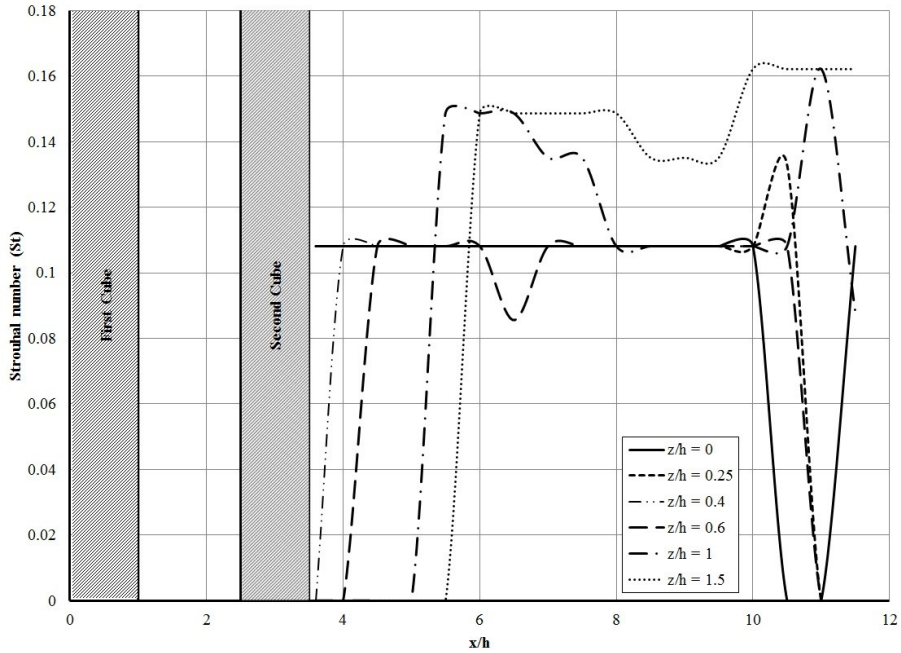

(b) S/h=1.5

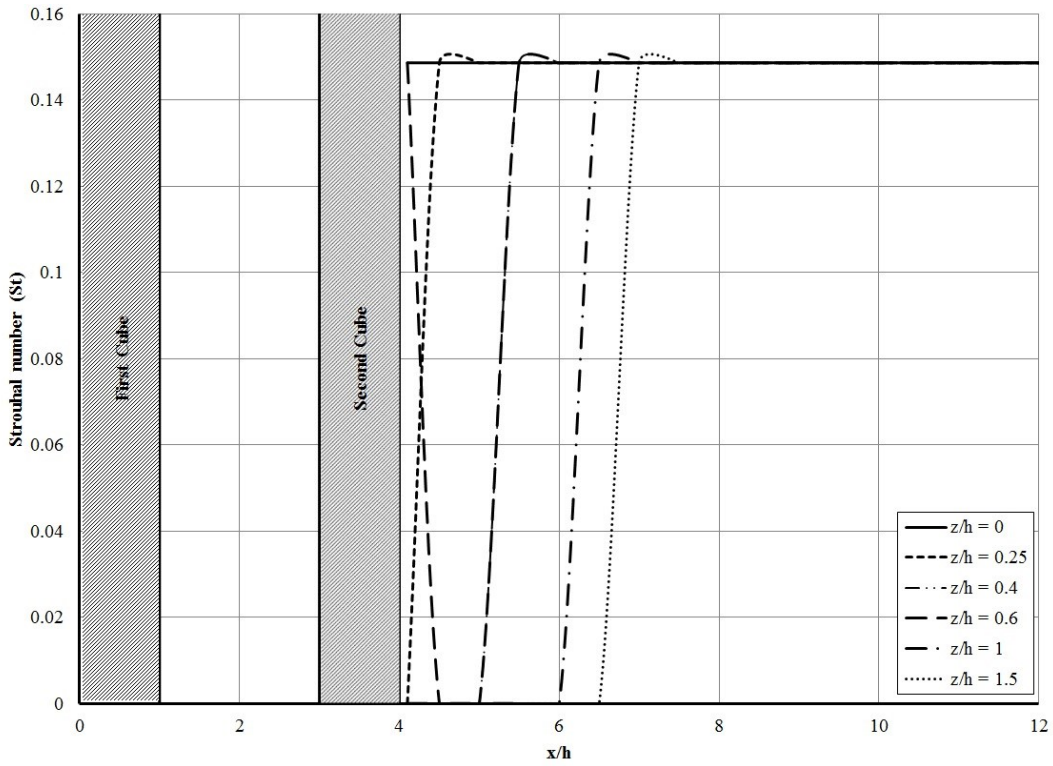

(c) *S/h=2*

Figure 3.9: Strouhal number behind the downstream cube.

More precisely, Strouhal number increases up to *x/h=3* as measured from the trailing edge of the second cube and then remains constant. The exception to this behavior is in the case of *S/h=1.5* where two things happen: 1- For *x/h>10* as was discussed in the interpretation of Figure 3.8 the numerical computations are inaccurate due to the boundary condition implementation at exit; 2- For *5<x/h<10,* there is a 2nd value of *St* number occurring at *z/h=1* and *1.5*, i.e. at the outskirts of the far-wake region, that could indicate the presence of an intermittent vortex shedding in that area.

A representative Strouhal number for each *S/h* is calculated by averaging the values observed at all the probing points behind the *SE* at $x/h \geq 6$. These values are then plotted as shown in Figure 3.10. This figure shows that the Strouhal number is a function of cube spacing, it reaches its highest value of *0.21* at *S/h=0.5* and its lowest value of *0.1* at *S/h=1.5*. As *S/h* increases towards infinity, *St* seems to asymptote to a value around *0.15*. In fact, several researchers found experimentally that *S*t follows the same trend as that obtained

numerically. Moreover the value of *St* prevailing for a single cube far downstream was found to be between *0.123* and *0.131* [25, 37] depending on the researcher.

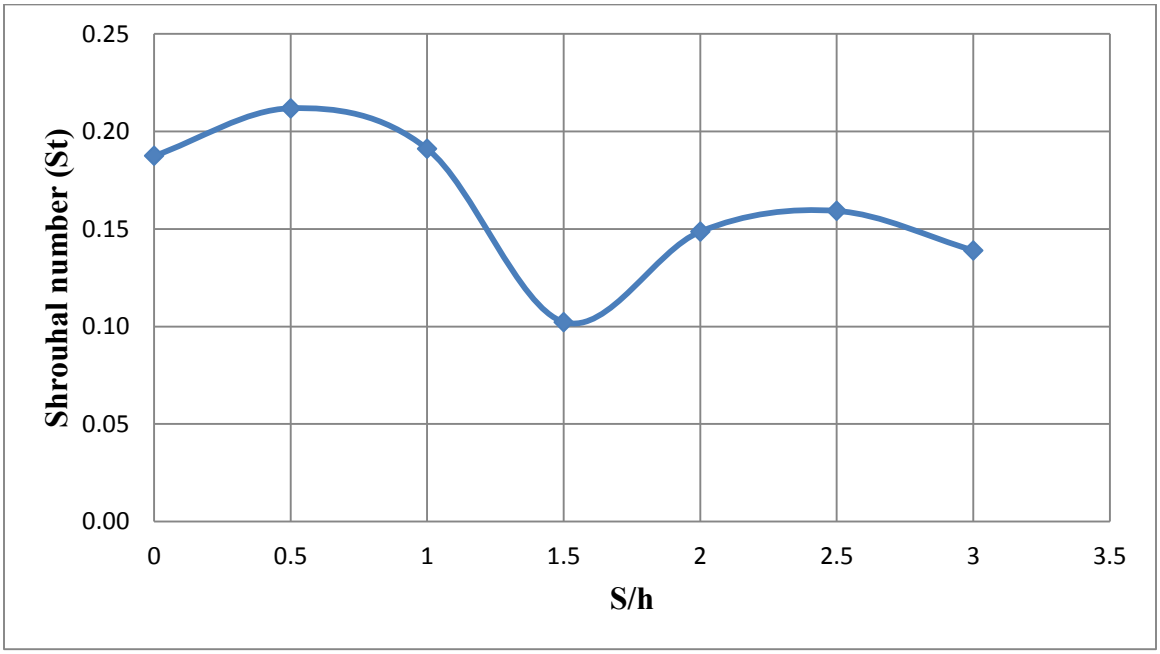

Figure 3.10: Variation of Strouhal number with cubes spacing.

In the cases of $S/h \leq 1$, which include $S/h=0$, 0.5 and 1, Strouhal no. is relatively high ($St \approx 0.2$) due to the high vortex shedding frequency. The small spacing between the cubes prevents the initiation of vortex shedding in the inter-cube cavity and produces a continuous shear layer on both sides of the cubes, i.e. both cubes are seen by the flow as one long bluff body as shown in Figure 3.12. Figure 3.9a also shows that $St \approx 0.2$ at $S/h=1$ at all probing points.

In the case of $S/h=1.5$, the fact that St is at its minimum value, may be attributed to the nonlinear interaction between the vortex shedding in the inter-cube cavity and the downstream flow. Similar behavior was observed by Takeuchi and Matsumoto [50]. Also the continuous side vortex between the two cubes disappeared, as shown in Figure 3.12**.**

In the case of $S/h \geq 2$, vortices are shed from both cubes and convect downstream. But the vortex strength and vortex shedding behind the upstream cube are weaker in comparison with that of the downstream cube. So the vortex shedding frequency is mainly controlled by the second cube. Hence $S/h \geq 2$ gives a Strouhal number lower than that observed at $S/h \leq 1$ but, as shown in Figure 3.7c, the signal is stronger and clearer than the one occurring

at *S/h=1.5*. The frequency value is also independent of the measuring probe location, as shown in Figure 3.9c.

Figure 3.11 shows that the average Strouhal number does not vary with *Re* in the given range (*7103-14660*) and assumes the value *St=0.19*. This result is compatible with the findings of Kim and Durbin [18] who demonstrated that, for spheres in uniform flow where the Reynolds number range is *800< Re <200,000*, there co-exist two values of the Strouhal number. The lower frequency is attributed to the large-scale instability in the far-wake. It is independent of Reynolds number *Re* and is approximately equal to *0.2*. This is in agreement with the numerical simulation predictions and the experimental measurements. However due to the limited computational resources available, it was not possible to explore a wider range of Reynolds numbers. Note that the above mentioned finding as well as the value of St seem to be insensitive to the object geometry (sphere vs cube).

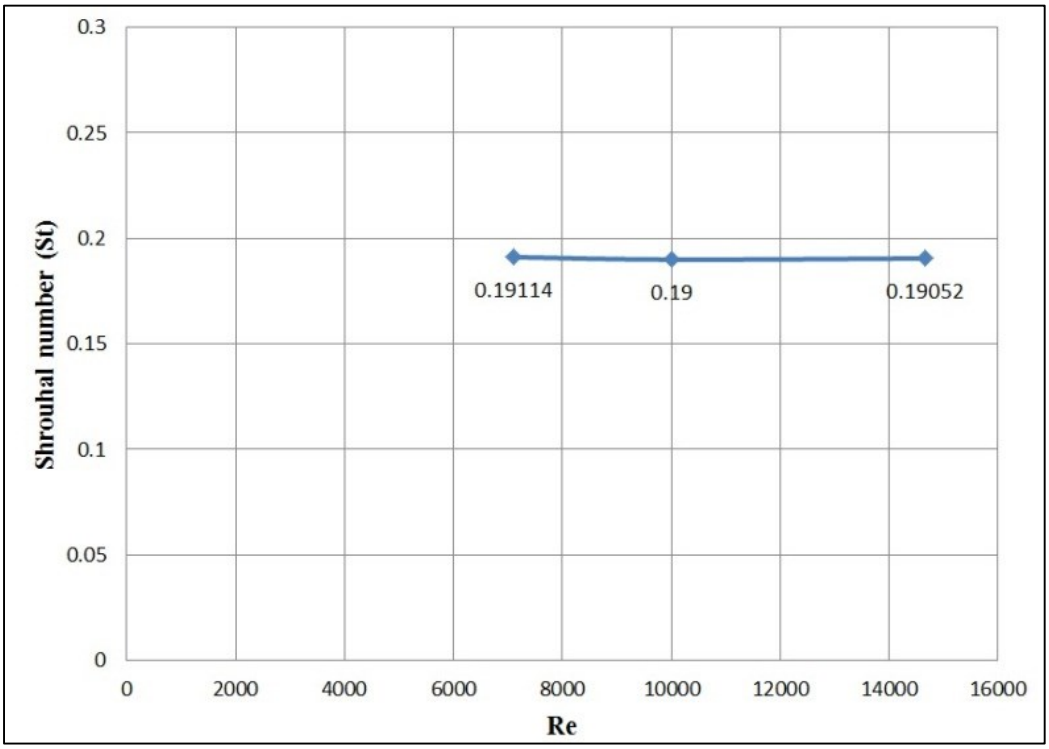

Figure 3.11: Strouhal number versus Reynolds number at *S/h=1* and *L/h=1*.

3.3.3 Numerical flow visualization and interpretation

In this subsection the flow pattern is reproduced at block spacings of *1*, *1.5* and *2*. Some flow features are noted and results are interpreted accordingly.

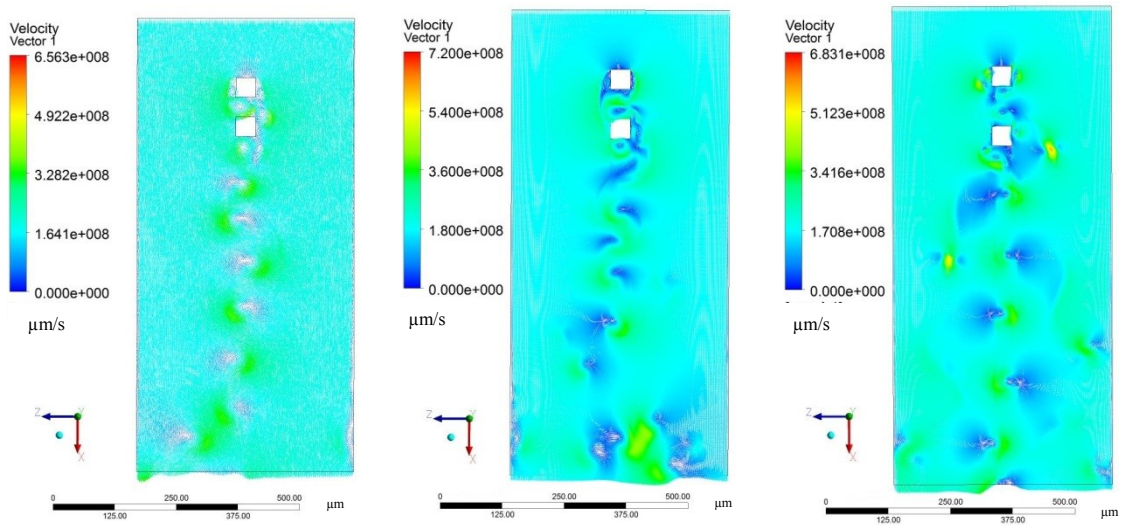

(a) S/h=1 *(b) S/h=1.5* (c) *S/h=2*

Figure 3.12: Flow pattern (velocity vector) in the *xz* plane for several *S/h* and *Re=7103*.

Figure 3.13 shows contour plots of the turbulent kinetic energy in the *xz* plane. The turbulent kinetic energy is defined as, see Ferziger, [24] (page 274):

$$K = \frac{1}{2}\left(\overline{u'^2} + \overline{v'^2} + \overline{w'^2}\right) \qquad 3.17$$

Where: $\overline{v'^2} = 0$ for *2D* simulations.

Figure 3.13 shows that the flow is laminar upstream of the 1st cube. It is tripped to turbulent flow as it turns around the cube side due to flow separation and reattachment and the associated pressure gradients. Another observation is that, except for *S/h=1*, the turbulent kinetic energy patterns downstream of the second cube are similar, which suggests that the turbulence generation mechanism is unaffected by the presence of the 1st cube. For *S/h=1.5*, Fig. 3.13b, the numerical error due to the choice of exit boundary condition manifests itself as a non physical increase in *K* at the wall-exit corner. For *S/h=1.5*, the flow pattern in the inter-cube region shows a stronger interaction due to the proximity of the two cubes., All these figures however, emphasize that the flow field and Strouhal

number are very sensitive to the inter-cube spacing as it controls the vortex formation and shedding in the inter-cube cavity.

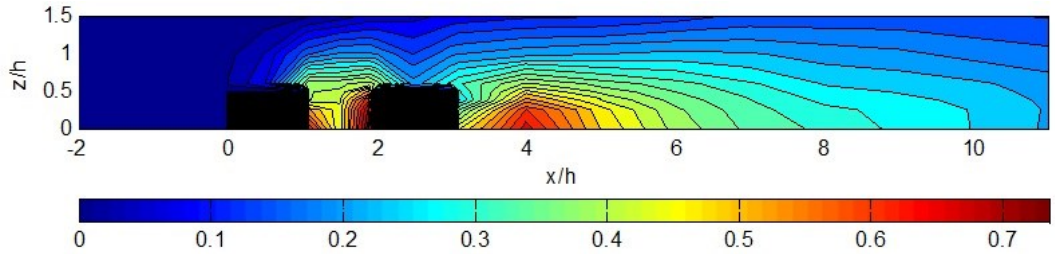

(a) S/h=1

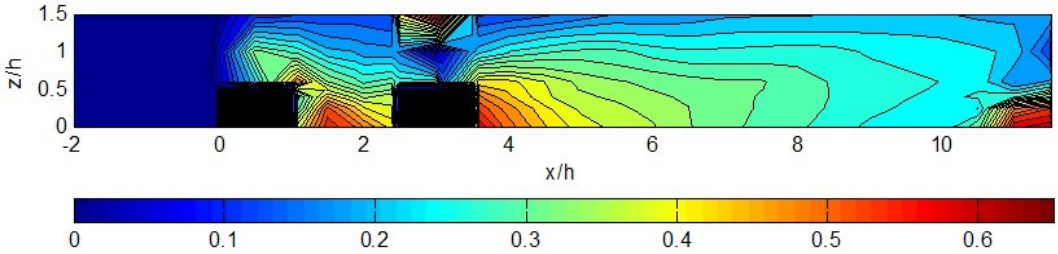

(b) S/h=1.5

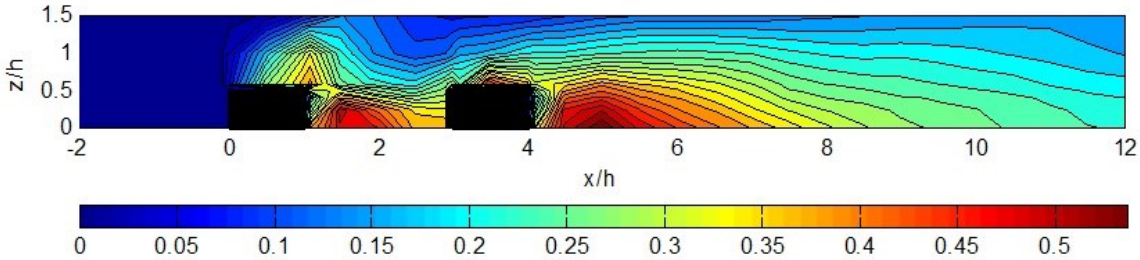

(c) *S/h=2*

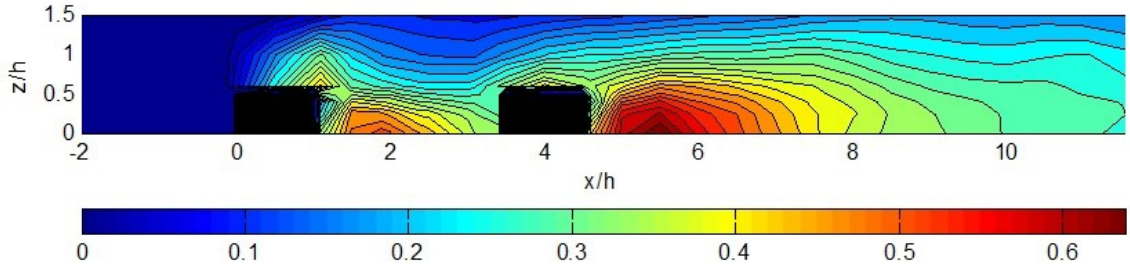

(d) *S/h=2.5*

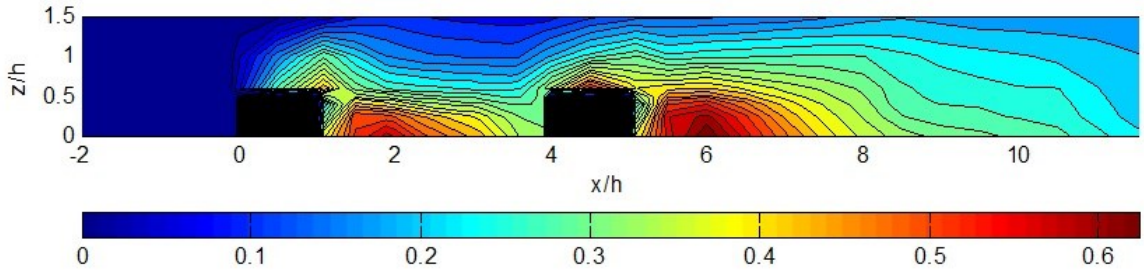

(e) *S/h=3*

Figure 3.13: Contour plots of turbulent kinetic energy K/U_m^2 in the *xz* plane.

3.3.4 Parametric study

Since the targeted application is that of two bluff bodies in tandem, the *BE* and *SE*, an attempt is made in this section at providing some insight on the choice of the proposed sensor geometry. To this end, a parametric study on the effect of changing the distance between the two cubes (*S*) and the thickness of the second cube (*L*) on the Strouhal number will be studied for Reynolds number values of *7103*, *10000* and *14660*.

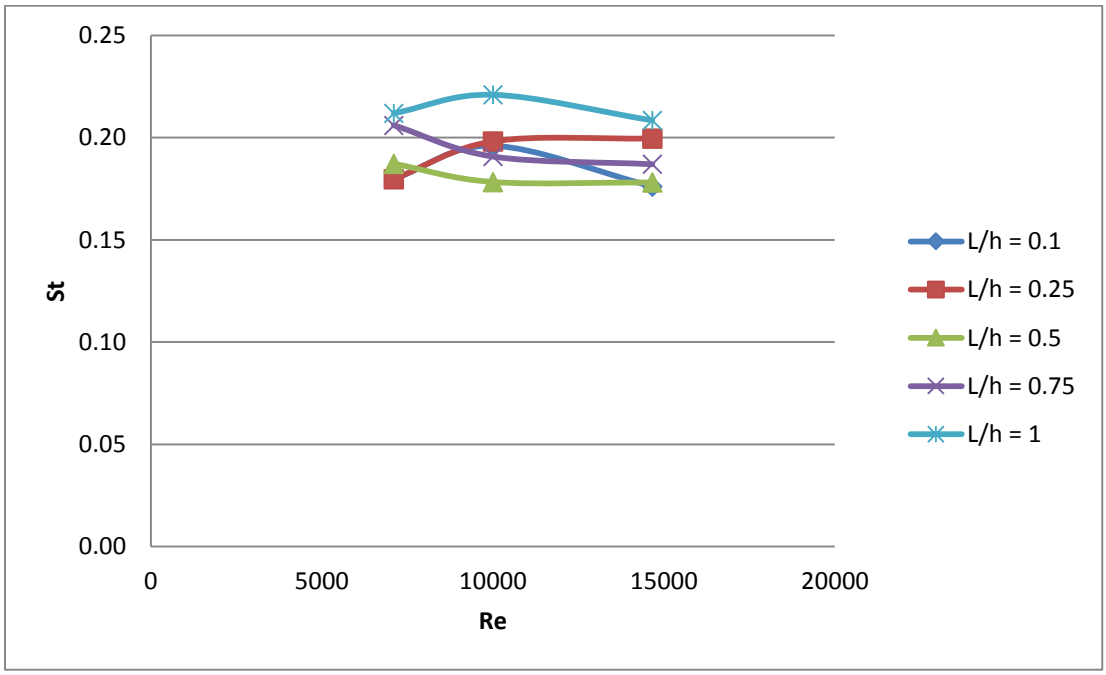

Figure 3.14: Strouhal number versus Reynolds number at *S/h=0.5* at several *L/h*.

Figure 3.14 shows *St* number at several *Re* numbers when the spacing is fixed at *S/h=0.5*. It is clear that *St* number is almost constant with *Re* number at several *L/h*, where the standard deviation is around *0.015*. The average value is also the same as that of *St* number for *S/h=1* and *L/h=1* for several *Re* number as shown in Figure 3.11.

Changing S and L

The inter-cubes spacing (*S/h*) is varied from *0* to *3* by steps of *0.5*. For each *S/h* the ratio of the second cube thickness and its side (*L/h*) assumes the values *0.1*, *0.25*, *0.5*, *0.75* and *1*. The Strouhal number is calculated for each case and its values are listed in Table 3.5 and plotted in Figure 3.15, showing no clear trend for Strouhal number with the change of the two ratios *S/h* and *L/h*.

Table 3.5: Strouhal number at several *S/h* and *L/h*.

S/h	***L/h***				
	0.1	**0.25**	**0.5**	**0.75**	**1**
0	0.20	0.18	0.18	0.18	0.19
0.5	0.18	0.18	0.19	0.21	0.21
1	0.18	0.15	0.20	0.17	0.19
1.5	0.15	0.16	0.12	0.12	0.10
2	0.16	0.16	0.14	0.12	0.15
2.5	0.14	0.15	0.15	0.15	0.16
3	0.12	0.15	0.17	0.13	0.14

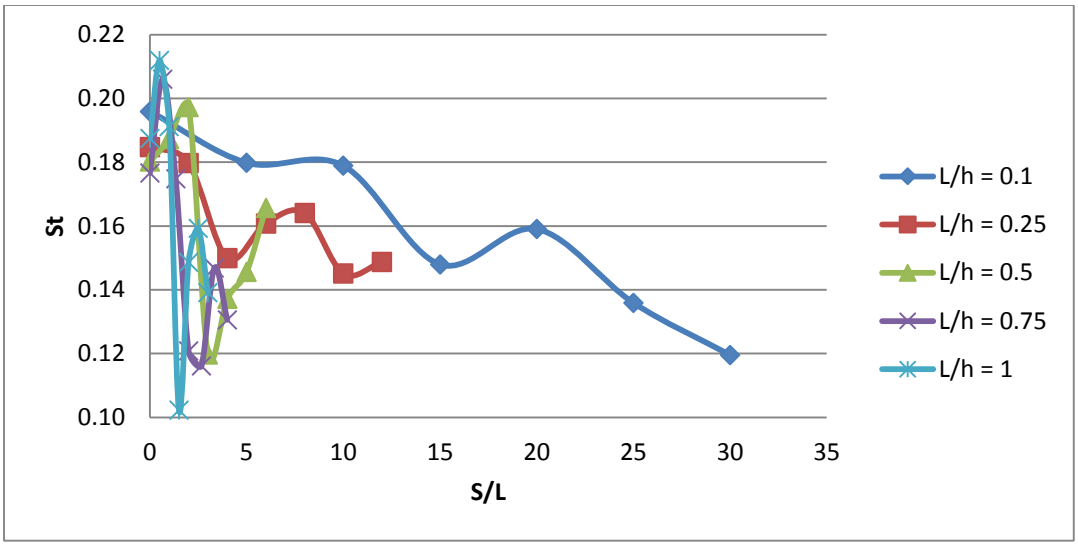

Figure 3.15: Strouhal number at several *S/h* and *L/h*.

Modified Strouhal and Reynolds numbers

Since there was no clear trend for Strouhal number with geometry for all Reynolds number values, it was convenient to use the Buckingham π-theorem to generate a modified Strouhal number and Reynolds number, which can be written as follows:

$$\pi_1 = \frac{\pi_2 \pi_3}{\pi_4} \qquad 3.18$$

The modified Strouhal number (St_M), π_1, is obtained by replacing π_2, π_3 and π_4 in equation 3.18 by Strouhal number (St), S/h and L/h respectively. So the Modified Strouhal number equals

$$St_M == St\ \frac{S}{L} \qquad 3.19$$

Also the modified Reynolds number (Re_M), or π_1, can be stablished by replacing π_2, π_3 and π_4 in equation 3.18 by Reynolds number (Re), S/h and L/h, respectively. So Modified Reynolds number equals

$$Re_M == Re\ \frac{S}{L} \qquad 3.20$$

Physically, the distances S and L have a strong impact on the vortex dynamics in that flow configuration since they control the vorticity strength developed around the blocks. The spacing S controls the growth of the shear layer (hence vorticity) between the two blocks and the thickness of the 2nd block controls the boundary layer development (hence

vorticity) on the block side, St_M and Re_M are calculated for several *S/h* and *L/h* and their values are listed in Table 3.6 and Table 3.7 respectively.

Table 3.6: Modified Strouhal number at several *S/h* and *L/h*.

S/h	***L/h***				
	0.1	**0.25**	**0.5**	**0.75**	**1**
0	0	0	0	0	0
0.5	0.899	0.360	0.187	0.137	0.106
1	1.789	0.600	0.395	0.233	0.191
1.5	2.219	0.965	0.359	0.242	0.153
2	3.181	1.313	0.549	0.310	0.297
2.5	3.397	1.451	0.728	0.490	0.398
3	3.586	1.785	0.994	0.522	0.417

Table 3.7: Modified Reynolds number at several *S/h* and *L/h*.

S/h	***L/h***				
	0.1	**0.25**	**0.5**	**0.75**	**1**
0	0	0	0	0	0
0.5	35517	14207	7103	4736	3552
1	71034	28414	14207	9471	7103
1.5	106551	42621	21310	14207	10655
2	142069	56827	28414	18942	14207
2.5	177586	71034	35517	23678	17759
3	213103	85241	42621	28414	21310

Figure 3.16 shows that there is a linear relation between St_M and Re_M at several *L/h*, moreover all curves have the same trend for several *L/h* and can be written as:

$$St_M = A\, Re_M + C \qquad 33.21$$

Where: A and C are constants that change with L/h as given in Figure 3.16, Note that the values of A and C are relatively small compared with Strouhal number. The R-Squared value changes from *0.94* to *0.99* implying that the maximum error of equation 3**3**.**21** is in the order of *6%*. Hence *St* number can be obtained for several *Re* numbers, inter spacing between cubes and thickness of second cube by using equation 3**3**.**21**.

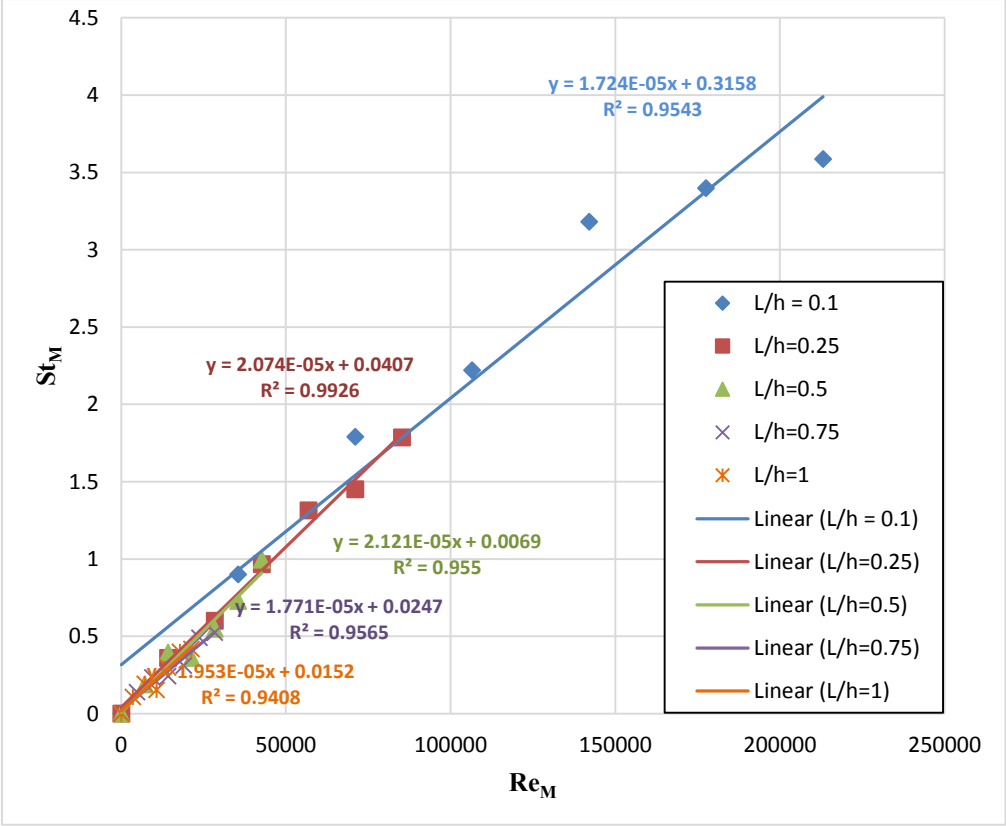

Figure 3.16: Modified Strouhal number versus Modified Reynolds number at several *L/h*.

Figure 3.17 shows that the modified Strouhal number has the same behavior with modified Reynolds number at several *Re* and same spacing. It also shows that for a linear fitting, equation 3.21 is obtained with an R-Squared value of *0.99*.

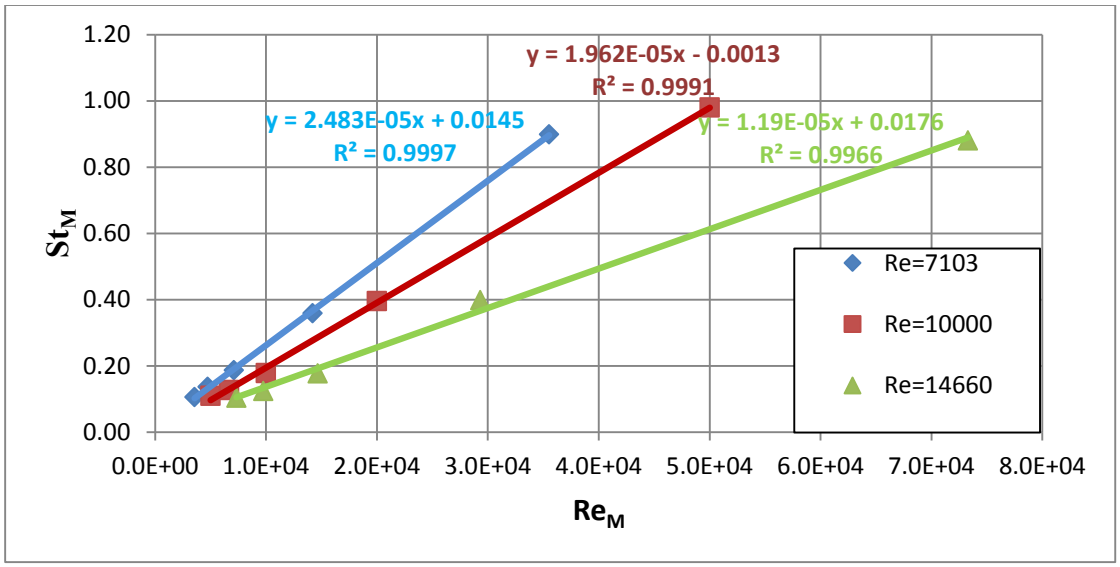

Figure 3.17: Modified Strouhal number vs. Modified Reynolds number at *S/h=0.5* and several *Re*.

Figure 3.18 is probably the most notable of this series of figures as it shows that the data obtained for the modified Strouhal number for all cases of *Re*, *S/h* and *L/h*, when plotted versus the modified Reynolds number, can be fitted with one straight line with a *3%* error (The data can also be fitted with a cubic curve with *1%* error).

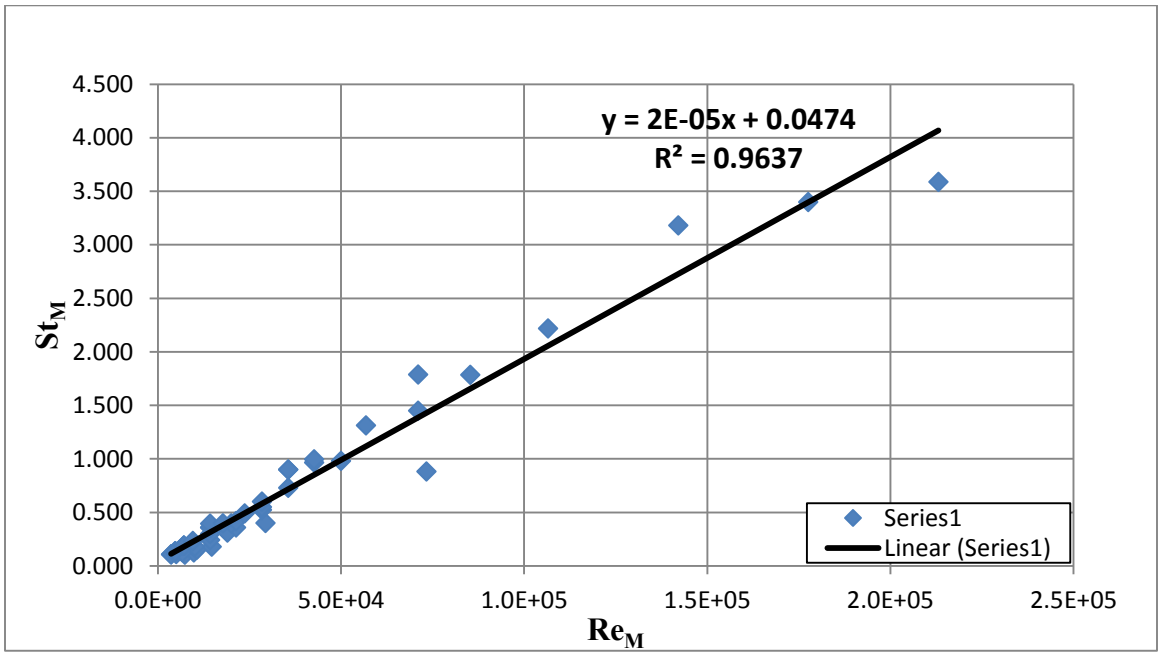

Figure 3.18: Modified Strouhal number vs. Modified Reynolds number.

3.4 Drag calculation on the cubes

As mentioned in Chapter 1, the proposed sensor is intended to measure pressure, among other things. To that end, it will measure the deflection on the sensitive element and use it to infer the drag based on material property of the latter. The numerical flow simulations will then provide the Reynolds number and the pressure corresponding to that drag.

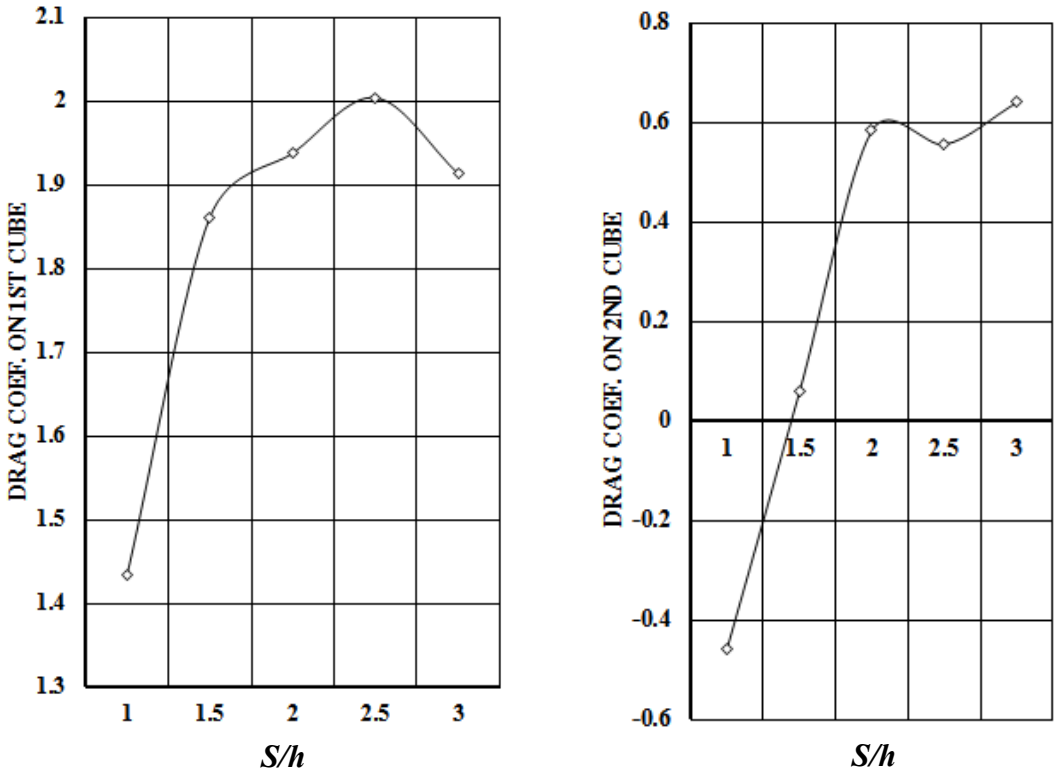

(a) For blocking element. (b) For sensitive element.

Figure 3.19: Drag coefficient on blocking element (left) and sensitive element (right) at *Re=7103* and *L/h=1* (*2D* flow).

The drag on the blocking element is positive, and negative on the sensitive element at low inter-cube spacing values. This qualitative trend was observed experimentally for *2D* flow by other researchers [37, 39]. (Note that the experiment was run at *Re=22,000*.) However the experimentally observed jump in C_d (from *-0.6* to *0.7*) occurring for the sensitive element at *S/h=2*, corresponds to a rapid change of C_d (from *-0.45* to *0.65*) that is spread between *S/h=0.5* and *1.5* in the present numerical flow simulations. This jump is physically due to the switch from an intermittent vortex shedding present for small inter-block spacing

S/h<1 where the flow is weak, to a stable vortex shedding for larger spacing *S/h>2* where vortex shedding starts taking place in the inter-cube spacing. This difference is probably due to the fact that the experimental work was carried out at *Re=22,000* while the simulations were carried out at *Re=7103*, as Re has a strong effect on the flow and vortex shedding in the inter-cube cavity, the shear layers reattachment and turbulence.

3.5 Concluding remarks

This chapter presents the numerical simulation of the two-dimensional incompressible flow over two cubes in tandem. After verifying the numerical flow pattern versus the experimental one documented in the previous chapters, the flow was simulated for various configurations and the flow physics was interpreted accordingly.

In summary, the following remarks are due:

- The flow is characterized by vortex shedding, splitting, merging and finally diffusing as it convects downstream
- For *S/h≤1*, the flow in the inter-cube cavity has little influence elsewhere but the vortex shedding is intermittent
- The crossflow velocity, *w*, is strongest around *x=0.5h* to *x=h* downstream of the second cube (near wake) and Strouhal number is stable along the centerline *z=0* at distances *x/h>6*. This fact suggests that a good place to measure the local vortex shedding frequency would be at a location where *z=0* and *x/h≥6*.
- The distances *S* and *L* have a strong impact on the vortex dynamics in that flow since they control the vorticity flux generated on the cube sides and on the inter-cube walls as well as the vortex generation in the inter-cube region.
- The parametric study suggests a 'general' linear correlation between St_M and Re_M that is valid for all values of Re (*7103* to *14660*), *S/h* (*0* to *3*) and *L/h* (*0.1* to *1*) investigated in this work. Namely,

  $$St_M = 2 \times 10^{-5} Re_M - 0.0474,$$

  with a maximum approximation error of *3.6%*. This correlation gives the flexibility of computing the vortex shedding frequency for a wide range of actual flow conditions and geometric configurations.
- The *2D* flow simulation gives a good agreement with the experimental work.

Chapter 4

TWO- AND THREE-DIMENSIONAL COMPRESSIBLE FLOW SIMULATION USING DNS

In this chapter, the air flow over two cubes in tandem is computed by Direct Numerical Simulation (*DNS*) using *ANSYS-CFX*. The approach taken in implementing the *2D* water flow simulation presented in the previous chapter is applied to *2D* and *3D* air flow over two cubes in the compressible flow regime. The resulting flow patterns for *2D* and *3D* air flow are verified against available experimental data and against basic flow physics. The results are presented and discussed for several Reynolds and Mach numbers, in particular the effect of compressibility.

Air flow around two cubes in a tandem arrangement is simulated using *DNS*. The flow is governed by the Navier-Stokes equations, as well as continuity and energy equations that are solved with proper boundary and initial conditions. The air is assumed to be an ideal gas with constant specific heats. Table 4.1 shows the Reynolds and Mach numbers for the nine several cases that were examined. Note that all inlet Mach numbers are subsonic however there are regions of supersonic flow within the flow domain.

Table 4.1: Reynolds number and Mach number for *3D* cases.

Reynolds number (Re_∞)	Mach number (M_∞)		
500	0.25	0.5	0.75
1000	0.25	0.5	0.75
2000	0.25	0.5	0.75

4.1 Flow governing equations

The governing equations for a Newtonian fluid with no body forces are written as [26]:

Continuity equation

$$\frac{\partial \rho}{\partial t} + \vec{\nabla} . (\rho \vec{U}) = 0 \qquad 4.1$$

Momentum equations

$$\frac{\partial (\rho \vec{U})}{\partial t} + \vec{\nabla} \cdot (\rho \vec{U} \otimes \vec{U}) = -\vec{\nabla} p + \vec{\nabla} \cdot \bar{\bar{\tau}} \qquad 4.2$$

Where the stress tensor, $\bar{\bar{\tau}}$, is given by

$$\bar{\bar{\tau}} = \mu \left(\vec{\nabla} \vec{U} + (\vec{\nabla} \vec{U})^T - \frac{2}{3} \delta \vec{\nabla} \cdot \vec{U} \right) \qquad 4.3$$

Total energy equation

$$\frac{\partial (\rho h_{tot})}{\partial t} - \frac{\partial p}{\partial t} + \vec{\nabla} \cdot (\rho \vec{U} h_{tot}) = \vec{\nabla} \cdot (k_{th} \vec{\nabla} T) + \vec{\nabla} \cdot (\vec{U} \cdot \bar{\bar{\tau}}) \qquad 4.4$$

Where h_{tot} is the total enthalpy, related to the static enthalpy *h(T,P)* by:

$$h_{tot} = h + \frac{1}{2} U^2 \qquad 4.5$$

The term $\vec{\nabla} \cdot (\vec{U} \cdot \bar{\bar{\tau}})$ is the viscous dissipation term which represents the work due to viscous stresses.

4.2 Numerical implementation

The flow governing equations are discretized in space using a second order accurate finite volume approach, in which the control volume is node-centered, and the finite element approach is used to integrate the equations in space, which are linearized and are solved using an iterative approach. The problem is considered converged when the *RMS* (root mean square) of the residuals is less than 10^{-8}. For unsteady flow simulation, the equations are then integrated in time using a second order backward Euler scheme (also known as Gear scheme), which is an implicit scheme in time. More details are given in the *CFX-solver* theory documentation [26].

4.2.1 Computational domain

2D Computational domain

- The computational domain that is used for all *2D* compressible cases is given in Figure 3.1 which is the same computational domain used in *2D* incompressible flow except for the domain sides being set as 'open boundary' instead of 'wall' so as to match the *3D* compressible flow case. Note that h is kept at *40 μm* and *S=h* is also unchanged for all cases tested.

3D Computational domain

A sketch of the computational domain that is used for all the *3D* cases is given in Figure 4.1; it shows the layout of the two cubes and some key dimensions where:

- *h* is the cube side and is equal *40 μm* for all cases.
- *S* is the separation distance between the two cubes; *S=h* for all cases.

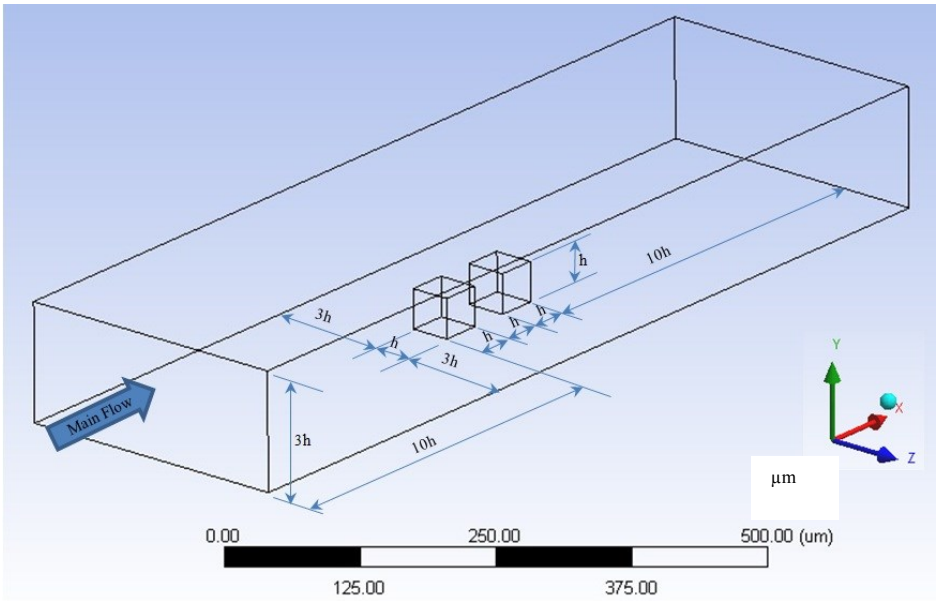

Figure 4.1: The computational domain.

The computational domain measures *23h* in the streamwise direction, *x*; *3h* in the vertical direction, *y*; and *7h* in the span-wise direction, *z*. The origin of the computational domain is taken at the middle of the leading edge of the blocking element (*BE*), i.e. the upstream cube. The cubes are located in the range $0 \leq x \leq h$ and $2h \leq x \leq 3h$, respectively.

4.2.2 Mesh resolution

In any numerical flow computation, the mesh should be fine enough to resolve the flow features associated with the postulated assumptions, e.g. potential flow, inviscid flow, laminar flow, or turbulent flow, where turbulence is modeled with for instance, with an algebraic or n-equations model. In this work, the flow equations are simulated directly using *DNS* computation, which implies that all flow features at all length scales need to be resolved by the mesh. These considerations increase the computation time. To capture the smallest flow features the mesh should be as fine as the Kolmogorov length scale, (η). Moreover, (η) is rather sensitive to Re as it is roughly proportional to $Re^{-9/4}$. Hence the mesh size depends rather strongly on Reynolds number and the mesh quality depends on aspect ratio and skewness. Knudsen number, *Kn*, for air is calculated to ensure that the continuum assumption holds. Before describing the mesh size and discretization, the Kolmogorov length scale and Knudsen number are estimated.

Kolmogorov length scale (η_{air})

The Kolmogorov length scale was calculated in Sec. 3.2.2 for water, which is essentially an incompressible fluid. In this section, it will be calculated for air which is assumed to be an ideal gas with constant C_p and C_v.

The difference between the computation procedures followed to compute η_{air} as opposed to η_w results from the fact that we need to compute the primitive variables starting from the Reynolds and Mach numbers given in Table 4.1. These details are given in Appendix D. Moreover, the size of the maximum eddy is set *to* $H=h=40\times10^{-6}$ *m* in all cases. Table 4.3 gives the Kolmogorov length scale for all cases considered in this chapter and the values of pressure and temperature are given in Table 4.7.

Knudsen number (*Kn*)

The Knudsen number is written as:

$$Kn = \frac{\lambda}{L} \tag{4.6}$$

Where L is the characteristic length scale and λ is the mean free path:

$$\lambda = \nu \sqrt{\frac{\pi}{2\,R\,T}} \tag{4.7}$$

Gatski [51] proposes to express the mean free path by unit Reynolds number, ($Re^* = U_\infty/\nu$), and the Mach number as:

$$\lambda = \sqrt{\frac{\pi\,\gamma}{2}}\left(\frac{M}{Re^*}\right) \qquad 4.8$$

Concerning the characteristic spatial length, Gatski [51] (page 82) states that: "The length scale L can be, for example, either the physical dimension of an obstacle or the thickness of the boundary layer that develops on the obstacle". In the present case, the more appropriate length scale to use is the cube side h, because the scale is typically set by the device dimension, phenomenon or confinement of flow field. Also Gatski mentioned that the Kolmogorov length scale is taken as the length scale in case of calculation of micro-structure Knudsen number ($Kn_\lambda=\lambda/\eta$). Since the Reynolds and Mach numbers are given in Table 4.1, the Knudsen number and Kolmogorov length scale can be evaluated. Table 4.3 provides their values for several cases. It is clear that the Kolmogorov length scale is a function of Reynolds number only, whereas Knudsen number is a function of both Reynolds and Mach numbers. According to the continuum hypothesis, the continuum assumption is valid when $Kn \leq 0.01$ [see e.g., Gatski [51] (page 82) and Dyson [47] (page 47)]. Table 4.3 shows that *Kn* number computed for all cases is much smaller than *0.01*, therefore the continuum assumption is valid. Another approach is that the *Kn* number be calculated based on the minimum mesh length. From Table 4.3, λ is of order 10^{-8} m and from Table 4.4 to Table 4.6, the minimum mesh length (Δ_{min}) is of order 10^{-6} m. So $Kn \leq 0.01$ therefore while the continuum assumption is valid for the *3D* cases, for the *2D* cases the minimum mesh is three times the mean free path in all cases.

Finally the mean time between collisions (τ_m) should be checked. It must be *100 times* the time step for continuum validation. It is obtained as follows:

First the mean molecular velocity is obtained from [51]

$$C_m = \sqrt{\frac{8\,R\,T}{\pi}}\;(m/s) \qquad 4.9$$

So

$$\tau_m = \frac{\lambda}{C_m}\;(s) \qquad 4.10$$

Table 4.2 shows the typical values of both mean molecular velocity and the mean time between collisions at several Reynolds numbers and Mach numbers. From this table it is clear that the minimum mean time between collisions is in the order of 10^{-10} and the time step is in the order of 10^{-8}. Therefore the time step is 100 times the mean time between collisions. Hence the continuum assumption is valid

Table 4.2: Mean molecular velocity and the mean time between collisions at several Reynolds number and Mach number.

Re	Mach number					
	0.25		0.5		0.75	
	C_m	τ_m	C_m	τ_m	C_m	τ_m
500	539.47	5.51×10^{-11}	809.2	7.33×10^{-11}	539.47	1.65×10^{-10}
1000	539.47	2.74×10^{-11}	809.2	3.67×10^{-11}	539.47	8.25×10^{-11}
2000	539.47	1.38×10^{-11}	809.2	1.83×10^{-11}	539.47	3.71×10^{-11}

Knowing the Kolmogorov length scale and the continuum limit, the mesh size can now be chosen. The mesh resolution is divided into five regions in the *x*-, *y*- and *z*-directions as shown in Table 4.4, Table 4.5 and Table 4.6, where γ denotes the mesh spacing normalized by the Kolmogorov length scale. These tables show that the mesh scales are less than 5.26η near the cubes and increase to about 10η further away from the cubes. The mesh is generated using *ICEM-CFD*, which is a mesh generation package that starts from a *CAD* geometry, and is part of *ANSYS 12.1*. Finally, the skewness and the aspect ratio were checked in *ICEM-CFD* and typical values for the aspect ratio fall in the range between *0.36* and *0.985* while the skewness is equal to *1* since the mesh is rectangular.

Table 4.3: Kolmogorov length scale and Knudsen number at different Reynolds number and Mach number.

Re	Re^*	Mach number								
		0.25			0.5			0.75		
		η (μm)	λ (m)	*Kn*	η (μm)	λ (m)	*Kn*	η (μm)	λ (m)	*Kn*
500	12.5×10^{6}	1.423	2.97×10^{-8}	0.00074	1.432	5.93×10^{-8}	0.00148	1.432	8.9×10^{-8}	0.00223
1000	25×10^{6}	0.846	1.48×10^{-8}	0.00037	0.846	2.97×10^{-8}	0.00074	0.846	4.45×10^{-8}	0.00111
2000	50×10^{6}	0.503	7.42×10^{-9}	0.00019	0.503	1.48×10^{-8}	0.00037	0.503	2×10^{-8}	0.00056

Table 4.4: Mesh discretization in *x*-direction for *3D* cases.

Re	Region	Δx (μm)		γ_x	
		Max.	Min.	Max.	Min.
500	$-10 \le x/h \le 0$	5.2795	2.6478	3.71	1.86
	$0 \le x/h \le 3$	2.10526		1.12	
	$3 \le x/h \le 13$	5.2795	2.6478	3.71	1.86
1000	$-10 \le x/h \le 0$	5.2795	2.6478	6.24	3.13
	$0 \le x/h \le 3$	2.10526		2.49	
	$3 \le x/h \le 13$	5.2795	2.6478	6.24	3.13
2000	$-10 \le x/h \le 0$	5.2795	2.6478	10.5	5.26
	$0 \le x/h \le 3$	2.10526		4.19	
	$3 \le x/h \le 13$	5.2795	2.6478	10.5	5.26

Table 4.5: Mesh discretization in *y*-direction for *3D* cases.

Re	Region	Δy (μm)		γ_y	
		Max.	Min.	Max.	Min.
500	$0 \le y/h \le 1$	2.32062	2	1.63	1.41
	$1 \le y/h \le 3$	3.53769	2.6478	2.49	1.86
1000	$0 \le y/h \le 1$	2.32062	2	2.74	2.36
	$1 \le y/h \le 3$	3.53769	2.6478	4.18	3.13
2000	$0 \le y/h \le 1$	2.32062	2	4.61	3.98
	$1 \le y/h \le 3$	3.53769	2.6478	7.03	5.26

Table 4.6: Mesh discretization in *z*-direction for *3D* cases.

Re	Region	Δz (μm)	γ_z
500	$-3.5 \leq z/h \leq -0.5$	2.6087	1.83
	$-0.5 \leq z/h \leq 0.5$	2.5	1.76
	$0.5 \leq z/h \leq 3.5$	2.6087	1.83
1000	$-3.5 \leq z/h \leq -0.5$	2.6087	3.08
	$-0.5 \leq z/h \leq 0.5$	2.5	2.96
	$0.5 \leq z/h \leq 3.5$	2.6087	3.08
2000	$-3.5 \leq z/h \leq -0.5$	2.6087	5.19
	$-0.5 \leq z/h \leq 0.5$	2.5	4.97
	$0.5 \leq z/h \leq 3.5$	2.6087	5.19

Table 4.7: Boundary values for velocity, pressure and temperature for the different cases of Reynolds and Mach numbers.

Re	Mach number								
	0.25			0.5			0.75		
	U_∞ *(m/s)*	*T (K)*	P_{abs} *(kPa)*	U_∞ *(m/s)*	*T (K)*	P_{abs} *(kPa)*	U_∞ *(m/s)*	*T (K)*	P_{abs} *(kPa)*
500	100	398.21	326.27	300	895.97	418.51	300	398.21	108.76
1000	100	398.21	652.54	300	895.97	837.02	300	398.21	217.51
2000	100	398.21	1305.07	300	895.97	1674.03	300	398.21	435.03

4.2.3 Boundary conditions

Boundary conditions for the *2D* flow cases

The inlet of the computational domain is located at $x=-3h$ where the inlet boundary is subsonic, the velocity is in the x-direction and is uniform as shown in Table 4.7 The computational domain exit is located at $x=20h$, and is set as 'open boundary' (implying that when the flow direction is into the domain, the pressure and temperature values are taken to be the total values based on the velocity component normal to the boundary, and when it is leaving the domain, they are taken to be the relative static pressure and temperature). The pressure and temperature are given according to each case as shown in Table 4.7. The domain exit plane was taken to be far enough so as to minimize the impact of the exit boundary condition on the von Karman vortex street and the vortex shedding frequency. The side boundaries, at $z=\pm 5.5h$, are set as 'open boundary'. The no slip wall boundary condition is set on the cubes surfaces. The boundaries at $y=\pm\ 0.0125h$ are set as symmetry planes.

Boundary conditions for the *3D* flow cases

The inlet of the computational domain is located at $x=-10h$ to ensure that the flow has developed before reaching the first cube. The flow enters the computational domain with a given uniform temperature and velocity parallel to the x-axis.

The computational domain exit is located at $x=13h$, and is set as 'open boundary' where the pressure and temperature are given according to each case, as shown in Table 4.7. The exit is taken far enough to let the von Karman vortex street develop and vortex shedding frequency be measured. The side boundaries at $z=\pm 3.5h$ are set as 'open boundary' where flow can go in or out. The no slip wall boundary condition is set at $y/h=0$ and on the cubes surfaces; the top boundary, located at $y=3h$, is set as 'an open boundary'.

In *CFX-pre* the temperature and pressure are needed to set the opening boundary conditions. Both must satisfy both Reynolds number and Mach number. Given the temperature computed in the previous section, the dynamic viscosity of air is obtained from "Air Properties Tables" [46]. The air density is then calculated using $\rho=\mu/v$, and the pressure is finally estimated from the ideal gas law for each case.

4.2.4 Initial conditions and temporal resolution

The steady state solution obtained on the same mesh and with the same boundary conditions is taken as the initial condition for the time accurate *DNS* computation. The steady state solution is assumed to be converged either when the *RMS* of the normalized residuals drops to 10^{-8} or after *2,000 iterations* whichever happens first.

The total physical time is chosen to be $t_{tot}=10^{-4}$ *s* as it gives a good number of periodic vortex shedding. The time step is given by the Kolmogorov time scale (t_η) and is calculated as follows [25]:

$$t_\eta = \left(\frac{\nu_{air}}{\epsilon}\right)^{1/2} = \frac{\eta^3}{\nu_{air}} \qquad 4.11$$

Given that ν_{air} is a function of temperature and ϵ is a function of Reynolds number, then t_η is case dependent. However its value was found to be of the order of 10^{-8} *s* for all cases considered in this chapter. Accordingly, the time step (Δt) used in all cases was set to 10^{-8} *s* resulting in 10^4 time steps. At each time step, the local problem iteration is set to a maximum of 10 iterations or is stopped when $RMS=10^{-8}$.

As the physical time advances, the flow field is captured and recorded into a file every 10^{-6} *s* resulting in *100* instantaneous flow fields. Moreover, all flow variables located at chosen probing points were captured and recorded at each time step.

4.3 Results and discussion

In the present section the *2D* and *3D* results and the implied physical phenomena will be discussed. The result samples presented will focus on the following:

- The instantaneous flow pattern is analyzed and interpreted
- The frequency content of the flow at several probing points is examined
- The turbulence kinetic energy is calculated from the *DNS* and is discussed
- A parametric study on the effect of geometry, *Re* and Mach numbers, on *St* is carried out and some interesting conclusions are reached

4.3.1 Expected flow phenomena in *2D* and *3D* flow

Before going through the results and discussion several observations on the flow phenomena associated with the flow over two cubes (or elements) in tandem are due.

In two-dimensional flow, the interesting phenomena can be summarized as:

- There is a boundary layer that develops on the cube walls and convects downstream as a shear layer. This layer affects the vortex dynamics rather strongly in the inter-cube region and the downstream region.
- Moreover if the flow is laminar upstream of the cubes, it will be tripped to turbulent flow as the flow negotiates the turn around the block side edges. A similar behavior was observed for *2D* incompressible (water) flow.

In three-dimensional flow, several flow phenomena take place. They are all manifested in the flow features, some of which are:

- The flow conditions at the inlet boundary are steady and uniform implying that the flow assumes a steady and inviscid-like profile upstream, and hence the total/static pressure and temperature are uniform at inlet. Hence the flow is homentropic and homenthalpic at inlet and, following *Crocco's* theorem, it will remain so except in viscous (or unsteady flow) regions. These are present near solid walls and in the wake of the cubes. Accordingly, the vorticity (and total pressure) contour values that are different from the inlet values, (e.g. those showing on the top and side boundaries downstream of the cubes, as shown in Figure 4.2, Figure 4.3 and Figure 4.4), are a sign of numerical boundary error since there is no physical reason for the flow to be rotational in these regions. These errors are manifested only near the top and side boundaries.
- The flow is highly unsteady and turbulent in the wake behind the cubes, whereas it is almost steady and inviscid-like upstream of the blocks and away from the bottom wall boundary layers.
- The horse shoe vortex development along the bottom wall where the vortex tubes generate at the wall due to viscous effects (in the boundary layer) convect downstream with the flow then curve around the cube. They stretch, tilt, and bend downstream of the cubes diverting the streamlines in the boundary layer, and

skewing them onto either side off the cube while shifting the flow from the near wall into a higher vertical location. They are clearly observed in Figure 4.2 for the vorticity contours just ahead of the first cube, and in Figure 4.3 for the total pressure contours in the cubes plan view, where they show as a region of total pressure gain that wraps around the 1st cube and literally forms a horse shoe with its two legs convecting with the flow far downstream.

- Arc-shaped vortex tubes shed downstream of the 2nd cube. Figure 4.2 shows the vortex core region corresponding to a swirling strength of *0.05* at *Re=500* and $t/t_{tot}=1\ s$ for several Mach numbers. Arc-shaped vortex tubes are periodically shed from the 2nd cube and convect downstream. Three of these arc-shaped vortices can be seen in Figure 4.2b-c. (They do not show in Figure 4.2a, because of the chosen contour levels.) This arc is formed from three merging vortices: two shed from the cube sides and one shed from the cube top. Given that vortex lines are material lines, the arc-shaped vortex lines tilt downstream as they are convected downstream due to the boundary layer velocity profile near the wall. Moreover, this arc is more inclined forward for higher Mach number values. In Figure 4.3 and Figure 4.4, which show the total pressure contours, the two arc sides and the top side are observed as a total pressure increase in the horse shoe vortex where the velocity intensifies. In fact, one can identify the traces of the three arc-shaped vortices in the wake of the 2nd cube, see Figure 4.2.
- Figure 4.4 shows the total pressure deficit associated with the boundary layer developing upstream of the first cube. It develops like a flat plate boundary layer from the domain inlet at *x=-10h* to the leading edge of the first cube, thickening till it reaches its maximum at the cube leading edge, see Appendix B.2. The boundary layer thickness is inversely related with Reynolds number; decreasing from *δ/h=0.71* to *0.5* to *0.35* as *Re* increases from *500* to *1000* to *2000*. The boundary layer is tripped to turbulent flow as separation occurs around the cube top- and side-edges; the turbulence kinetic energy contours are depicted in Figure 4.5 and Figure 4.6.

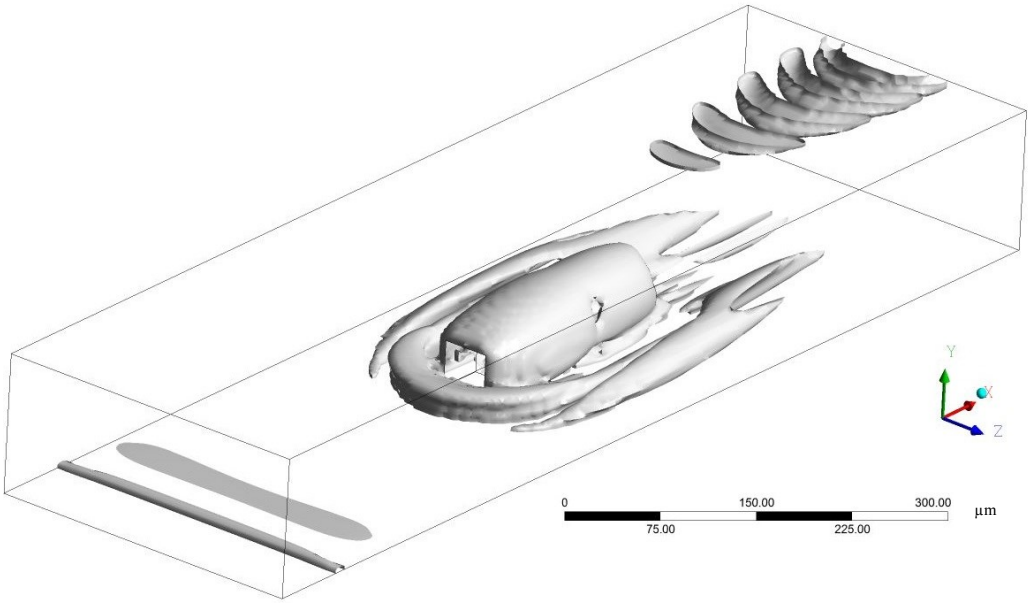

(a) M=0.25

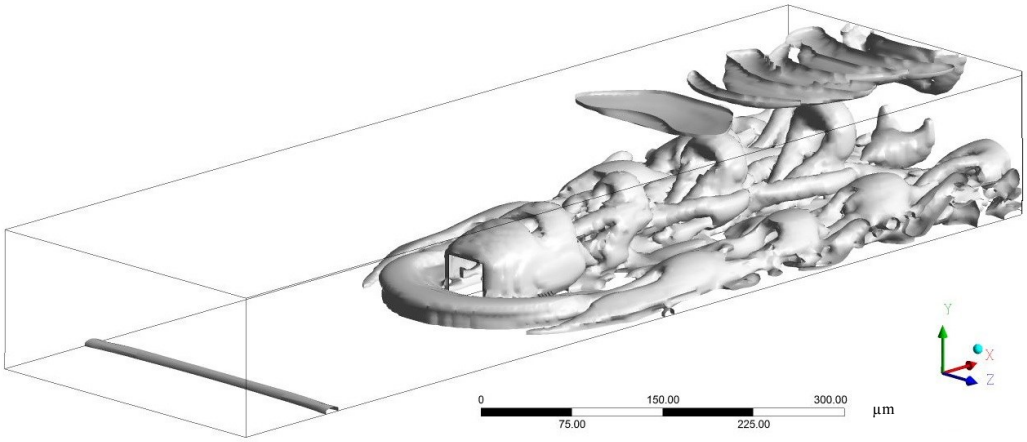

(b) M=0.5

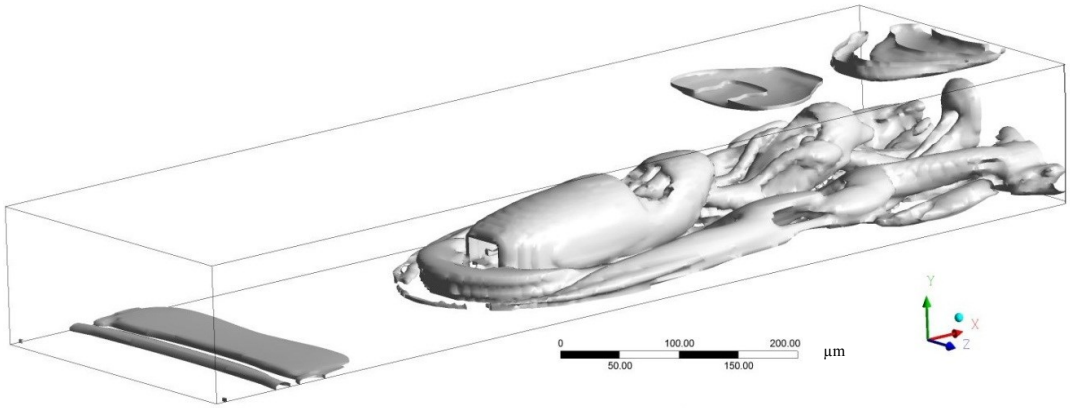

(c) *M=0.75*

Figure 4.2: Vortex core region for swirling strength *0.05*, *Re=500* and $t/t_{tot}=1$.

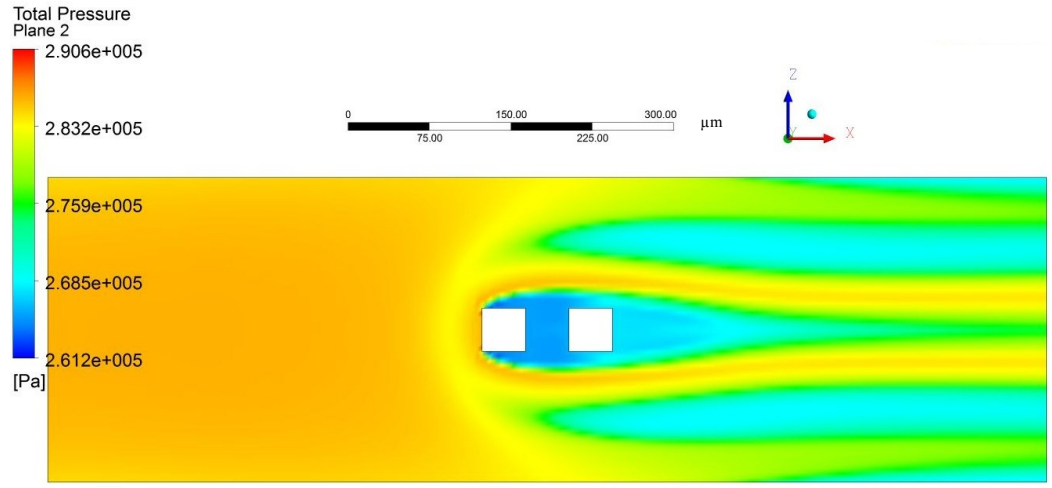

(a) M=0.25

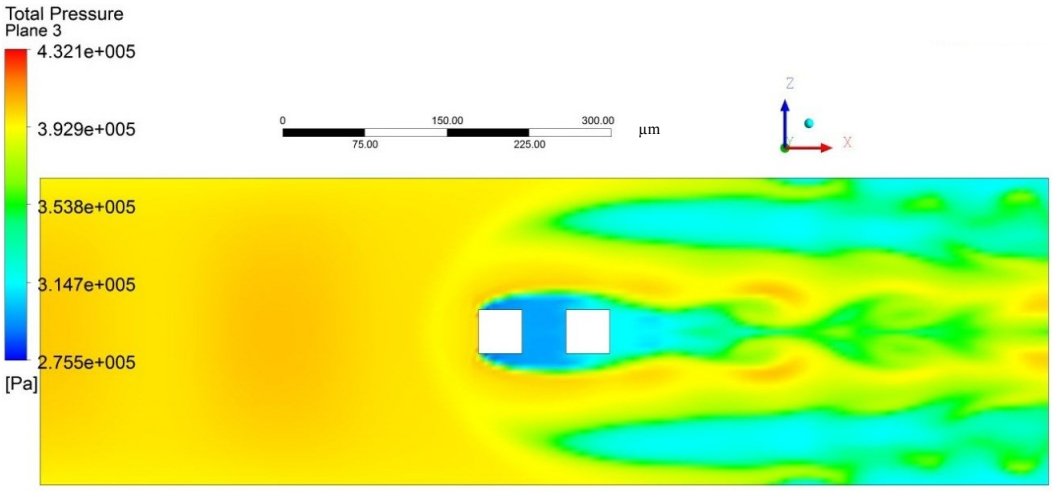

(b) M=0.5

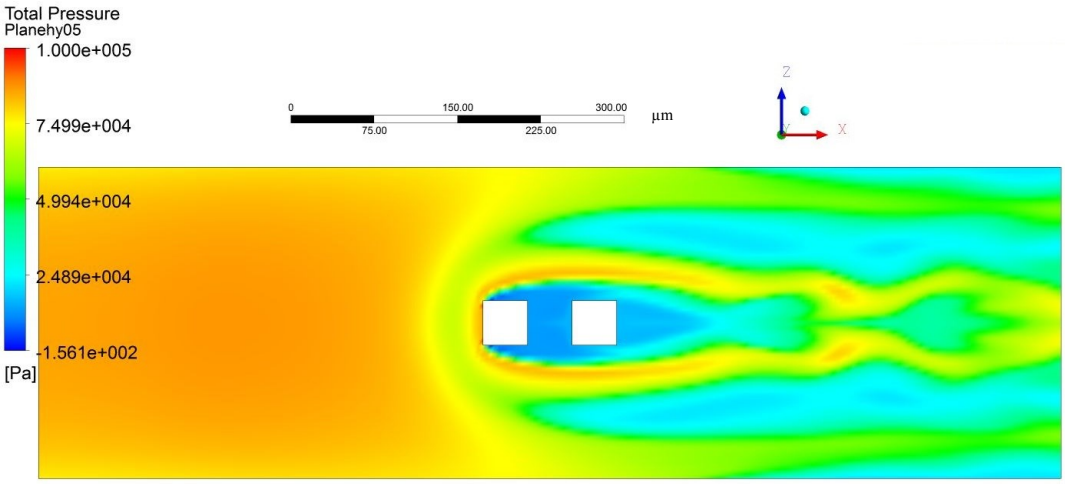

(c) *M=0.75*

Figure 4.3: Total pressure contours on *xz*-plane (*y/h=0.5*) at *Re=500* and $t/t_{tot}=1$.

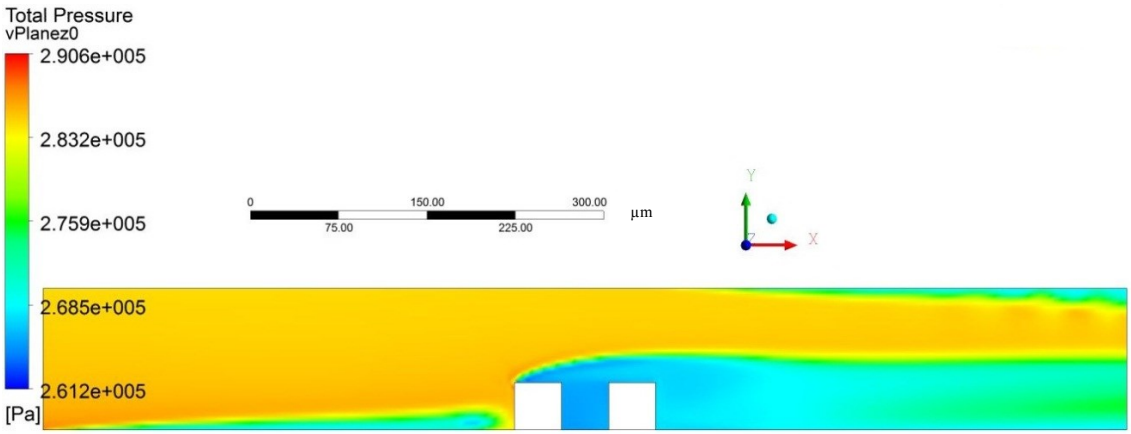

(a) M=0.25

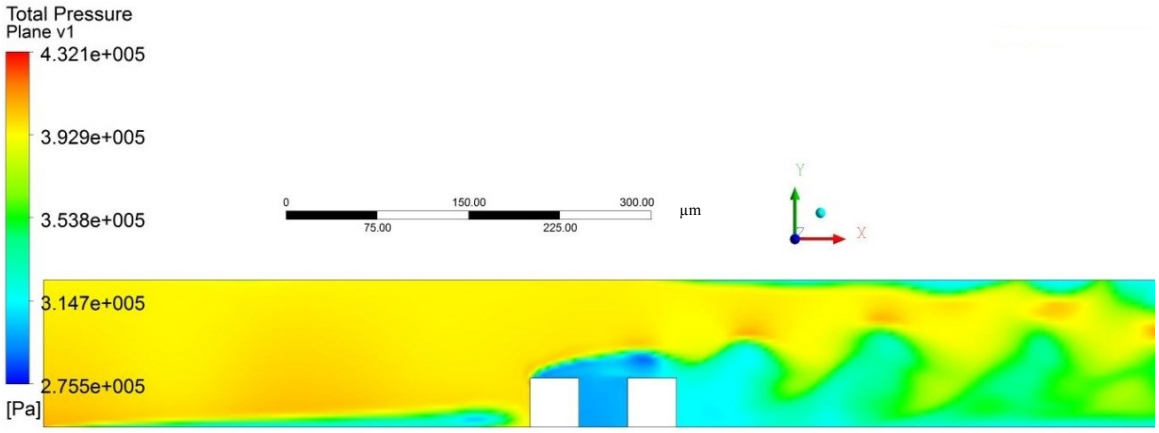

(b) M=0.5

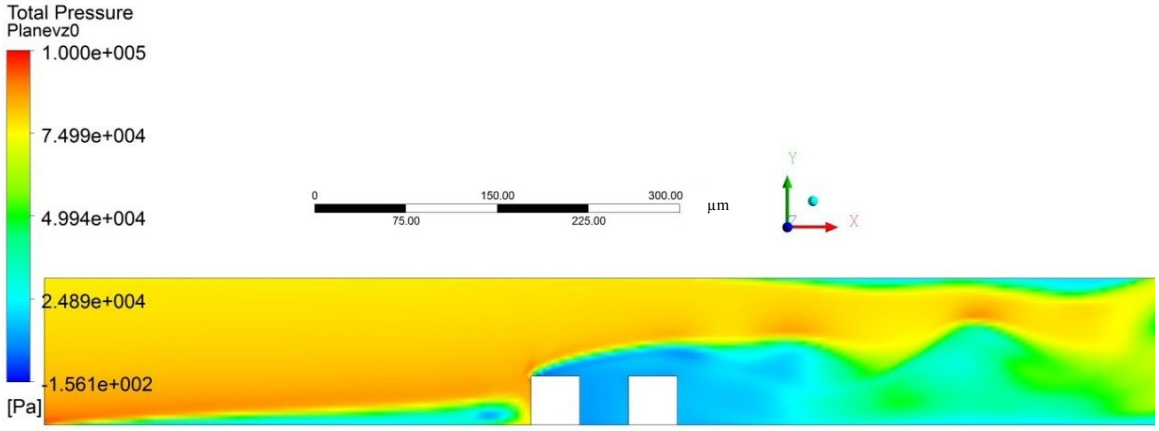

(c) *M=0.75*

Figure 4.4: Total pressure contours on the symmetry plane (*z/h=0*) at *Re=500* and t/t_{tot} =1.

- Figure 4.5 and Figure 4.6 show contour plots of the turbulent kinetic energy in the *xy*-plane and *xz*-plane at *Re=2000*. These figures clearly indicate the effect of compressibility on the redistribution of the turbulent kinetic energy in the inter-cube gap and in the near wake behind the 2nd (or downstream) cube. In fact, turbulence in the gap between the cubes is significantly increased as Mach number increases; this increase will have a significant impact on the force exerted on both cubes and hence the drag coefficients, which are presented later in this chapter.

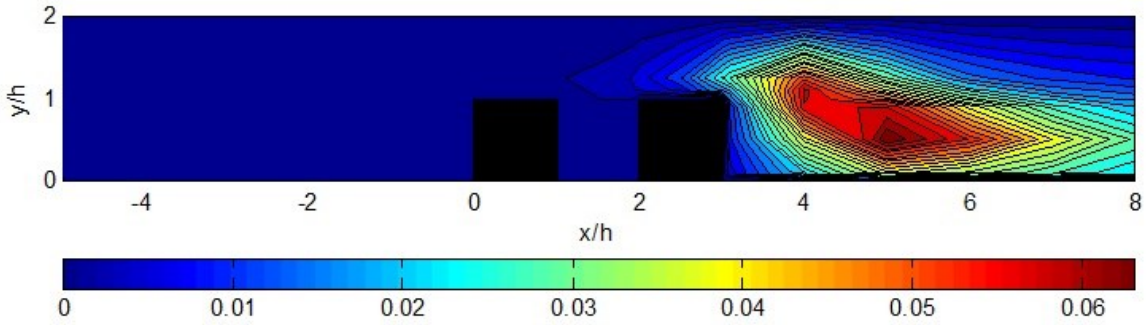

(a) M=0.25

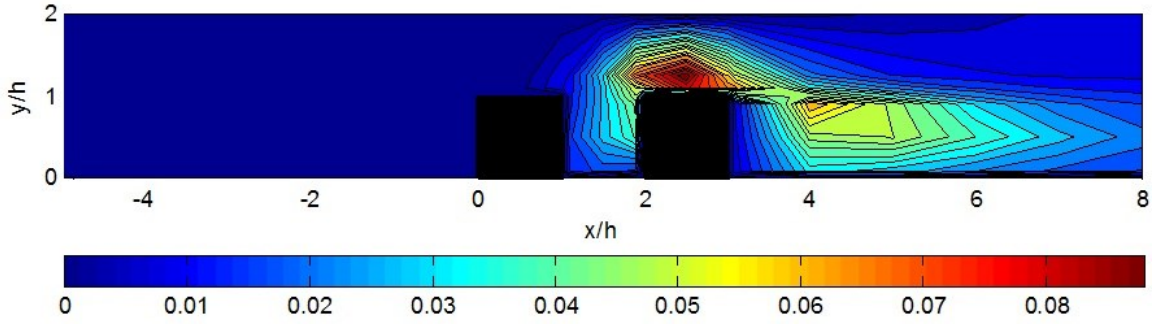

(b) M=0.5

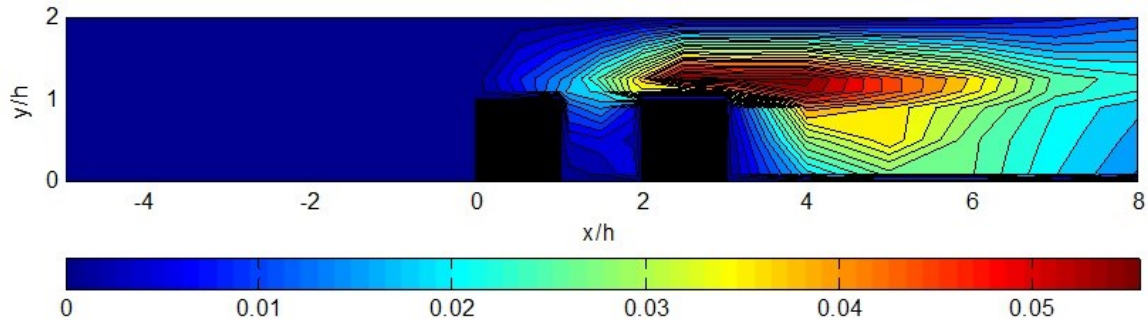

(c) *M=0.75*

Figure 4.5: Contour plots of turbulent kinetic energy K/U_m^2 in the *xy* plane (*z/h=0*) at *Re=2000*.

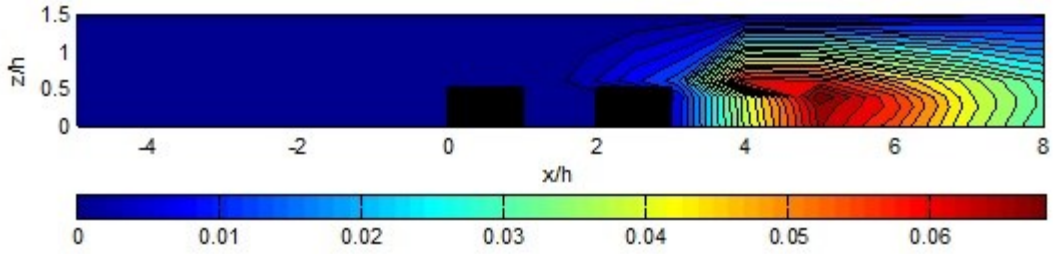

(a) M=0.25

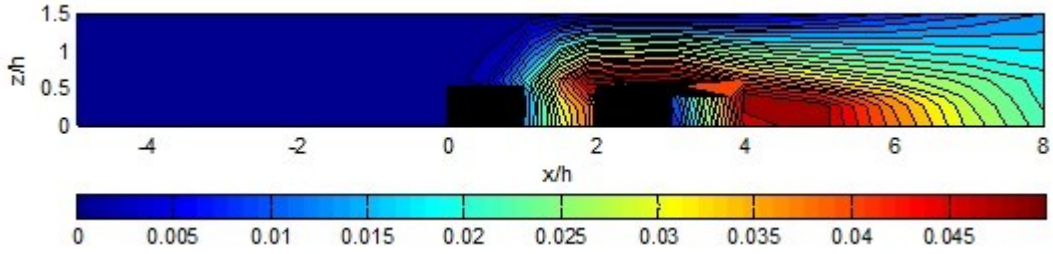

(b) M=0.5

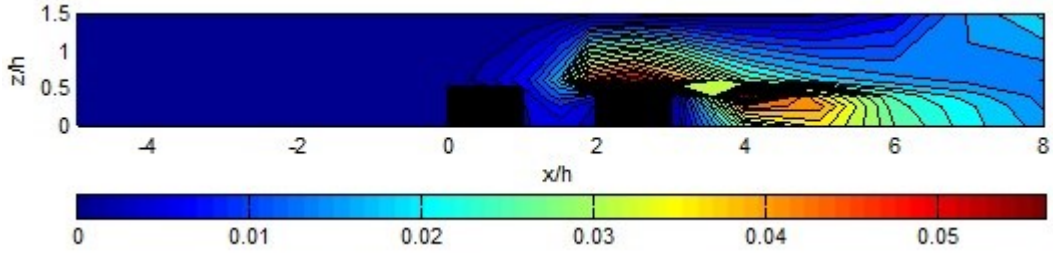

(c) *M=0.75*

Figure 4.6: Contour plots of turbulent kinetic energy K/U_m^2 in the *xz* plane (*y/h=0.5*) at *Re=2000*.

4.3.2 2D results and discussion

The effect of Reynolds and Mach numbers on Strouhal number, observed at a point located at *x/h=5* (measured from the cube leading edge) and *z/h=0* (symmetry line), is shown in Figure 4.7. It shows that Strouhal number is a weak function of Mach number for *Re=500* and *Re=1000*. It also shows that Strouhal number is a weak function of Reynolds number for *M=0.25* and *M=0.5* at $Re \geq 1000$. However Strouhal number experiences a noticeable variation for *Re=2000* when *M=0.75*, therefore the Reynolds and Mach number effects on the Strouhal number have to be accounted for in the study of high Mach and Reynolds numbers flows.

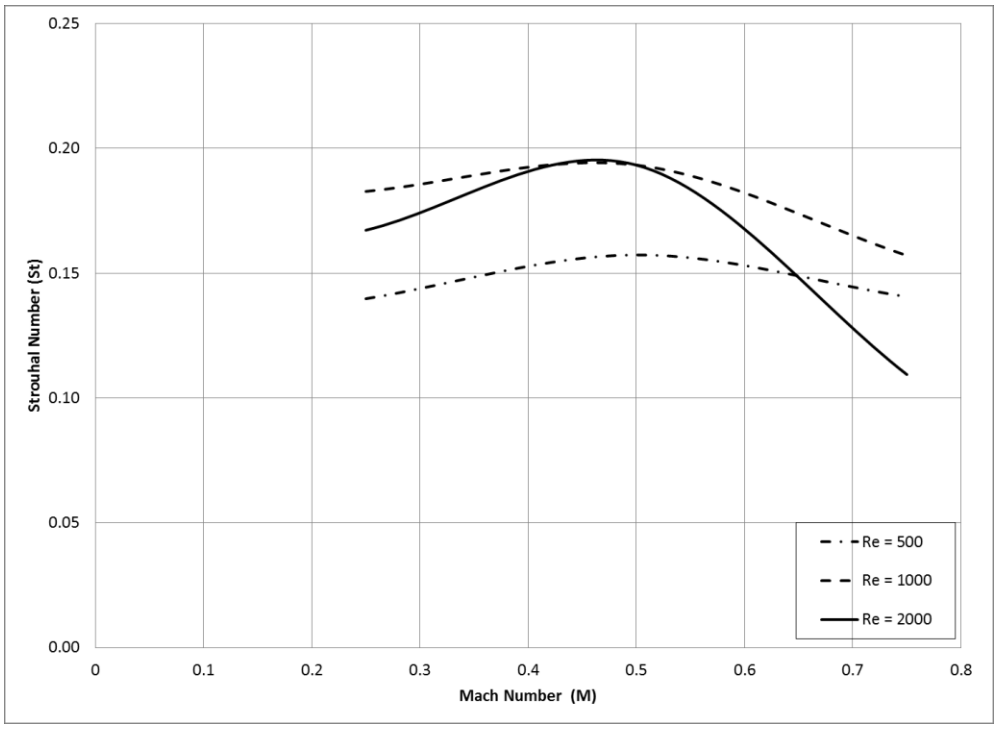

(a) Strouhal number Vs. Mach number

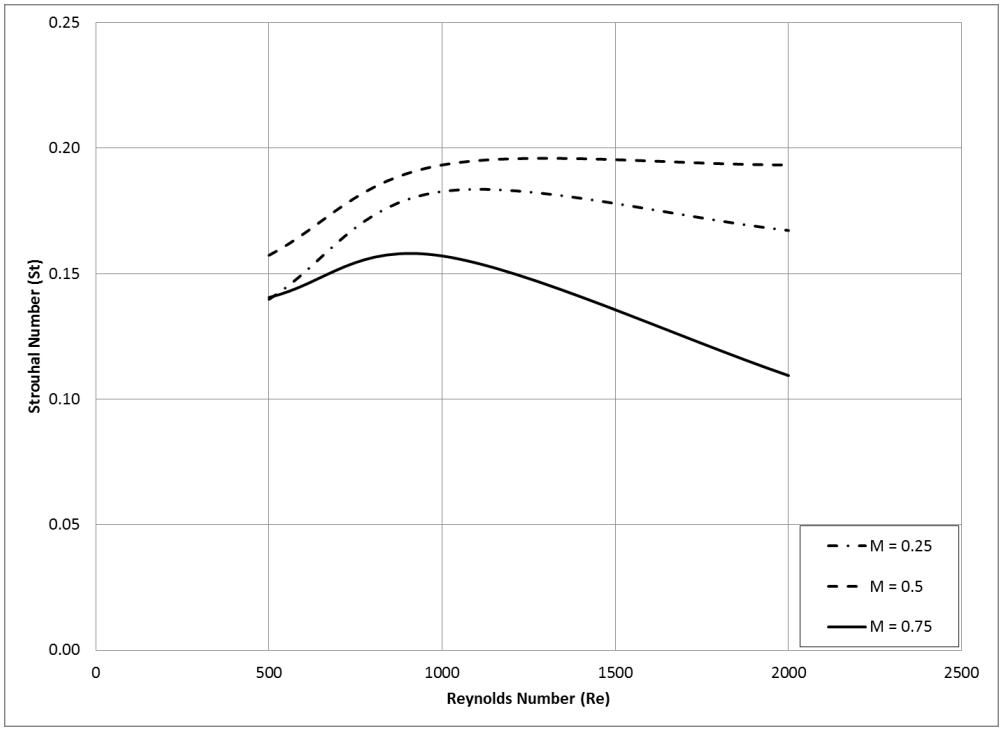

(b) Strouhal number Vs. Reynolds number

Figure 4.7: Average Strouhal number vs. Reynolds on the symmetry plane (*z/h=0*) for *2D* simulations.

Roshko number (*Ro*)

Figure 4.7 and the related discussion given above, suggest that Strouhal number may not be the most appropriate measure of vortex shedding. In fact, Roshko number which combines both *St* and *Re* (see equation 4.12) seems to be more appropriate. It describes oscillating flow mechanisms involving relatively strong viscous effects and is defined as:

$$Ro = \frac{f\,h^2}{\nu} = St\,Re \qquad 4.12$$

Figure 4.8 shows that, for several Mach numbers, Roshko number increases linearly with increasing Reynolds number.

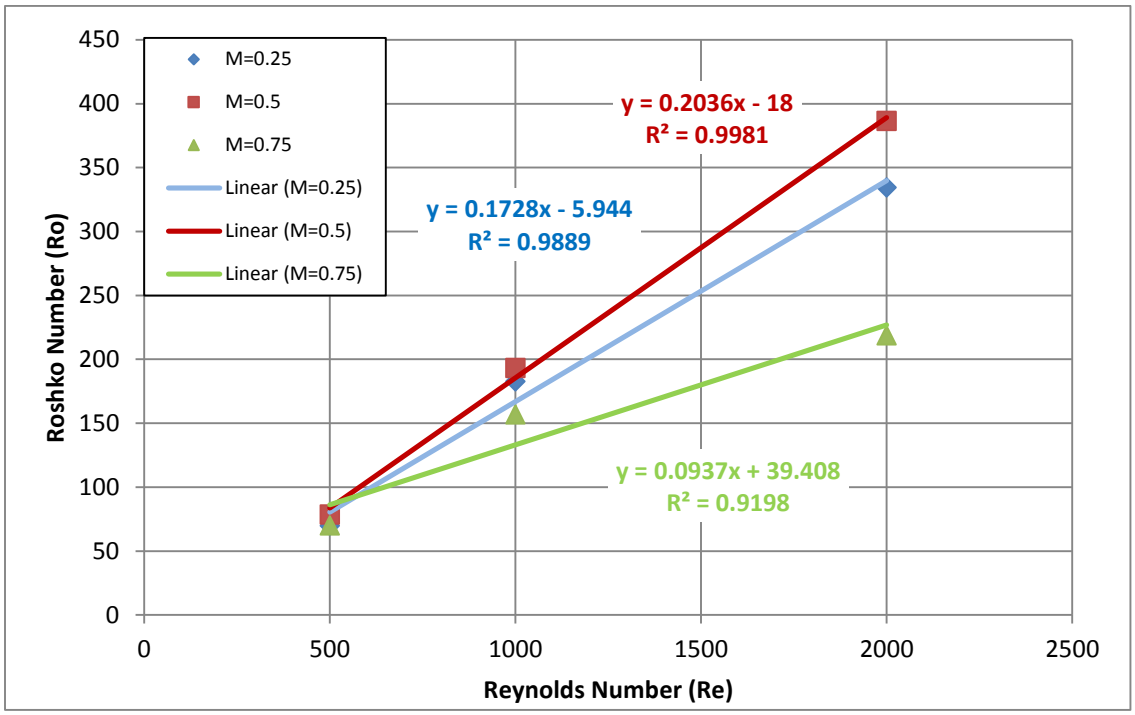

Figure 4.8: Roshko number versus Reynolds number at several Mach number (*2D* flow).

Figure 4.9 shows that for all Reynolds numbers, the variation of Roshko number with Mach number is nonlinear: Roshko number has a maximum value at *M=0.5*. This is probably associated with the impact of compressibility on the turbulent kinetic energy discussed in this section.

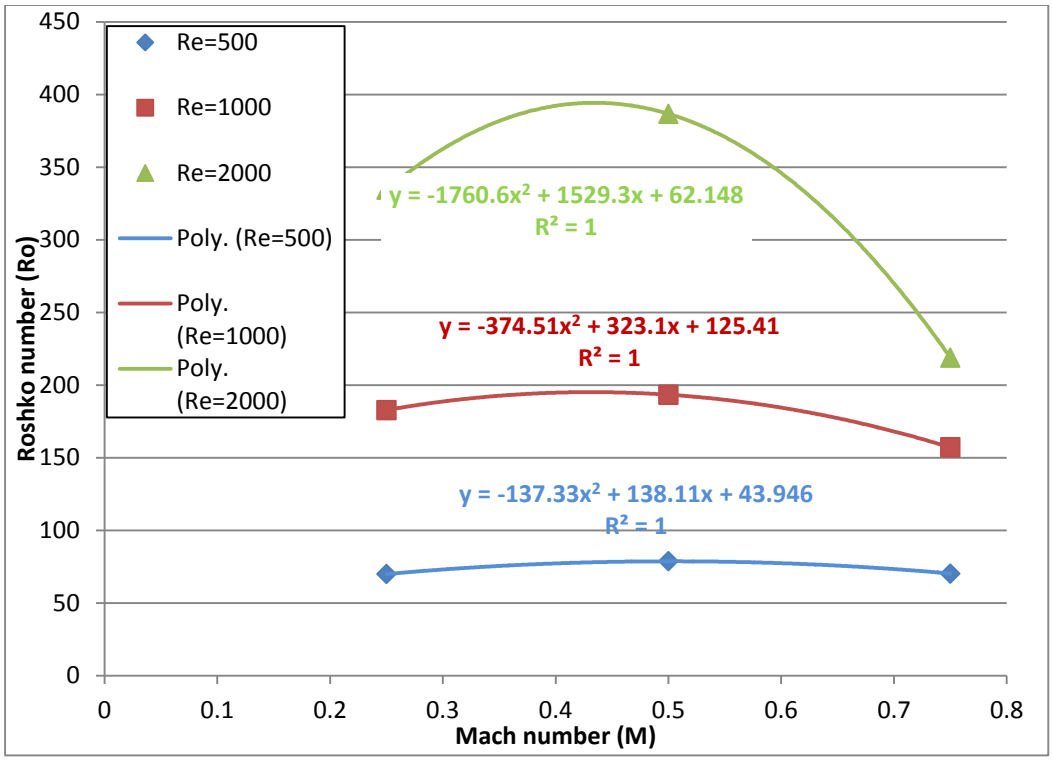

Figure 4.9: Roshko number versus Mach number at several Reynolds number.

4.3.3 3D results and discussion

to begin with, a general comment is due concerning the difference between *2D* and *3D* flow features. Since the flow features over the cubes configuration are strongly influenced by the presence of vortices, it follows that stretching and tilting of the vortex lines will add another level of difficulty in interpreting the *3D* flow behavior.

Figure 4.10, Figure 4.11 and Figure 4.12 show the time trace of the crossflow velocity, w, at a probing point located on the symmetry plane ($z=0$) at $x=5h$ downstream of the second cube and $y=h/2$ above the wall. This point is taken as an example to show the temporal flow variations. Note that probing points at several spatial locations record local flow behavior. The results shown in those figures indicate that the crossflow velocity, hence the vortex shedding, is intermittent at *Re=500* (for all Mach numbers) and at *Re=1000* when *M=0.75*. A *DFT* is used to analyze the signal and identify the dominant flow frequency (if any) at each probing point. As shown in the previous chapter, the Strouhal number is calculated at the dominant Fourier component.

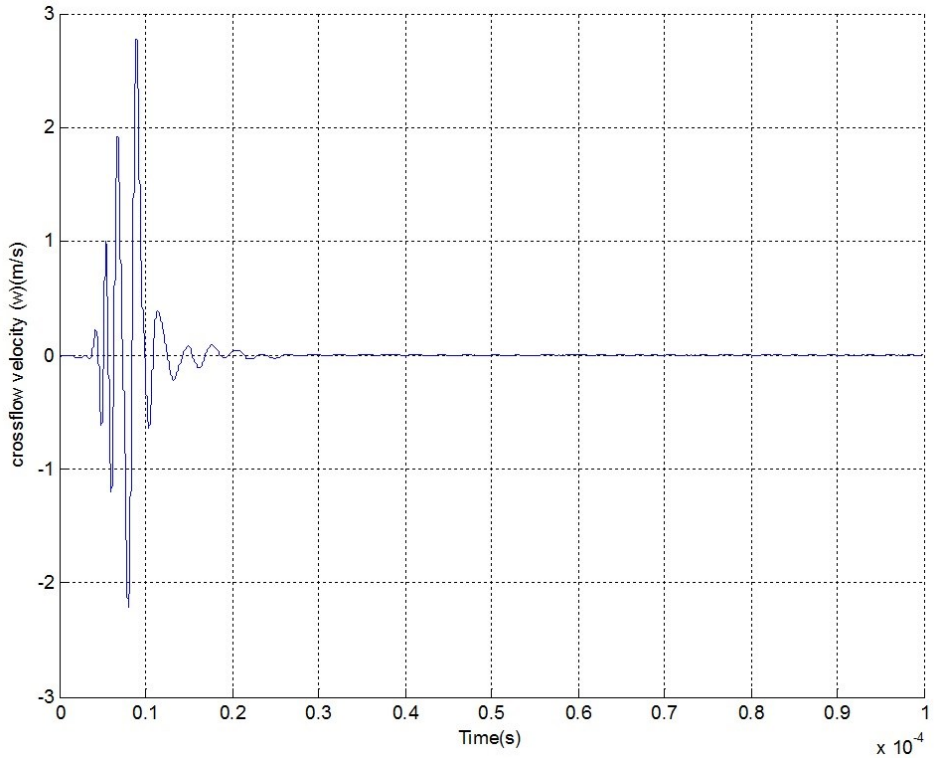
crossflow velocity (w)(m/s)
Time(s)
x 10^-4

(a) M=0.25

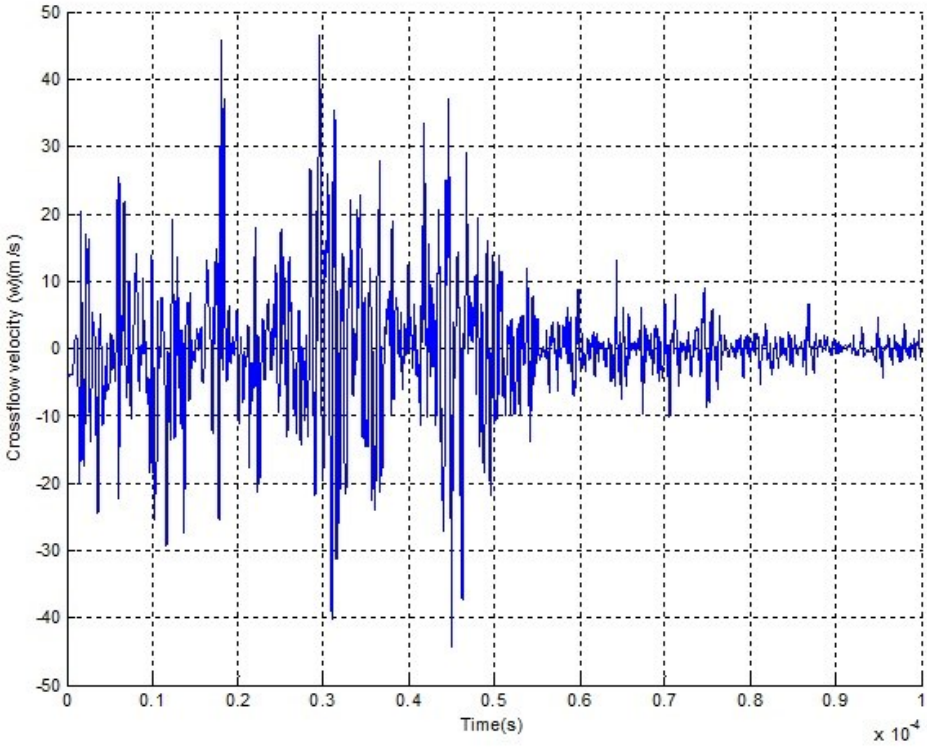
Crossflow velocity (w)(m/s)
Time(s)
x 10^-4

(b) M=0.5

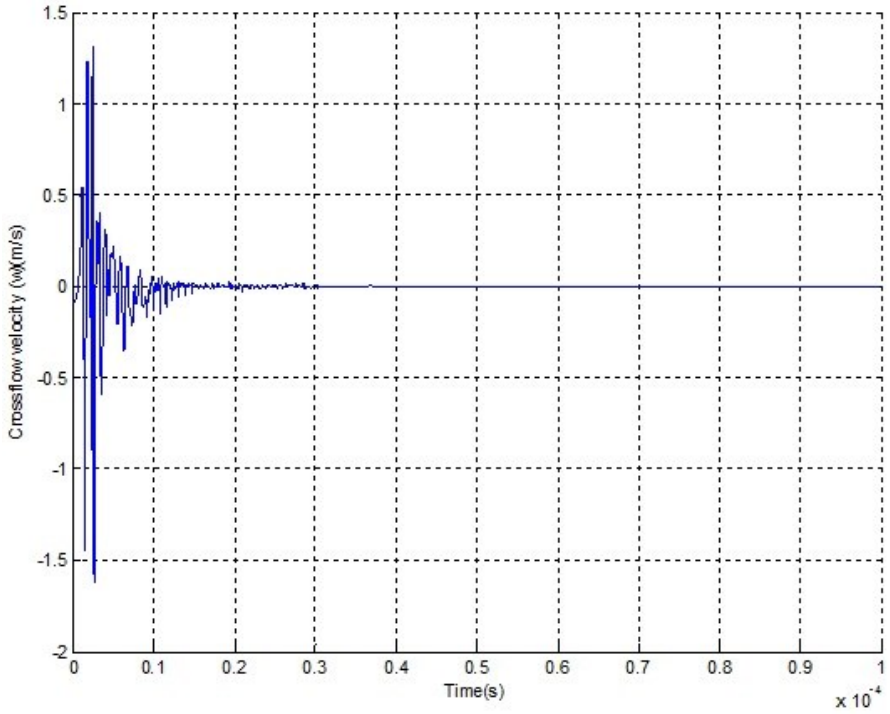

(c) *M=0.75*

Figure 4.10: Time trace of the crossflow velocity (*w*) on the symmetry plane (*z/h=0*) at *y=h/2* and at *x=5h* downstream of the second cube at *Re=500*.

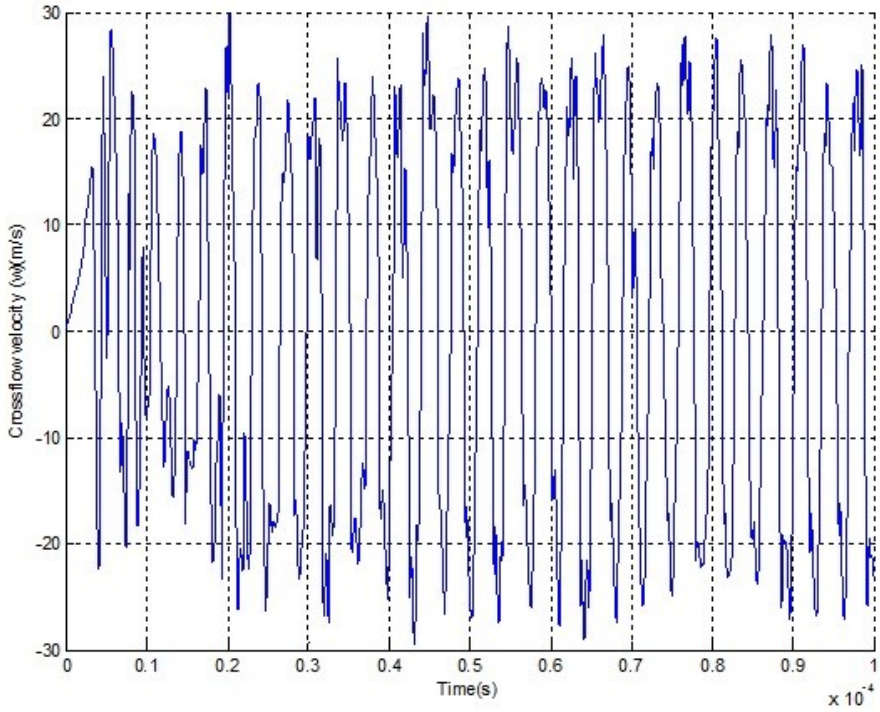

(a) M=0.25

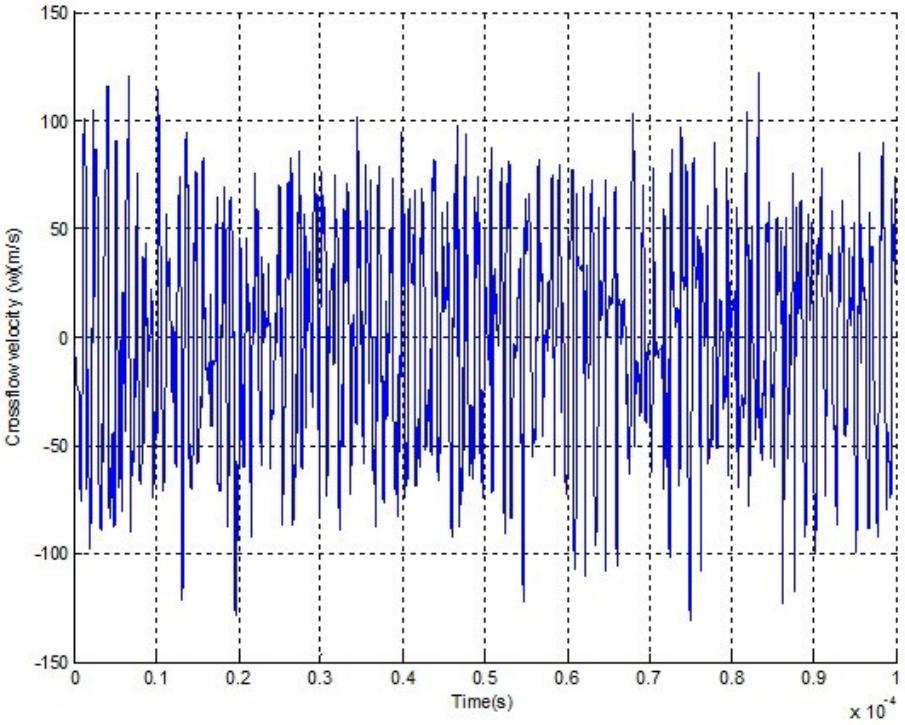

(b) M=0.5

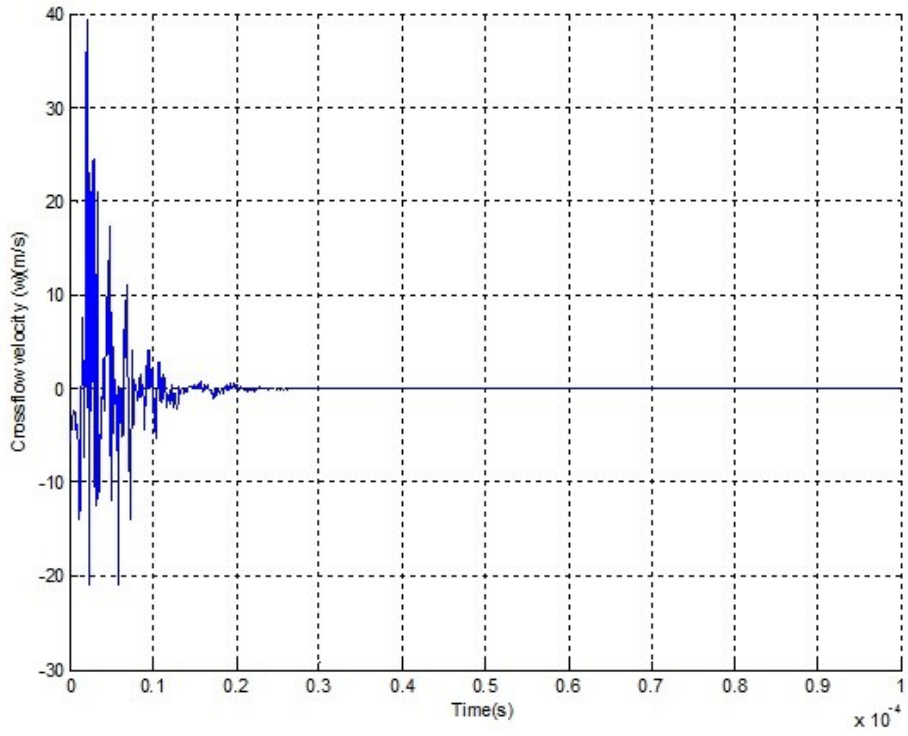

(c) *M=0.75*

Figure 4.11: Time trace of the crossflow velocity (*w*) on the symmetry plane (*z/h=0*) at *y=h/2* and at *x=5h* downstream of the second cube at *Re=1000*.

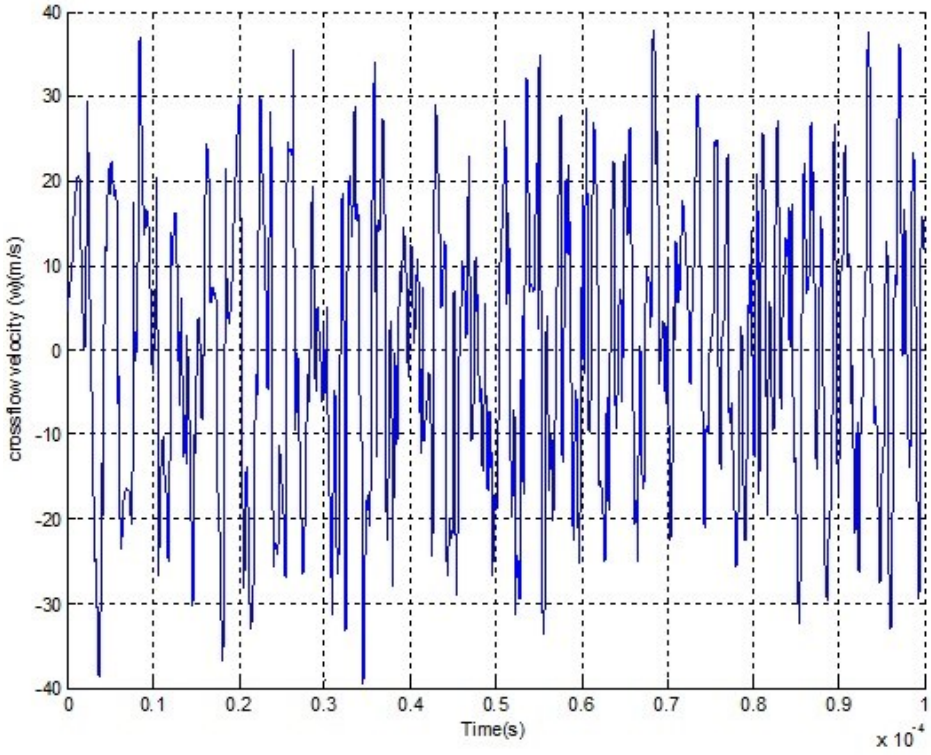
crossflow velocity (w)(m/s)
Time(s)
x 10^-4

(a) M=0.25

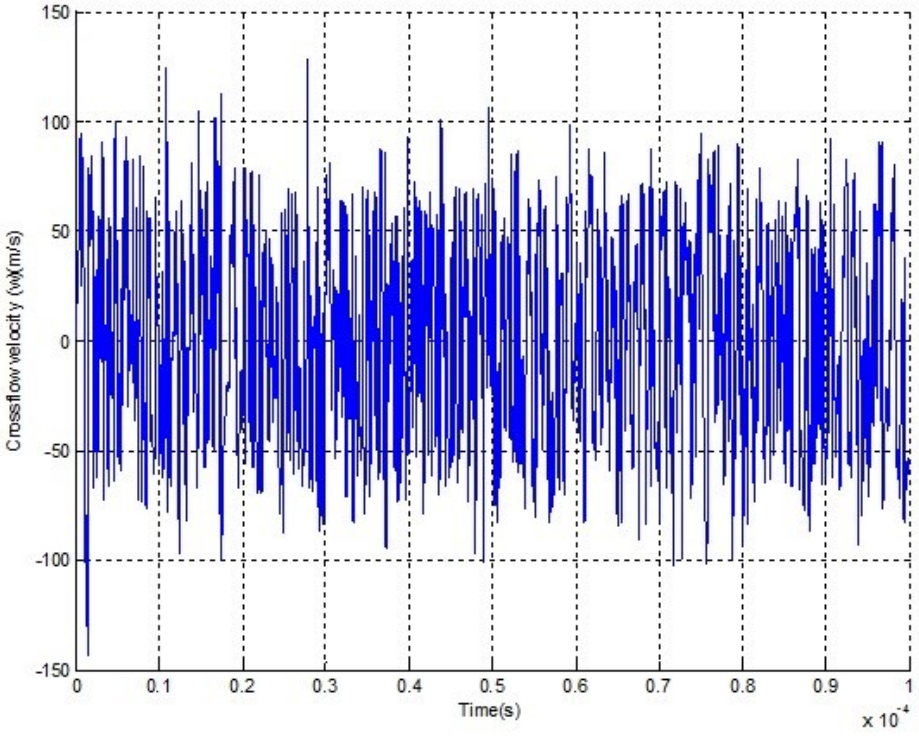
Crossflow velocity (w)(m/s)
Time(s)
x 10^-4

(b) M=0.5

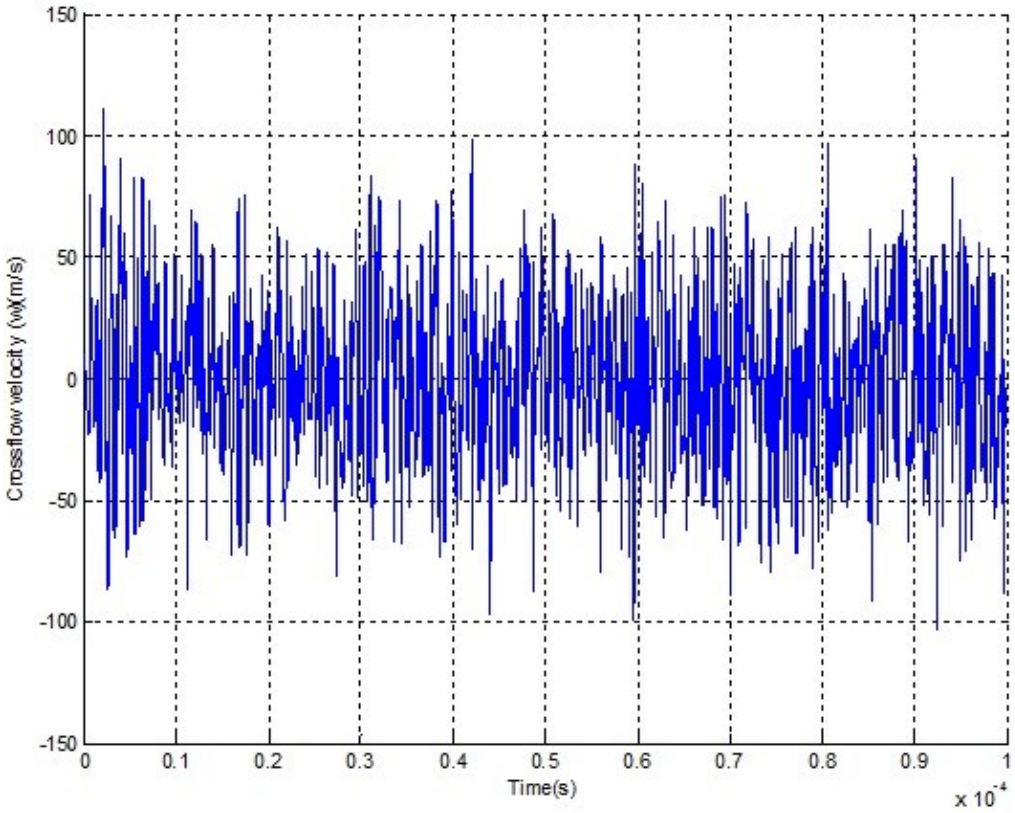

(c) *M=0.75*

Figure 4.12: Time trace of the crossflow velocity (*w*) on the symmetry plane (*z/h=0*) at *y=h/2* and at *x=5h* downstream of the second cube at *Re=2000*.

Figure 4.13, Figure 4.14 and Figure 4.15 show Strouhal number at the same point for several Reynolds and Mach numbers. Strouhal number corresponding to the dominant Fourier component varies with both *Re* and *M*. For low Mach number, the dominant Fourier component hence Strouhal number is well defined and decreases from *St=0.144* to *0.112* as *Re* increases from *500* to *1000* to *2000*. However, as the Mach number increases, either many secondary frequencies or a second dominant frequency appear, indicating a possibility of having two dominant frequencies coexisting under these conditions. Such dual frequency cases were observed in other vortex shedding experiments [41]. Such flow behaviour suggests that the effects of Mach number (hence compressibility) on the flow physics are rather non-liner.

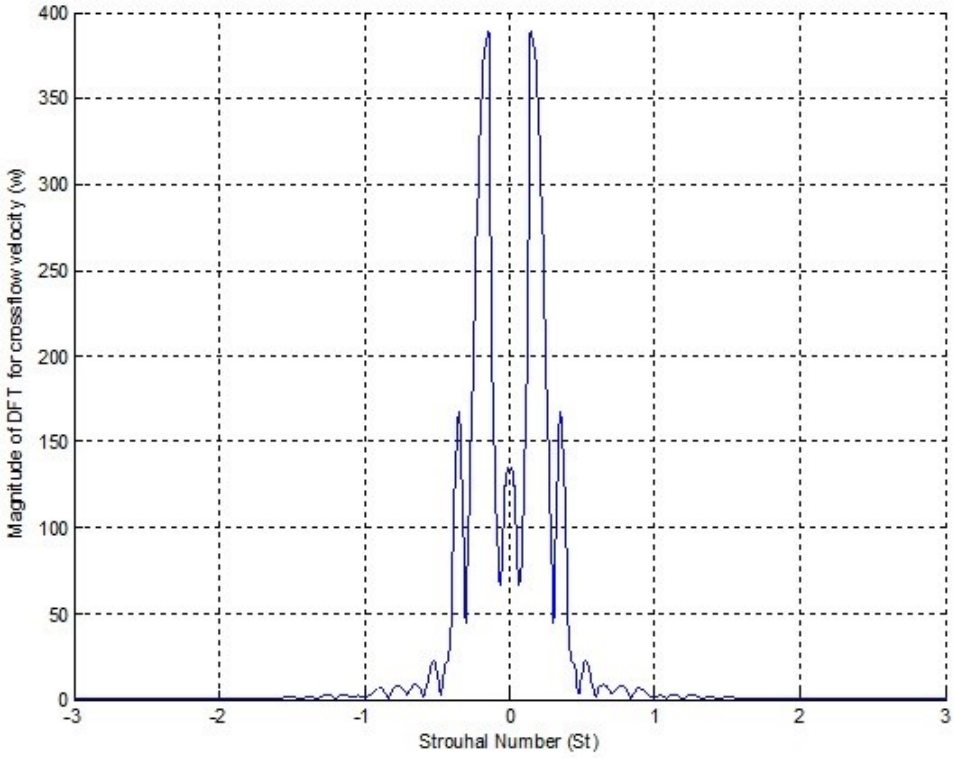
Magnitude of DFT for crossflow velocity (w)
Strouhal Number (St)
400
350
300
250
200
150
100
50
0
-3
-2
-1
0
1
2
3

(a) M=0.25

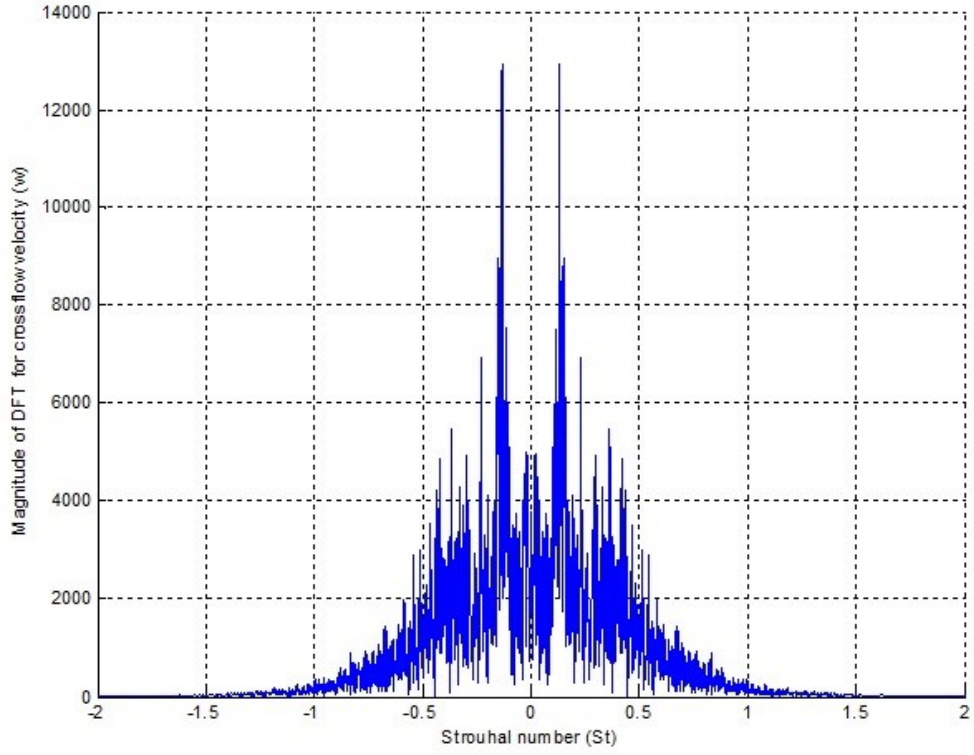
Magnitude of DFT for crossflow velocity (w)
Strouhal number (St)
14000
12000
10000
8000
6000
4000
2000
0
-2
-1.5
-1
-0.5
0
0.5
1
1.5
2

(b) M=0.5

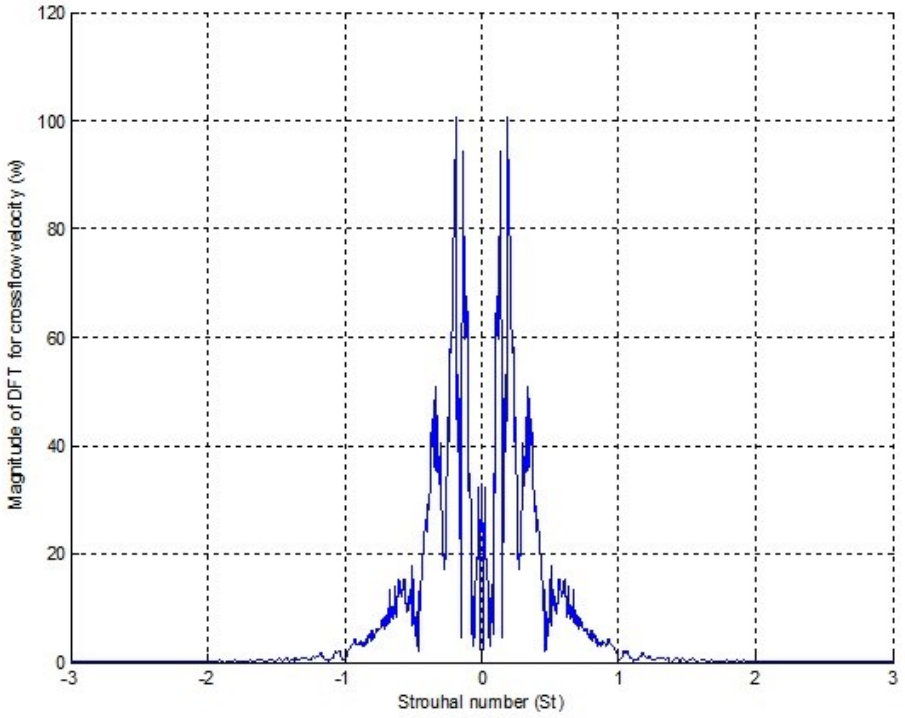

(c) *M=0.75*

Figure 4.13: Strouhal number (*St*) on the symmetry plane (*z/h=0*) at *y=h/2* and at *x=5h* downstream of the second cube at *Re=500*.

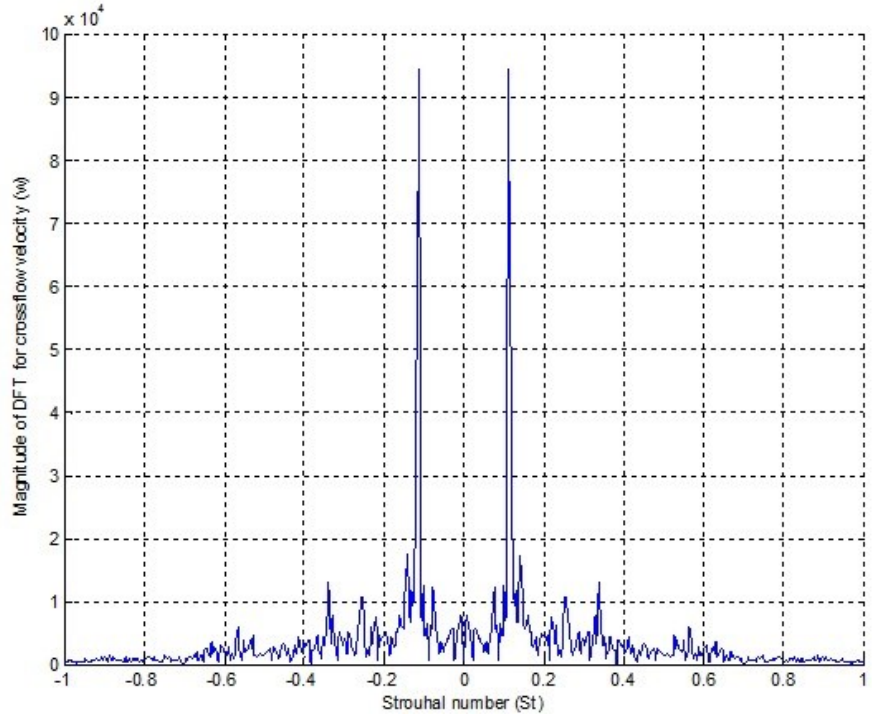

(a) M=0.25

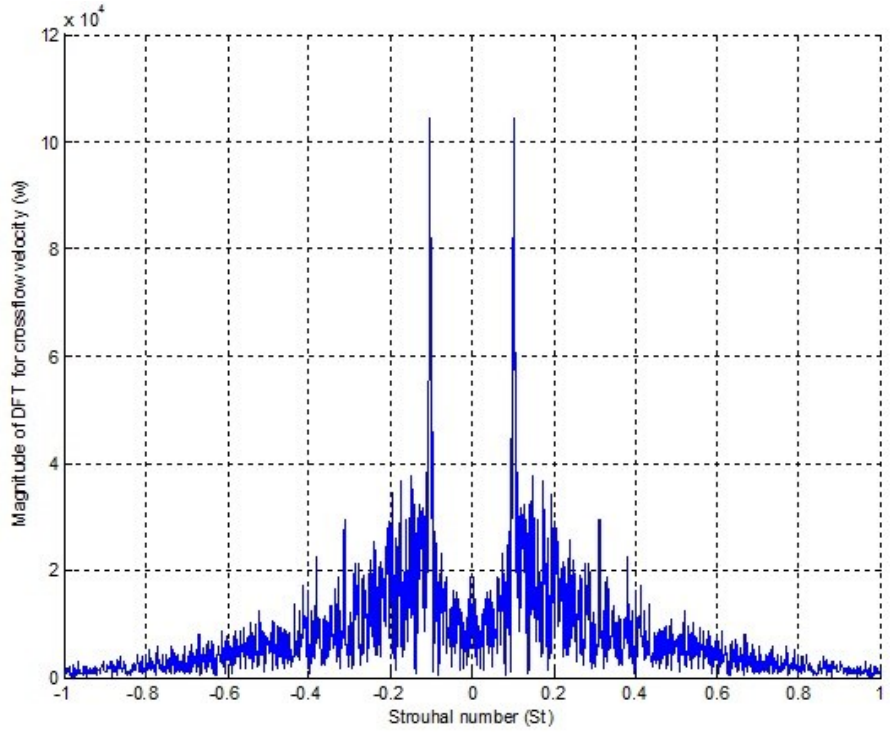

(b) M=0.5

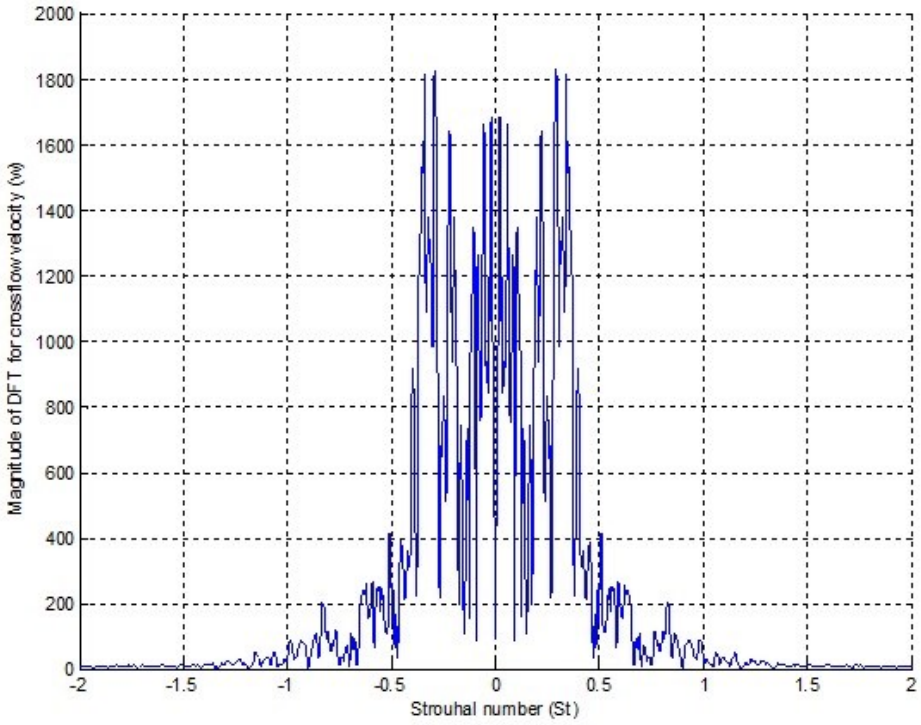

(c) *M=0.75*

Figure 4.14: Strouhal number (*St*) on the symmetry plane (*z/h=0*) at *y=h/2* and at *x=5h* downstream of the second cube at *Re=1000*.

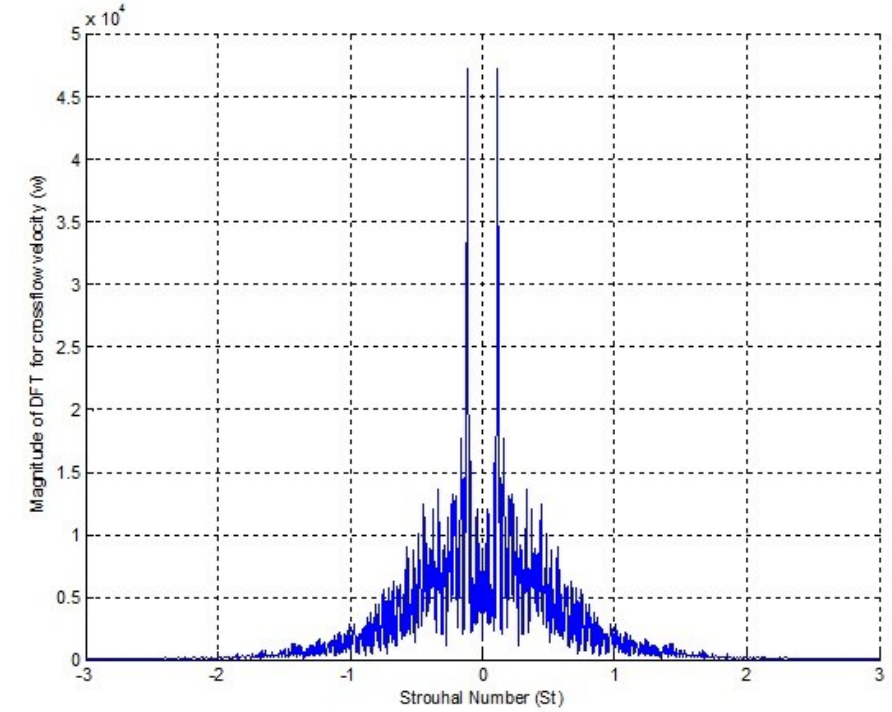
x 10^4
Magnitude of DFT for crossflow velocity (w)
Strouhal Number (St)

(a) M=0.25

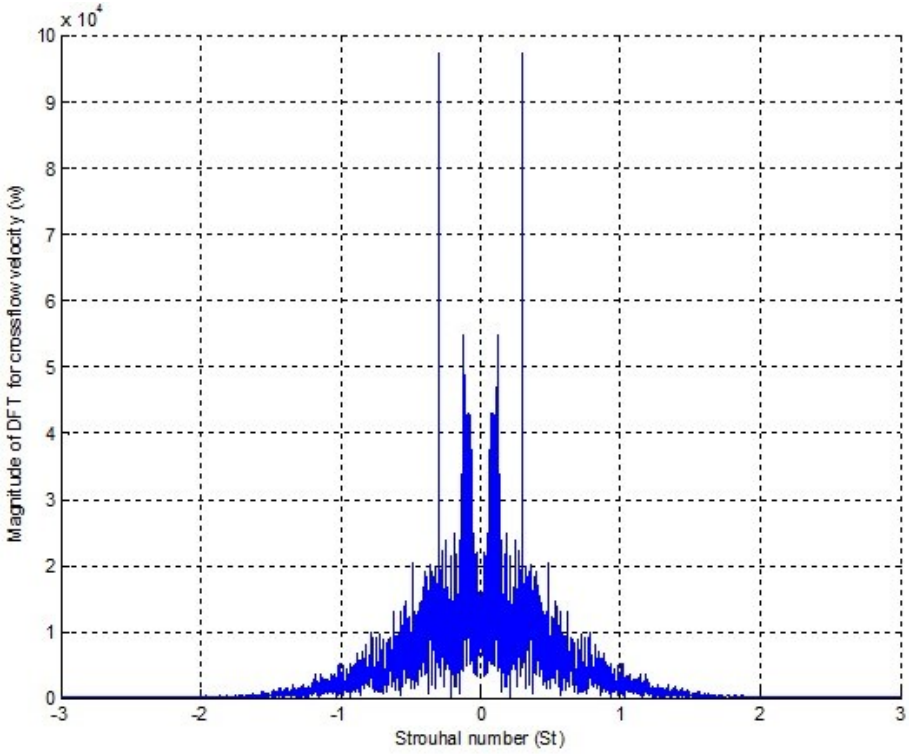
x 10^4
Magnitude of DFT for crossflow velocity (w)
Strouhal number (St)

(b) M=0.5

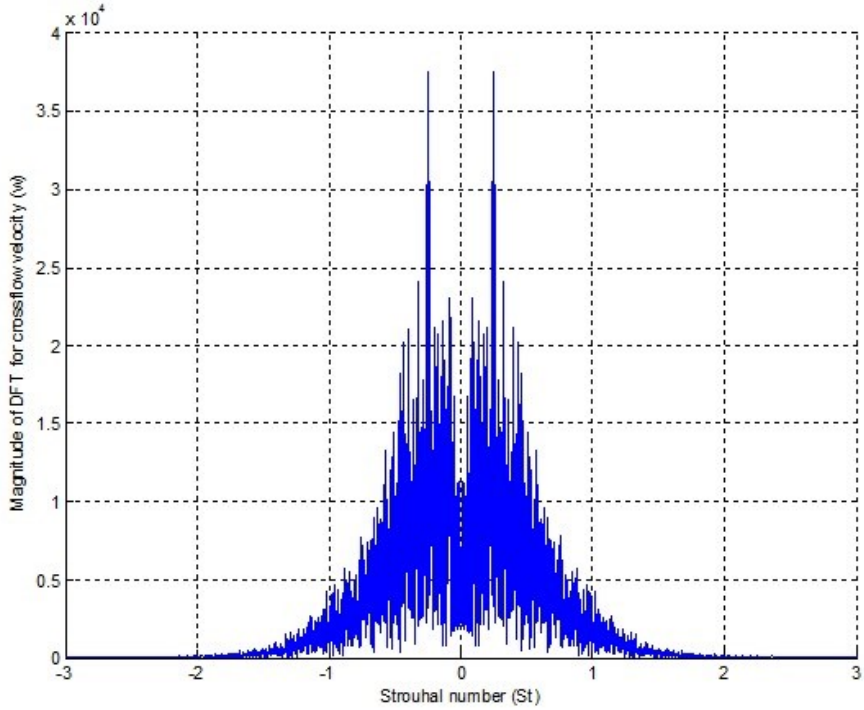

(c) *M=0.75*

Figure 4.15: Strouhal number (*St*) on the symmetry plane (*z/h=0*) at *y=h/2* and at *x=5h* downstream of the second cube at *Re=2000*.

Figure 4.16, Figure 3.17 and Figure 3.18 show Strouhal number along the cube half-height plane (*y/h=0.5*) for Reynolds number values *Re=500*, *1,000* and *2,000*, respectively, at several *z/h* and Mach number values. These figures are complemented with Table 4.8 where *St* number values in the far wake are given. The figures show that all probing points on the symmetry plane (*z/h = 0*) have a periodic signal. It is noticed from these figures that Strouhal number changes value from one probing point to another even if the *2* points are in the same plane. This may be due to several reasons. One is that many small vortices appear behind the second cube so one can notice a low *St* value behind the downstream cube especially for *M=0.5* or *0.75* (i.e. compressible flow). Another is that sometimes the merging of two or more vortex tubes occurs and gives rise to a stronger vortex, in this case Strouhal number changes and the signal gets stronger. Or the vortex could be tilting as it convects downstream so that its motion is fully three dimensional. On the symmetry plane, Strouhal number tends to level off downstream of the cubes, with the distance depending

on the Mach number. Note that, for *M=0.25* (incompressible flow) and *Re≥1,000 the numerical value of St=0.112* while the experimental value reported by Havel *et al.* [37] is 0.11.

Table 4.8: Strouhal number in the far wake at cube half- height (*y/h=0.5*) on the symmetry plane (*z/h=0*).

Re	*M*		
	0.25	0.5	0.75
500	0.148	0.131	0.189
1,000	0.112	0.105	0.292
2,000	0.112	0.300	0.254

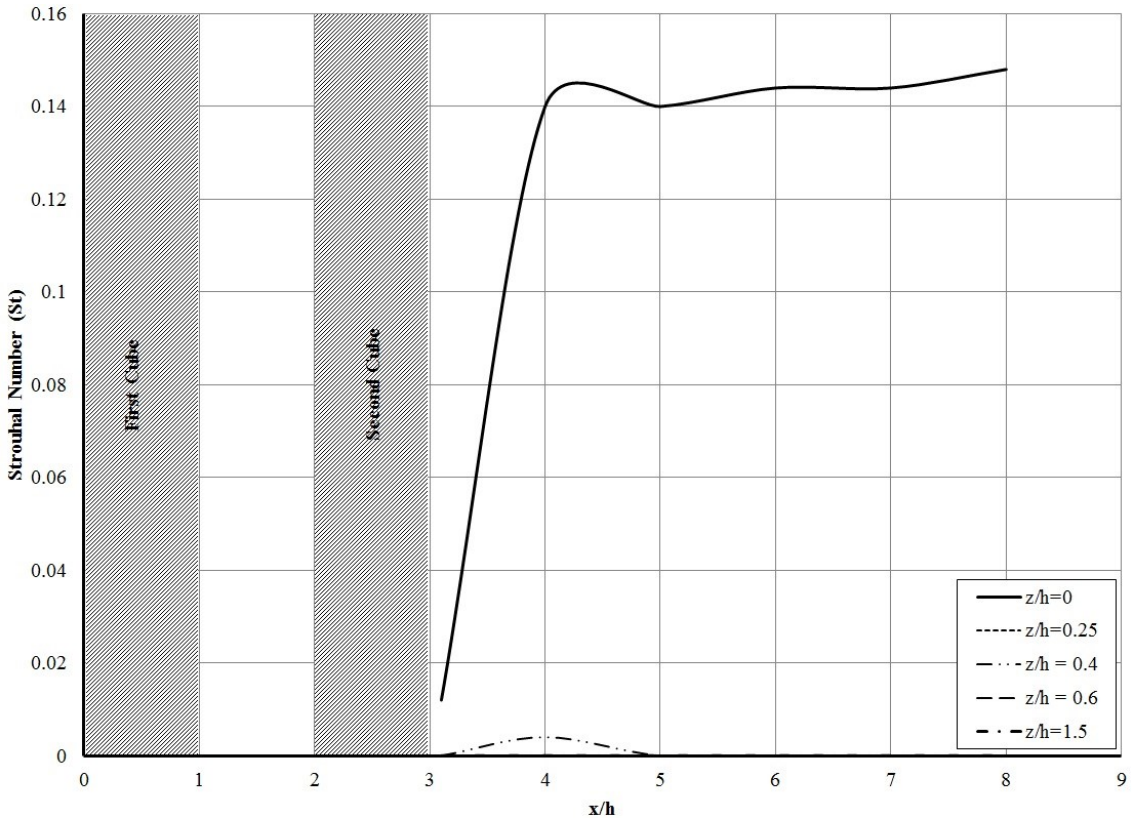

(a) M=0.25

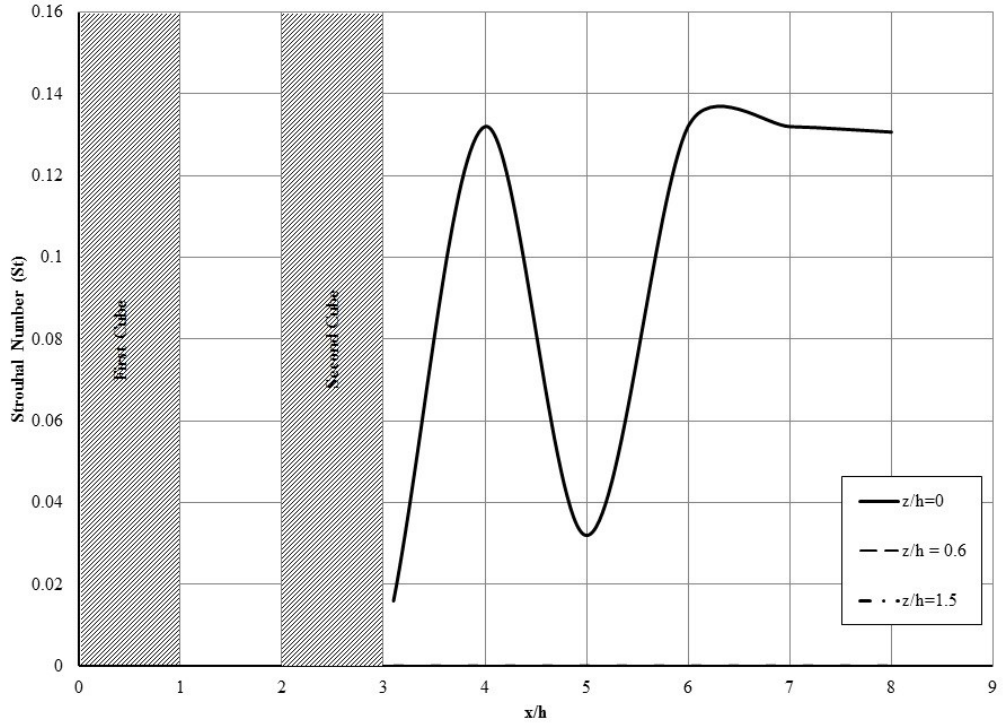

(b) M=0.5

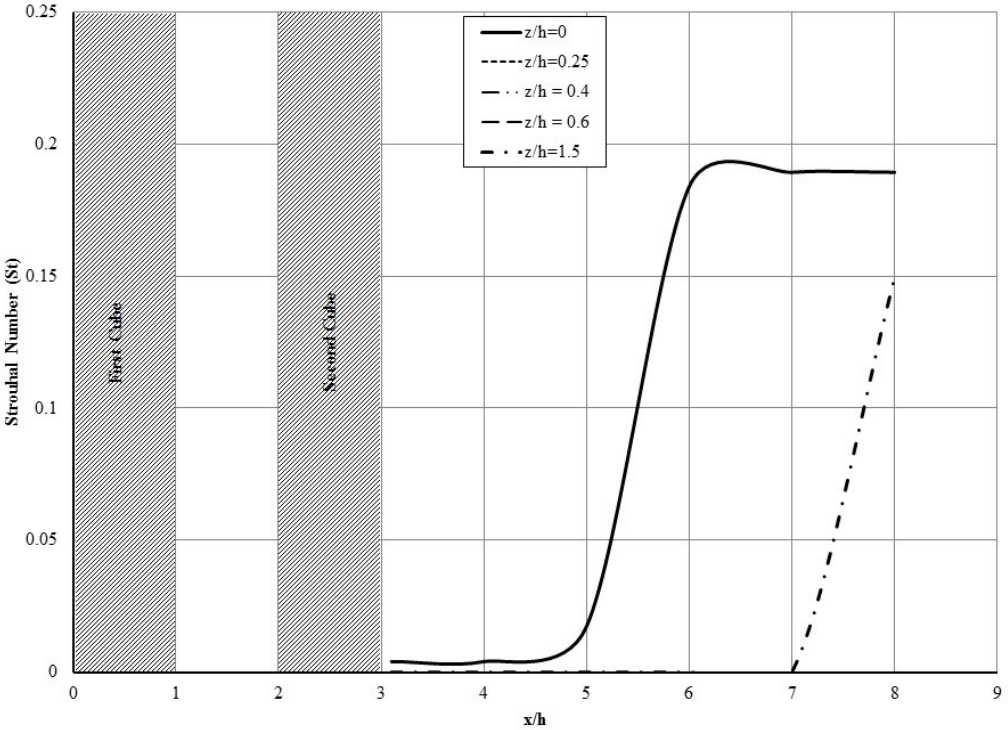

(c) *M=0.75*

Figure 4.16: Strouhal number (*St*) on the cube half-height plane (*y/h=0.5*) at *Re=500* and several *z/h*.

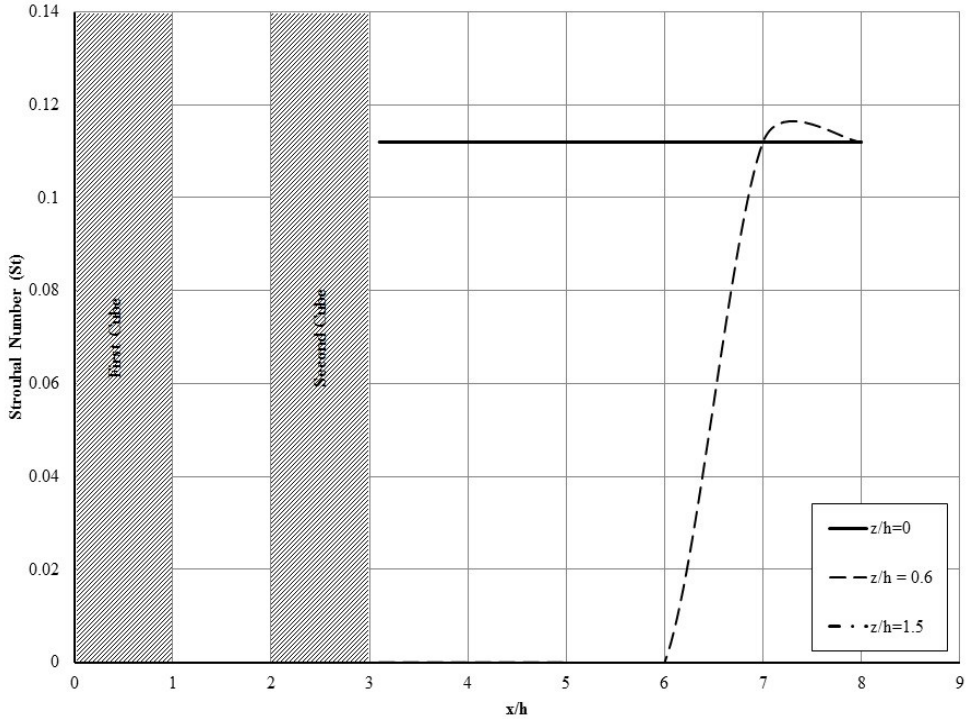
0.14
0.12
0.1
0.08
0.06
0.04
0.02
0
Strouhal Number (St)
First Cube
Second Cube
z/h=0
z/h = 0.6
z/h=1.5
0
1
2
3
4
5
6
7
8
9
x/h

(a) M=0.25

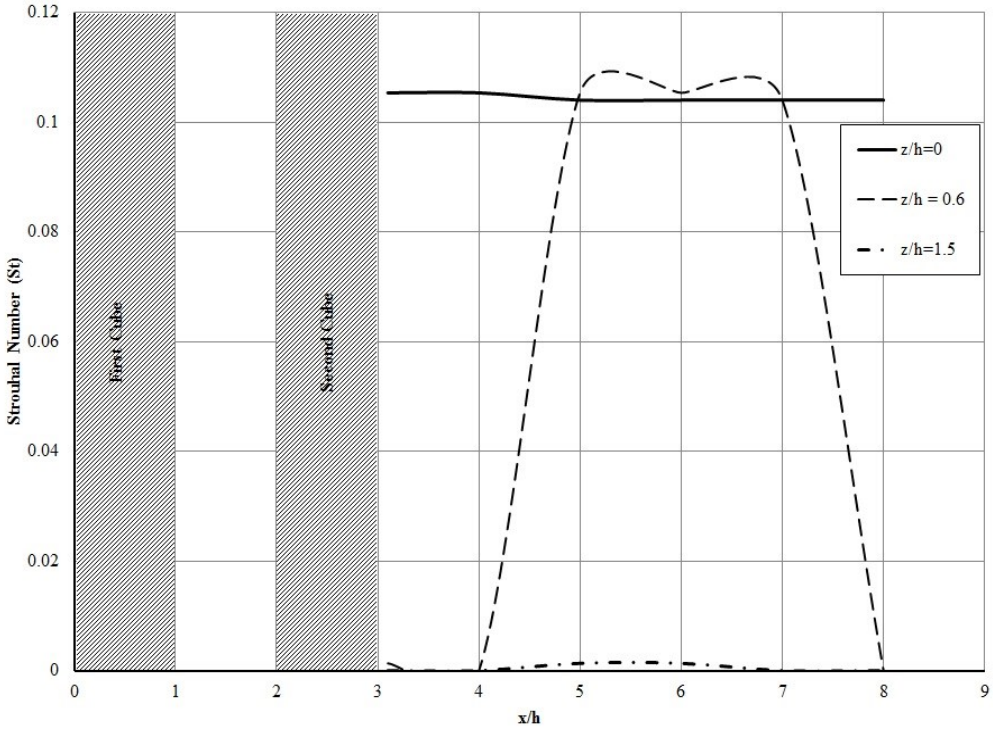
0.12
0.1
0.08
0.06
0.04
0.02
0
Strouhal Number (St)
First Cube
Second Cube
z/h=0
z/h = 0.6
z/h=1.5
0
1
2
3
4
5
6
7
8
9
x/h

(b) M=0.5

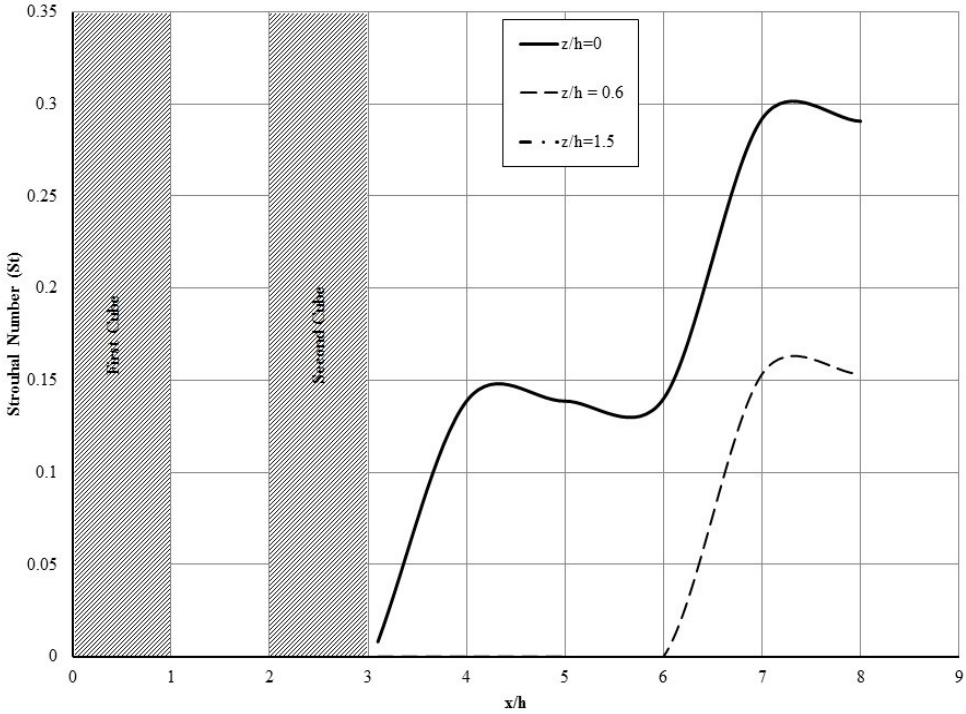

(c) *M=0.75*

Figure 4.17: Strouhal number (*St*) on the cube half-height plane (*y/h=0.5*) at *Re=1000* and several *z/h*.

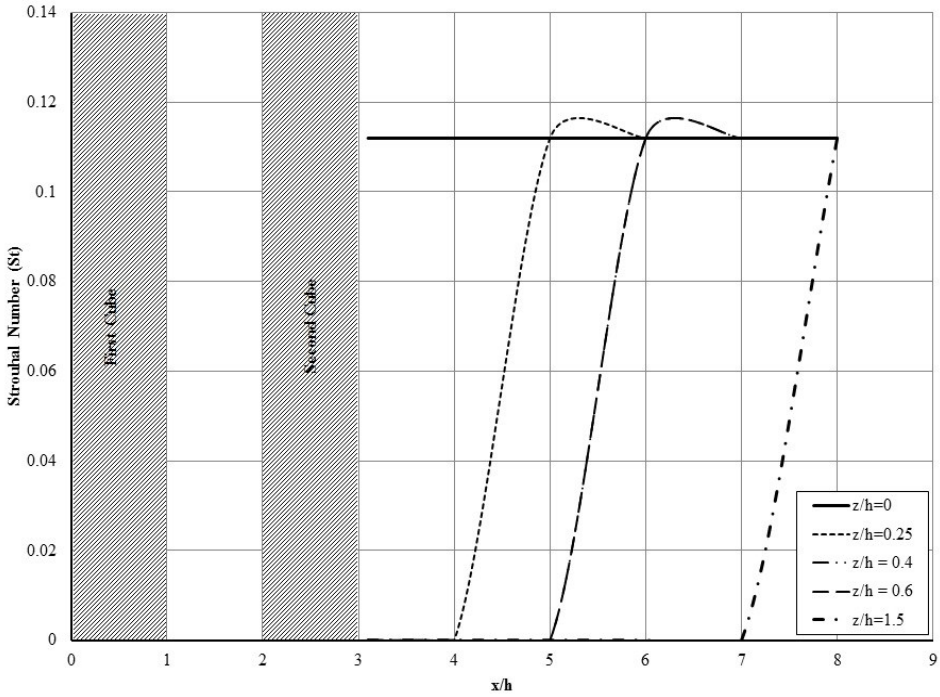

(a) M=0.25

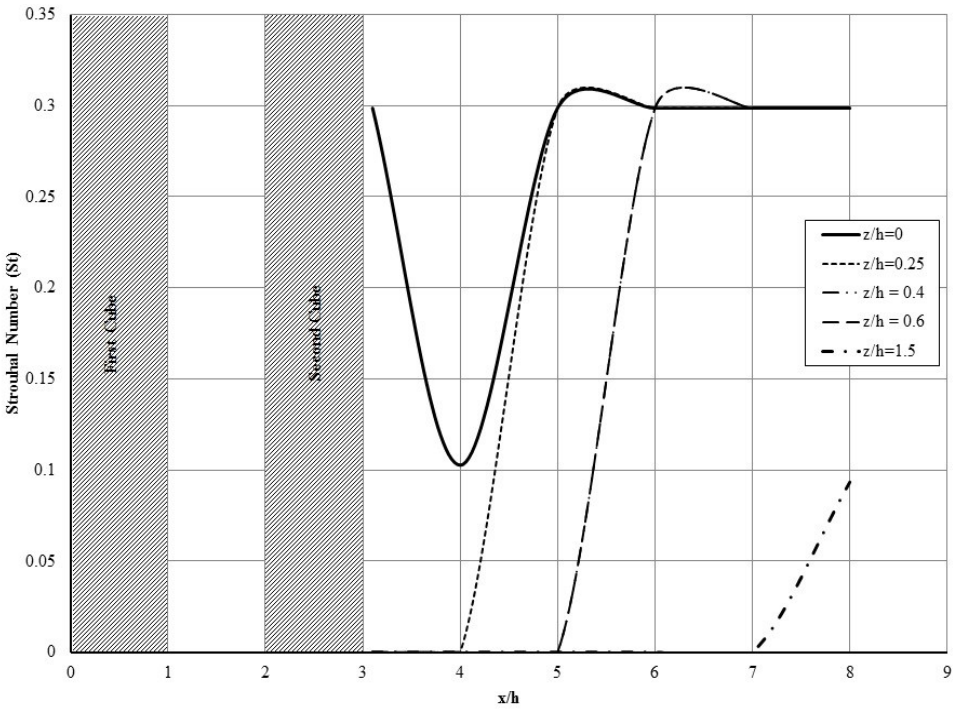

(b) M=0.5

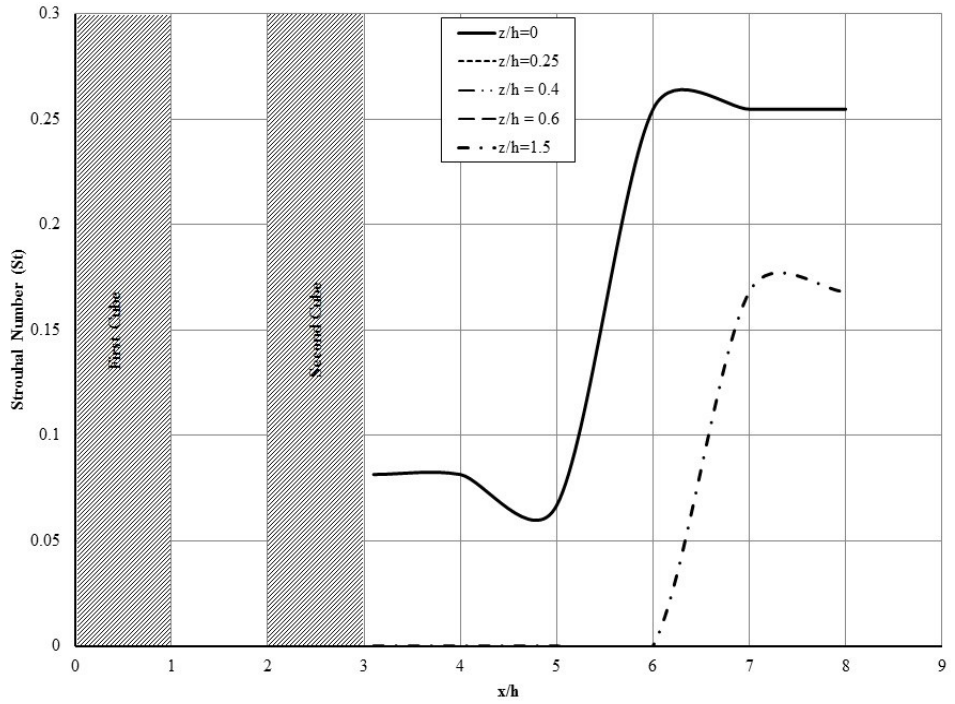

(c) *M=0.75*

Figure 4.18: Strouhal number (*St*) on the cube half-height plane (*y/h=0.5*) at *Re=2000* and several *z/h*.

The variation of *St* versus *M* and *St* versus *Re* at a point located in the far-field (*x=5h*) at the cube half-height (*y=h/2*) and on the symmetry plane (*z/h=0*) are summarized in Figure 4.19. Strouhal number is almost independent of Reynolds number for *M=0.25* whereas for *M=0.5* and *Re ≤ 1000,* Strouhal number exhibits a behavior similar to that at *M=0.25*. By taking the average Strouhal number over all probing points in the symmetry plane for several Mach numbers and Reynolds numbers, as shown in Figure 4.20 and Figure 4.21, Strouhal number behavior with Mach and Reynolds numbers is fairly similar to the local Strouhal number in the far wake (*x=5h*, *y=h/2*, *z/h=0*). Figure 4.7 and Figure 4.19, which represent the variation of Strouhal number (*St*) with the Reynolds number and Mach number in the far wake for *2D* and *3D*, are compared. The trend of *St* vs *Re* is similar only at *M=0.75*. The behavior is almost the same for low *Re* and Mach number.

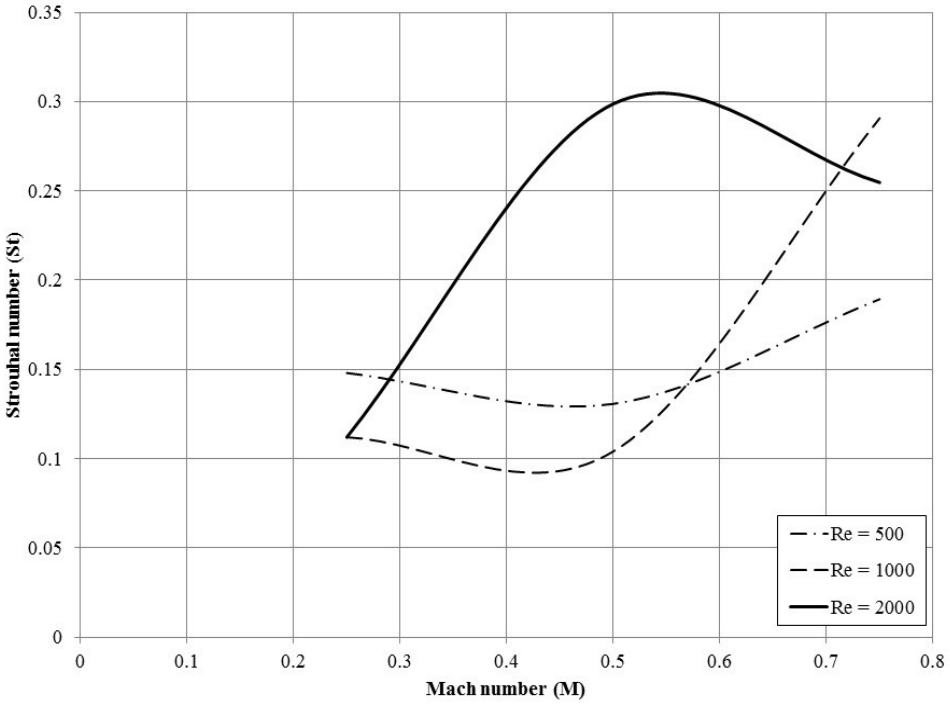

(a) Strouhal number Vs. Mach number

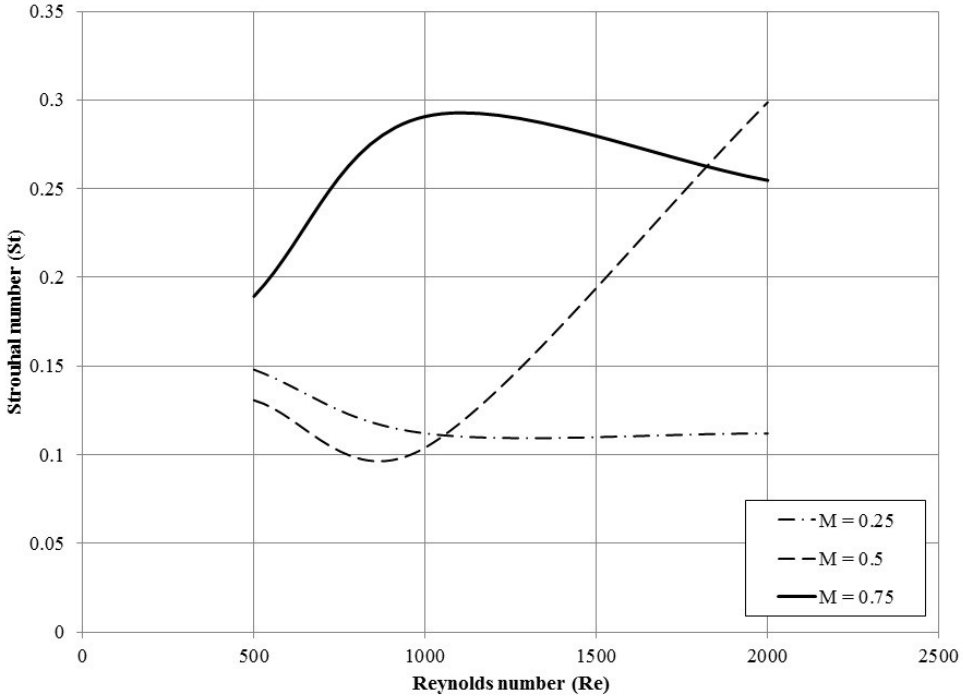

(b) Strouhal number Vs. Reynolds number

Figure 4.19: Strouhal number (*St*) on the symmetry plane (*z/h=0*) at *x=5h* downstream of the second cube.

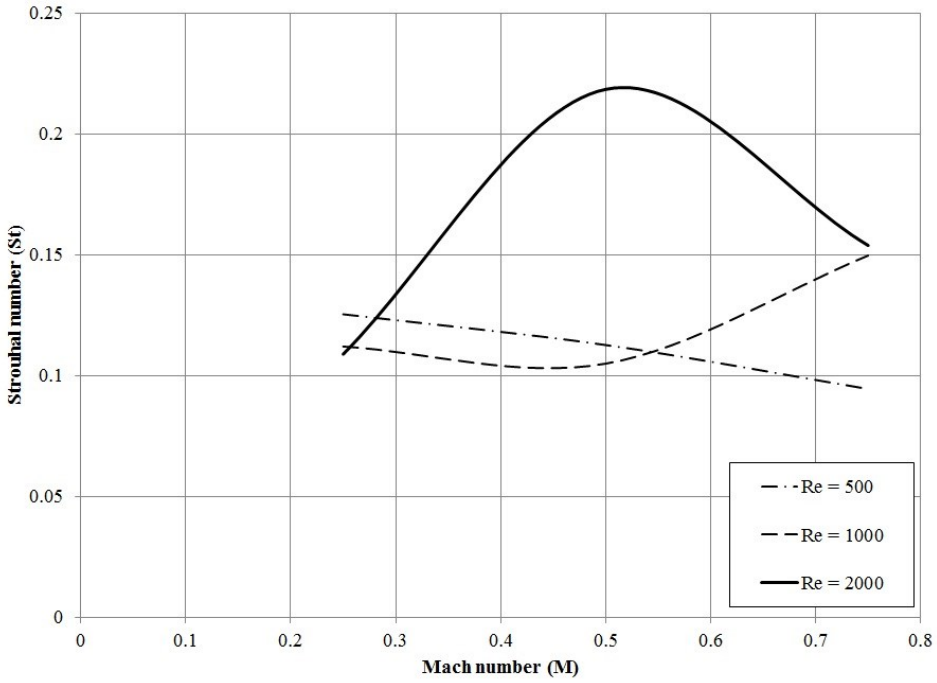

Figure 4.20: Average Strouhal number vs. Mach number on the symmetry plane.

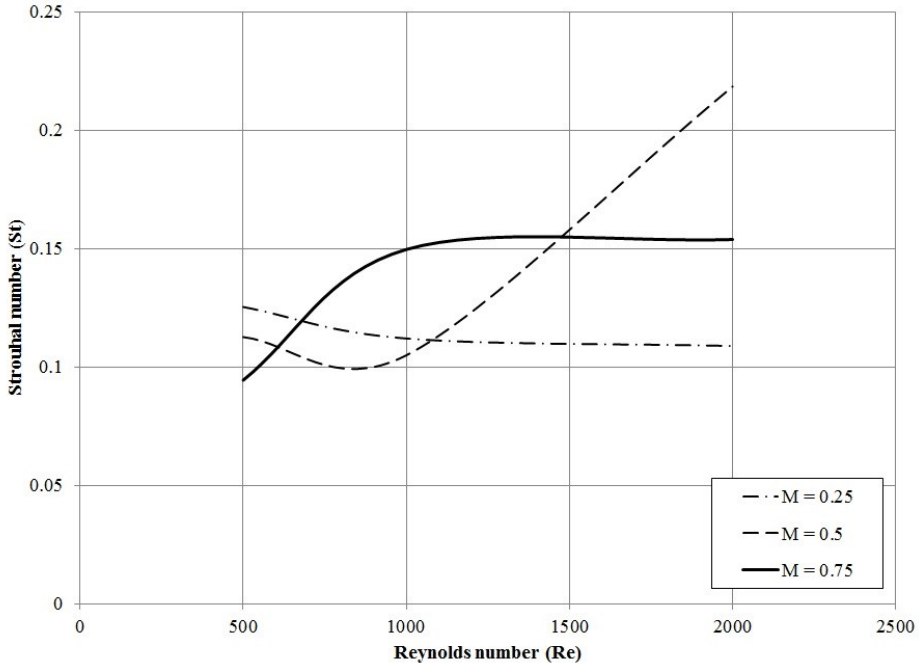

Figure 4.21: Average Strouhal number vs. Reynolds on the symmetry plane.

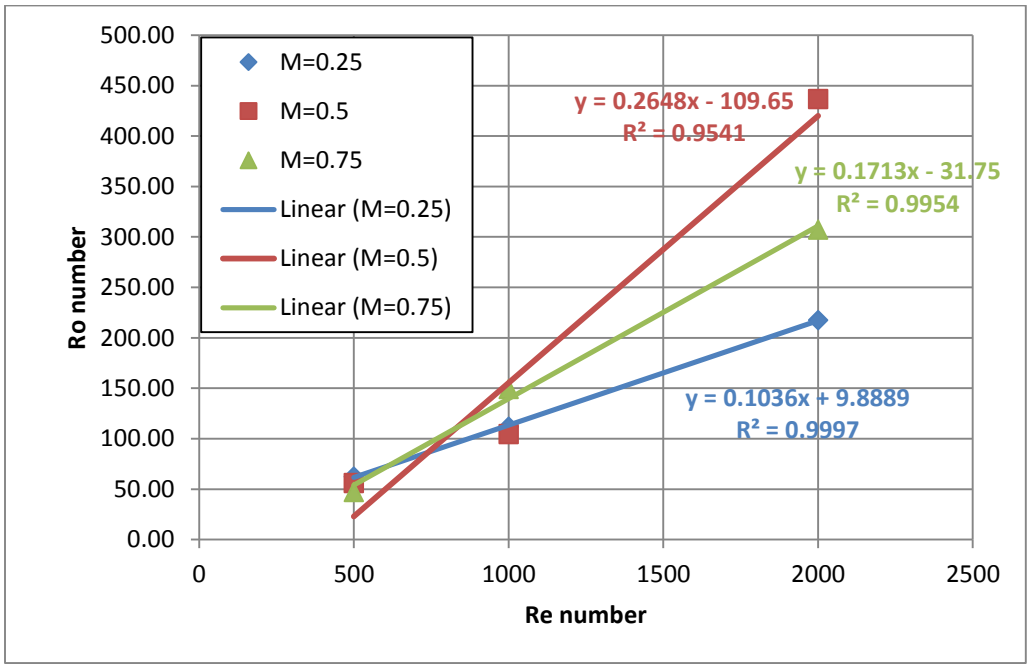

Figure 4.22: Roshko number versus Reynolds number at several Mach number (*3D* flow).

Figure 4.22 shows that a linear fit is a good approximation for the variation of *Ro* with *Re*. It also confirms once more the non-linear nature of compressibility effects.

4.4 Drag coefficient on the cubes

The deflection of the sensitive element is measured, and the force acting on that element is inferred from the element material properties. This force can be computed from the *3D* flow simulations and hence the Reynolds number (hence velocity) corresponding to the deflection, which is a target in the present work. Note that the viscous drag is negligible compared to the pressure drag. The drag coefficient is computed as follows:

Where ρ, V and A are the inflow density, velocity and the cube side area (h^2), see Figure 4.23.

$$C_d = \frac{2}{\rho V^2 A} \iint_A (p_1 - p_2)\, dA \qquad 4.13$$

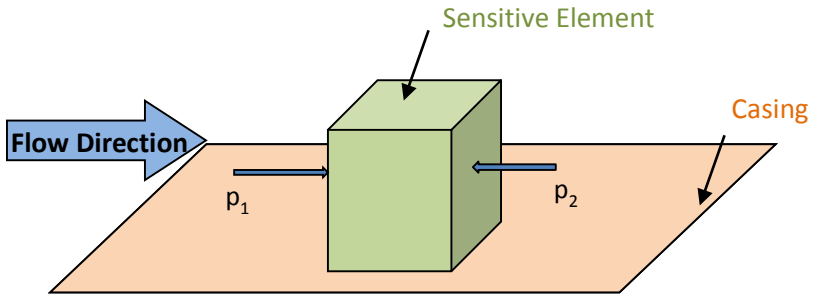

Figure 4.23: Scheme of drag forces acting on the sensitive element.

Figure 4.24 shows that the drag coefficient on the blocking element (1st cube) is always positive and varies between 1.15 and 1.6 for all values of *Re* and *M*. Figure 4.25 shows that the drag coefficient on the sensitive element (2nd cube) is always negative implying that the sensitive element is pushed forward towards the blocking element (1st cube). C_d varies between *-1.2* and *-0.15* for all values of *Re* and *M*, which is a much wider range compared with C_d computed for the blocking element.

More importantly, when the numerical and experimental values of C_d are compared, we find that at *Re=2000* and *M=0.25*, the numerical simulation gives C_d*=1.33* and *-0.69* compared with experimental data [41] where C_d*=1.35* and *-0.5*. This is a rather good agreement given the fact that the experimental data are obtained at *Re=22,000*.

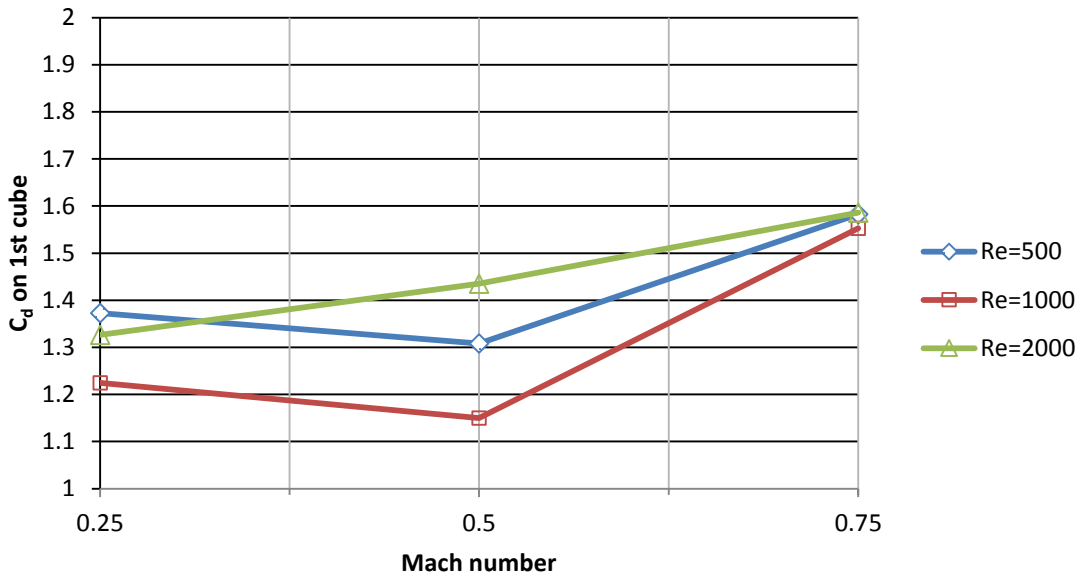

Figure 4.24: Drag coefficient on the blocking element (1st cube) for *S/h=1*.

For the 1st cube, it is expected that C_d will be positive as the pressure on the cube front face will always be close to the stagnation pressure. The flow in the inter-cube cavity will strongly affect the pressure on the 1st cube back side and on the 2nd cube. Figure 4.5 and Figure 4.6, which show the turbulence kinetic energy contours for *S/h=1* and *Re=2000*, indicate that turbulence in the inter-cube cavity is maximum at *M=0.5,* then at *M=0.75* and at *M=0.25*, and the maximum contours are closer to the 2nd cube front face. This turbulence variation implies that the pressure on the 2nd cube front face will be most affected, and that the pressure will be least at *M=0.5* then *M=0.75* then *M=0.25*. This behaviour explains the drag variation on the 2nd cube at *Re=2000*, given in Figure 4.25; the drag is least at *M=0.5* then *M=0.75* then *M=0.5*.

In summary, the drag coefficient C_d values computed numerically and measured experimentally are in good agreement and the drag coefficient is strongly affected by compressibility since the latter affects the flow in the inter-cube cavity.

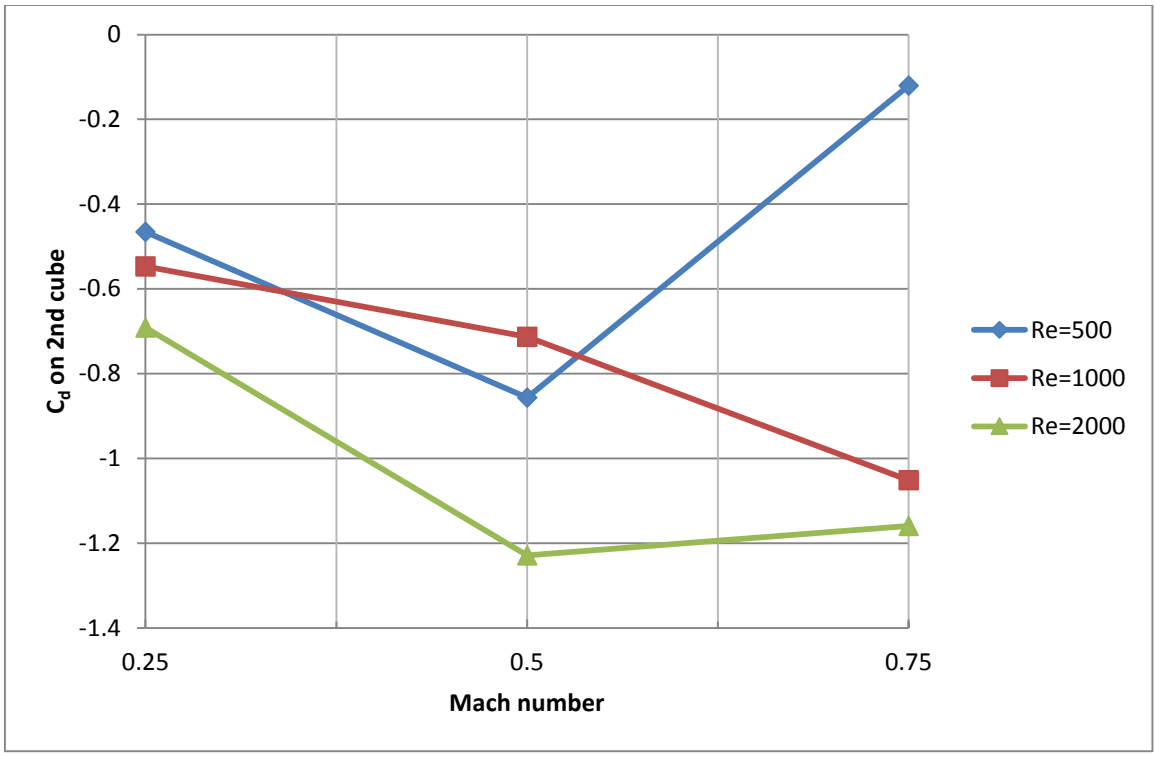

Figure 4.25: Drag coefficient on the sensitive element (2nd cube) for *S/h=1*.

4.5 Concluding remarks

This chapter presents new knowledge and interprets some of it in terms of flow physics as much as possible, and in terms of comparison with available experimental data whenever possible. Some of the key points can be summarized as follows:

- The governing equations are presented and the numerical implementation is described and justified, and key issues are discussed in detail, e.g. the continuum assumption, the Kolmogorov length scale etc.
- Important *2D* and *3D* flow phenomena occurring in the present problem are described in detail and are demonstrated from the numerical simulation results.
- The *3D* nature of vortical flow is demonstrated with vortex contours (as measured by the swirl strength at local centers) and its effect on redistributing the energy within the flow is demonstrated with total pressure contours.

- For incompressible air flow (*M=0.25*), the drag coefficient is in good agreement with experimental data
- For air flow, the vortex shedding seems to correlate better with Roshko number Ro whereas Strouhal number *St* correlated better for water flow (presented in the previous chapter).
- Strouhal number assumes different values at different spatial locations. Three of these locations (or regions) are important: 1- the near wake region (near the 2nd cube back side), 2- the far wake region (near the downstream exit) and 3- the average downstream region (the space downstream of the 2nd cube up to the domain exit).
- The effect of compressibility on turbulence in the inter-cube cavity and its impact on both drag coefficient and vortex shedding is noted.
- The effect of flow compressibility is interpreted in part. More work however, needs to be done to add more knowledge in that area.
- For the proposed sensor, it is recommended to use an inter-element spacing in the range $1.5<S/h<2.5$, which corresponds to the cavity-locked vortex shedding where the shedding is continuous and its frequency is inversely proportional to the inter-cube spacing. Moreover the downstream average vortex shedding is given by a strong signal.

Chapter 5

CONCLUSION

In this work, the fluid dynamic flow behaviour around a proposed micro-sensor geometry is assessed. The sensor is intended for use in micro devices and is represented by two cubes (or elements) set in tandem. The flow is described by the *Navier-Stokes* equations and is solved by Direct Numerical Simulation (*DNS*) using *ANSYS-CFX*. Flow visualization using an existing experimental setup is carried out to visualize the flow pattern around the sensor using the soap film technique, where the flow is considered to be *2D* incompressible. This visualization is intended to verify the *DNS* that is carried out for the same cases. Results for the flow pattern and the vortex shedding frequency that are obtained from both numerical simulations and experimental investigations compare favorably well, for three different values of Reynolds number. This confirms the accuracy and verifies the validity of the numerical approach used in solving this rather difficult problem.

A parametric study on the effect of geometry in the limit of *2D* incompressible flow of water is carried out using the assessed program. This study shows that the inter-element spacing strongly affects the flow in the inter-element cavity; it also shows that the thickness of the downstream element affects the downstream shear layer. Both of these geometric parameters control the vortex shedding in the wake and the drag coefficient particularly on the downstream element. This parametric study also suggests that a 'general' linear correlation between Strouhal and Reynolds numbers (modified to include geometric parameters) is valid for all variables investigated in this work.

The *DNS* of air in the limit of *2D* and *3D* flow is considered at three subsonic inflow Mach numbers and three Reynolds numbers. The flow simulation results are verified against basic flow physics, available experimental data and interpretations of vortex shedding behaviour particularly in *3D* flow. For air flow in the *2D* limit, the vortex shedding frequency expressed in terms of Roshko number seems to correlate better with Reynolds number at all Mach numbers. For both *2D* flow and *3D* flow, the vortex shedding

frequency, flow behaviour and drag coefficient compare reasonably well with available experimental data.

The drag coefficient and Strouhal number computed from the *DNS* together with the drag measured by the micro-sensor can be used to infer the flow pressure and velocity, hence achieving one of the main goals of this work.

5.1 Contributions

The contributions of this research to knowledge can be summarized as follows:

- Experimental visualization and numerical investigations of *2D* incompressible (liquid) flow around two cubes in tandem were carried out and assessed for accuracy, consistency and detailed flow features.
- A parametric study on the effects of geometry and Reynolds number on vortex shedding downstream of the cubes was carried out and compared with available experimental results.
- The parametric study suggests the presence of a 'general' linear correlation between St_M and Re_M (modified to include geometric parameters), valid for all variables presented in this work. Namely,

  $$St_M = 2 \times 10^{-5} Re_M - 0.0474,$$

  with a maximum approximation error of *3.6%*. This correlation gives the flexibility of computing the vortex shedding frequency for a wide range of actual flow conditions and geometric configurations.
- Numerical investigations of *2D* and *3D* compressible (air) flow around two cubes in tandem using *DNS* were carried out and the flow physics was discussed.
- Some of the *3D* vortex structures in the downstream wake were identified and their effect on the flow field was elaborated on.
- Compressibility effect on turbulence in the inter-cubes cavity was found to be strong, hence affecting both the drag coefficient particularly on the sensitive element (downstream element) as well as Roshko number (the dimensionless vortex shedding frequency).

5.2 Concluding remarks

The following points have been concluded from the numerical and experimental investigations:

- The soap film experiment allows for a good visualization of the flow pattern and gives a good approximation of the flow velocity and vortex shedding frequency.
- The *DNS* results of the *2D* flow captured the experimentally visualized flow pattern as well as the average Strouhal number, and agreed rather well with the experimental work.
- The computational resources needed for the *DNS* of *2D* flow are manageable with the currently available computers however, they are prohibitively high for a *3D* flow for the same range of Reynolds number investigated in *2D* flow ($7301<Re<14660$).
- The effect of compressibility on the net pressure force exerted across the sensitive element (the 2nd cube) is fairly strong
- The symmetry plane ($z/h=0$) is the best plane to measure Strouhal number since all probing points located on it have a strong and periodic signal.
- The flow is characterized by vortices shedding, splitting, merging and finally diffusing as they convect downstream
- For $S/h\leq 1$, the flow in the inter-cube cavity has little influence elsewhere
- The crossflow velocity, w, is strongest around $x=0.5h$ to $x=h$ downstream of the second block and Strouhal number is stable along the centerline $z=0$ at distances $x/h>6$. This fact suggests that a good place to measure the vortex shedding frequency would be in a region where $z=0$ and $x/h\geq 6$.
- The distances S (inter-element spacing) and L (element thickness in the flow direction) have a strong impact on the vortex dynamics since they control the vorticity strength developed around the elements.
- In *2D* compressible (air) flow, Roshko number (Ro) correlates linearly with Reynolds number (Re) at all Mach numbers. This implies that, for air flow, the vortex shedding frequency is better represented by Roshko number (rather than Strouhal number).

- In *2D* incompressible flow, the experimental and numerical drag coefficients experience a similar variation with inter-element spacing. The values were slightly different due the difference in Reynolds number between the experimental and numerical simulations.

5.3 Recommendations for the proposed sensor

From the results and discussions of the fluid dynamic flow behaviour around the proposed two-element geometry proposed for the sensor and presented in this work, it is possible to make some recommendations for constructing the proposed sensor.

- The average Strouhal number downstream of the two-cube configuration is independent of Reynolds number in the investigated range, $St=0.194$, when $S/h=1$
- The ratio of cube-spacing to cube-side should be chosen in the range of $1.5<S/h<2.5$, where vortex shedding is continuous and where the frequency scales inversely with S (known as the cavity-locked vortex shedding regime).
- The effect of compressibility on the net force exerted across the sensitive element (the 2nd cube) is rather strong and should be accounted for in sensor design.
- Buffeting of the sensitive element due to vortex shedding can be used to infer the vortex shedding frequency hence allowing for computing the flow velocity from *DNS* results

5.4 Recommendations for future work

The present work can be extended in the following directions:

- Account for inflow turbulence by introducing a statistical distribution for the inflow variables that is consistent with turbulent flow.
- For *3D* flow simulations, extend the range of Reynolds number (based on sensor dimensions and flow velocity) to more interesting values (10^4 to 10^5) by assessing several turbulence models against *DNS* results obtained so far and using the most promising turbulence model.
- *DNS* of the flow in the *2D* limit, provided useful insight into the incompressible problem. It should be used further to give a deeper insight into the effects of

compressibility, Reynolds number and geometry over the operating range of a gas turbine engine

- Design, manufacture and test the proposed micro-sensor, based on the present results,

REFERENCES

[1] H. Pfoertner, "Status of Gas Turbine Engine Design and Challenges," NATO Research and Technology Organization, Lecture 2010.

[2] J. S. Wilson, *Sensor technology handbook*: Elsevier, 2004.

[3] H. Bartelt and H. Unzeitig, "Design and investigation of micromechanical bridge structures for an optical pressure sensor with temperature compensation," *Sensors and Actuators A: Physical,* vol. 37, pp. 167-170, 1993.

[4] C. V. Collett and A. D. Hope, *Engineering measurements*: Pitman, 1983.

[5] I. Stiharu, "Sensors Requirements and Roadmaps Part 1," NATO Research and Technology Organization, Lecture2010.

[6] Y. MIHARA. *Measurement of Oil-film pressure and strain distribution in engine and machine elements using a thin-film sensor*.

[7] J. D. Wrbanek, G. C. Fralick, C. A. Blaha, A. R. Busfield, and V. D. Thomas, *A multilayered thin film insulator for harsh environments*: National Aeronautics and Space Administration, Glenn Research Center, 2002.

[8] L. C. Martin, J. D. Wrbanek, and G. C. Fralick, "Thin film sensors for surface measurements [in aerospace simulation facilities]," in *ICIASF 2001 Record. 19th International Congress on Instrumentation in Aerospace Simulation Facilities, 27-30 Aug. 2001*, Piscataway, NJ, USA, 2001, pp. 196-203.

[9] J. D. Wrbanek and K. L. Laster, "Preparation and analysis of platinum thin films for high temperature sensor applications," *NASA/TM-2005-213433,* pp. 1-19, 2005.

[10] A. S. Leo, Ion; Bhat, Rama B.; Moustapha, Hany, "Micro Pressure Sensor for High Temperature Applications," 2007.

[11] H. J. Kleebe, H. Störmer, S. Trassl, and G. Ziegler, "Thermal stability of SiCN ceramics studied by spectroscopy and electron microscopy," *Applied organometallic chemistry,* vol. 15, pp. 858-866, 2001.

[12] C. A. Lewinsohn, P. Colombo, I. Reimanis, and Ö. Ünal, "Stresses occurring during joining of ceramics using preceramic polymers," *Journal of the American Ceramic Society,* vol. 84, pp. 2240-2244, 2001.

[13] Y. Liu, R. Luo, L. An, V. Bright, M. Dunn, J. Daily*, et al.*, "Fabrication of SiCN MEMS structures using microforged molds," in *Micro Electro Mechanical Systems, 2001. MEMS 2001. The 14th IEEE International Conference on*, 2001, pp. 118-121.

[14] C. Haluschka, C. Engel, and R. Riedel, "Silicon carbonitride ceramics derived from polysilazanes Part II. Investigation of electrical properties," *Journal of the European Ceramic Society,* vol. 20, pp. 1365-1374, 2000.

[15] C.-Y. Lee, C.-Y. Wen, H.-H. Hou, R.-J. Yang, C.-H. Tsai, and L.-M. Fu, "Design and characterization of MEMS-based flow-rate and flow-direction microsensor," *Microfluidics and nanofluidics,* vol. 6, pp. 363-371, 2009.

[16] G. L. Pankanin, "The vortex flowmeter: various methods of investigating phenomena," *Measurement science and technology,* vol. 16, p. R1, 2005.

[17] H. Yamasaki and M. Rubin, "The vortex flowmeter," in *Flow: Its measurement and control in science and industry, 10-14 May 1971*, Pittsburgh, PA, USA, 1974, pp. 975-83.
[18] H. Kim and P. Durbin, "Observations of the frequencies in a sphere wake and of drag increase by acoustic excitation," *Physics of Fluids (1958-1988),* vol. 31, pp. 3260-3265, 1988.
[19] R. T. Keefe, "Investigation of the fluctuating forces acting on a stationary circular cylinder in a subsonic stream and of the associated sound field," *The Journal of the Acoustical Society of America,* vol. 34, pp. 1711-1714, 1962.
[20] T. Cousins, S. Foster, and P. Johnson, "A linear and accurate flowmeter using vortex shedding," in *Proc. Power Fluid for Process Control Symposium, Inst. Measurement and Control, Guildford*, 1973, pp. 45-46.
[21] R. A. Benson and J. P. Bentley, "Design and performance evaluation of optimal multiple bluff body vortex flowmeters," *Transactions of the Institute of Measurement and Control,* vol. 15, pp. 239-47, / 1993.
[22] J. P. Bentley, R. A. Benson, and A. J. Shanks, "The development of dual bluff body vortex flowmeters," *Flow Measurement and Instrumentation,* vol. 7, pp. 85-90, 06/ 1996.
[23] J. P. Bentley and J. W. Mudd, "Vortex shedding mechanisms in single and dual bluff bodies," *Flow Measurement and Instrumentation,* vol. 15, pp. 23-31, 03/ 2003.
[24] J. H. Ferziger and M. Peri*c, *Computational methods for fluid dynamics*, 2nd rev. ed. Berlin ; New York: Springer, 1999.
[25] D. C. Wilcox, *Turbulence modeling for CFD*, 1st ed. La Cãnada, CA: DCW Industries, Inc., 1993.
[26] "ANSYSY CFX-Solver Theory Guide Release 12.1," ANSYS, Inc., Canonsburg, PA2009.
[27] P. Spalart, W. Jou, M. Strelets, and S. Allmaras, "Comments on the feasibility of LES for wings, and on a hybrid RANS/LES approach," *Advances in DNS/LES,* vol. 1, pp. 4-8, 1997.
[28] H. Oertel Jr, "Wakes behind blunt bodies," *Annual Review of Fluid Mechanics,* vol. 22, pp. 539-562, 1990.
[29] C. H. Williamson, "Vortex dynamics in the cylinder wake," *Annual review of fluid mechanics,* vol. 28, pp. 477-539, 1996.
[30] A. Roshko, "Experiments on the flow past a circular cylinder at very high Reynolds number," *Journal of Fluid Mechanics,* vol. 10, pp. 345-356, 1961.
[31] E. Achenbach, "Experiments on the flow past spheres at very high Reynolds numbers," *Journal of Fluid Mechanics,* vol. 54, pp. 565-575, 1972.
[32] M. Breuer, "A challenging test case for large eddy simulation: high Reynolds number circular cylinder flow," *International Journal of Heat and Fluid Flow,* vol. 21, pp. 648-654, 2000.
[33] S. Murakami and A. Mochida, "Turbulent vortex shedding flow past 2D square cylinder predicted by CFD," *Journal of Wind Engineering and Industrial Aerodynamics,* vol. 54-55, pp. 191-211, 1995.

[34] A. Sohankar, C. Norberg, and L. Davidson, "Simulation of three-dimensional flow around a square cylinder at moderate Reynolds numbers," *Physics of Fluids,* vol. 11, pp. 288-306, 02/ 1999.
[35] S. C. Yen and J. H. Liu, "Wake flow behind two side-by-side square cylinders," *International Journal of Heat and Fluid Flow,* vol. 32, pp. 41-51, 02/ 2011.
[36] Y. Yamagishi, S. Kimura, and M. Oki, "Flow characteristics around a square cylinder with changing chamfer dimensions," *Journal of visualization,* vol. 13, pp. 61-68, 2010.
[37] B. Havel, H. Hangan, and R. Martinuzzi, "Buffeting for 2D and 3D sharp-edged bluff bodies," *Journal of Wind Engineering and Industrial Aerodynamics,* vol. 89, pp. 1369-1381, 2001.
[38] R. J. Martinuzzi and B. Havel, "Turbulent flow around two interfering surface-mounted cubic obstacles in tandem arrangement," *Journal of fluids engineering,* vol. 122, pp. 24-31, 2000.
[39] R. J. Martinuzzi and B. Havel, "Vortex shedding from two surface-mounted cubes in tandem," *International journal of heat and fluid flow,* vol. 25, pp. 364-372, 2004.
[40] H. Sakamoto and H. Haniu, "Aerodynamic forces acting on two square prisms placed vertically in a turbulent boundary layer," *Journal of Wind Engineering and Industrial Aerodynamics,* vol. 31, pp. 41-66, 1988.
[41] M. Farhadi and K. Sedighi, "Flow over two tandem wall-mounted cubes using large eddy simulation," *Proceedings of the Institution of Mechanical Engineers, Part C: Journal of Mechanical Engineering Science,* vol. 222, pp. 1465-1475, 2008.
[42] J. Paik, F. Sotiropoulos, and F. Porté-Agel, "Detached eddy simulation of flow around two wall-mounted cubes in tandem," *International Journal of Heat and Fluid Flow,* vol. 30, pp. 286-305, 2009.
[43] A. Yakhot, H. Liu, and N. Nikitin, "Turbulent flow around a wall-mounted cube: A direct numerical simulation," *International journal of heat and fluid flow,* vol. 27, pp. 994-1009, 2006.
[44] Y. Q. Wang, P. L. Jackson, and J. Sui, "Simulation of Flow Around a Surface-Mounted Square-Section Cylinder of Aspect Ratio Four," in *20th Annual Conference of the CFD Society of Canada*, 2012.
[45] M. Rutgers, X. Wu, and W. Daniel, "Conducting fluid dynamics experiments with vertically falling soap films," *Review of Scientific Instruments,* vol. 72, pp. 3025-3037, 2001.
[46] B. R. Munson, D. F. Young, and T. H. Okiishi, *Fundamentals of fluid mechanics*, 4th ed. New York: Wiley, 2002.
[47] P. Dyson, R. Ransing, P. H. Williams, and R. Williams, *Fluid properties at nano/meso scale: a numerical treatment* vol. 1: John Wiley & Sons, 2008.
[48] N.-T. Nguyen and S. T. Wereley, *Fundamentals and applications of microfluidics*, 2nd ed. Boston: Artech House, 2006.
[49] R. D. Moser and P. Moin, "The effects of curvature in wall-bounded turbulent flows," *Journal of Fluid Mechanics,* vol. 175, pp. 479-510, 1987.

[50] T. Takeuchi and M. Matsumoto, "Aerodynamic response characteristics of rectangular cylinders in tandem arrangement," *Journal of Wind Engineering and Industrial Aerodynamics,* vol. 41, pp. 565-575, 1992.
[51] T. B. Gatski and J.-P. Bonnet, *Compressibility, turbulence and high speed flow*. Amsterdam ; London: Elsevier, 2009.
[52] "ANSYS CFX-Solver Modeling Guide Release 12.1," ANSYS, Inc., Canonsburg, PA2009.
[53] A. Leo, "communications about the experimental work setting and measuring in Ref. [8]," ed, 2009.
[54] R. W. Fox and A. T. McDonald, *Introduction to fluid mechanics*, 4th ed. New York: J. Wiley, 1992.

Appendix A

Pressure micro sensor: aerodynamic modeling

In the literature, two configurations of twin bluff bodies were tested experimentally [10], [39] and then used to assess the *CFD* method used in this work. The most appropriate model was retained and used in the twin bluff body configuration that is the focus of this work.

A.1. Experimental work

The experimental work done by Leo *et al.* [10] demonstrated that the deflection of the sensitive element was caused by the depression occurring in the wake behind the blocking element. Figure 1.2 shows a scaled up model of the experimental set up where compressed air was injected above the blocking element through a duct. Spacing shim rings were used to change the spacing between the blocking and the sensitive elements. Finally, the sensitive element deflection was measured for duct air pressures varying between 1 and 4 psi for several spacing between the elements (namely, *0.6*, *0.9* and *1.5* mm), as shown in Figure A.1. However, the experimental work did not measure the fluid flow parameters such as velocity, pressure and temperature, but focused on the deflection of the sensitive element for several duct pressures.

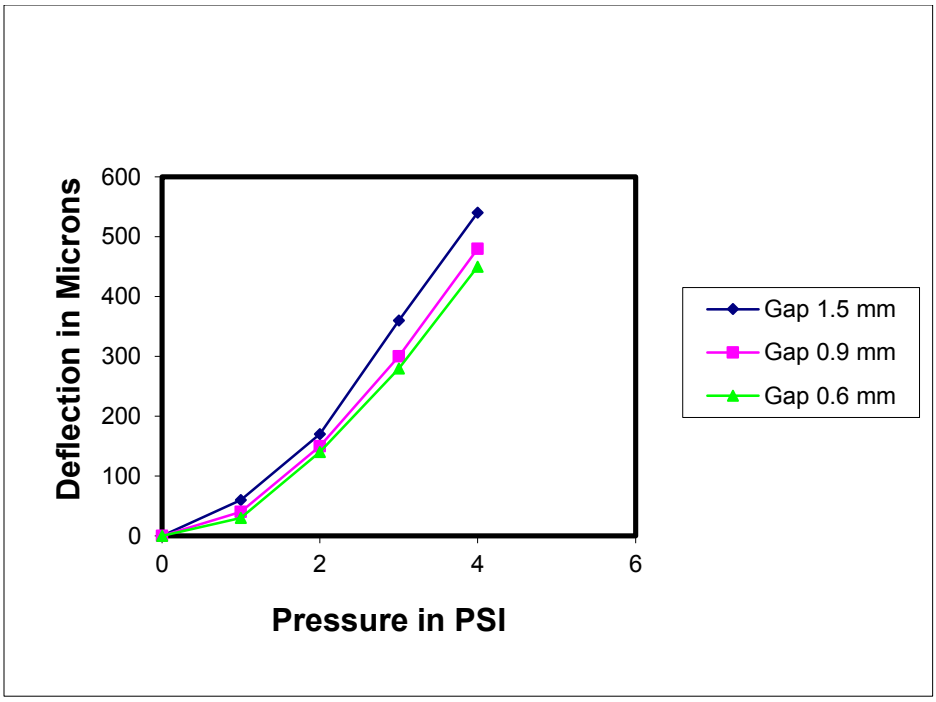

Figure A.1: Variation of *SE* deflection versus duct pressure [10].

A.2. Flow governing equations

The governing equations are written as [33]

Continuity equation

$$\frac{\partial \rho}{\partial t} + \vec{\nabla} . (\rho \vec{U}) = 0 \qquad \text{A.1}$$

Momentum equations

$$\frac{\partial (\rho \vec{U})}{\partial t} + \vec{\nabla} \cdot (\rho \vec{U} \otimes \vec{U}) = -\vec{\nabla} p + \vec{\nabla} \cdot \bar{\bar{\tau}} + \overrightarrow{S_M} \qquad \text{A.2}$$

Where: S_M is a user-defined source of momentum per u. volume and time (currently set to zero) and the stress tensor, τ, is given by

$$\bar{\bar{\tau}} = \mu \left(\vec{\nabla} \vec{U} + (\vec{\nabla} \vec{U})^T - \frac{2}{3} \delta \vec{\nabla} \cdot \vec{U} \right) \qquad \text{A.3}$$

Total energy equation, written in terms of the total enthalpy

$$\frac{\partial\,(\rho\,h_{tot})}{\partial\,t} - \frac{\partial\,p}{\partial\,t} + \vec{\nabla}\cdot\left(\rho\,\vec{U}\,h_{tot}\right) = \vec{\nabla}\cdot\left(k_{th}\,\vec{\nabla}\,T\right) + \vec{\nabla}\cdot\left(\vec{U}\cdot\bar{\bar{\tau}}\right) + \vec{U}\cdot\overrightarrow{S_M} + S_E \qquad \text{A.4}$$

Where h_{tot} is the total enthalpy

$$h_{tot} = h + \frac{1}{2}\,U^2 \qquad \text{A.5}$$

The term $\vec{\nabla}\cdot\left(\vec{U}\cdot\bar{\bar{\tau}}\right)$ represents the work due to viscous stresses and is referred to as the viscous dissipation. The term $\vec{U}\cdot\overrightarrow{S_M}$ represents the work due to external momentum sources and is currently set to zero.

A.3. Numerical implementation

Two analysis modules within *ANSYS Workbench 12.1* were used namely, *CFX* for fluid flow simulation and ANSYS for computing the static structure deflection.

A.3.1 Fluid flow simulation using *ANSYS-CFX*

Computational domain

The unsteady Reynolds averaged *Navier-Stokes* equations were used to model the compressible flow field around the micro sensor where air is blowing at *25°C* and is assumed to be a perfect gas with constant specific heats.

The dimensions are taken from the experimental work. The blocking element used is made of steel; it is a rectangular strip measuring *30.48 mm* long, *8 mm* wide and *2.3 mm* thick. The sensitive element used is also a rectangular strip made of aluminum and measuring *27 mm* long, *6 mm* wide and *0.038 mm* thick. There is a jet that is blowing air under several constant pressure varying from *1* to *5 psi*. The vertical distance between the jet and the blocking element is *1.143 mm* and its diameter is *3.572 mm*.

The gap between the blocking and the sensitive elements is set at three values *0.6*, *0.9* and *1.5 mm*. Figure A.2 shows the dimensions and the layout of the computational domain set around the sensor.

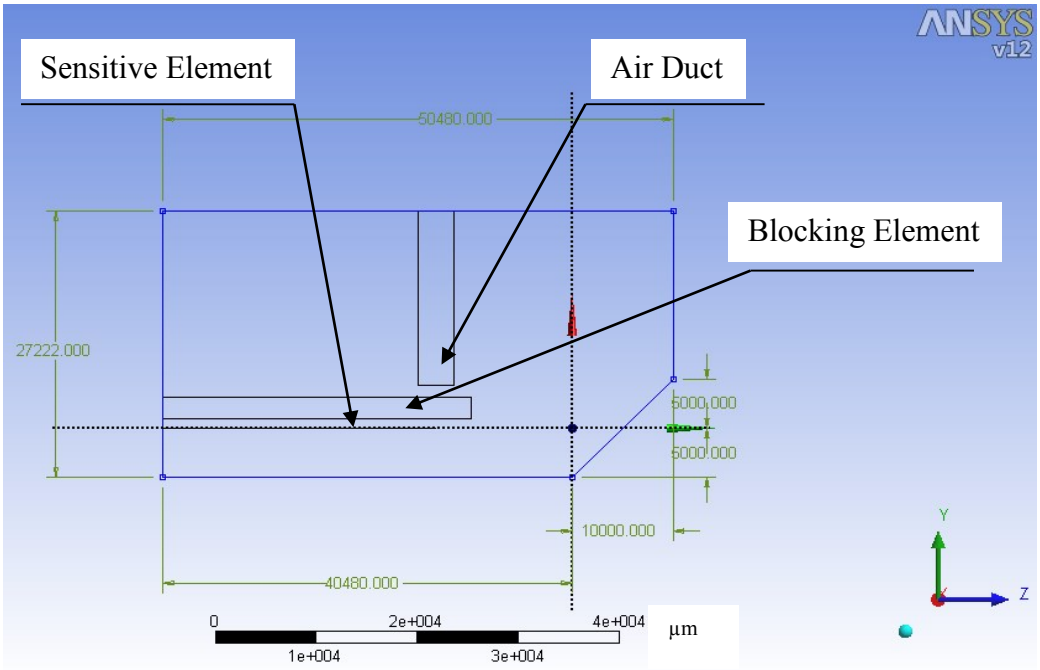

Figure A.2: The layout of the computational domain.

Mesh resolution

The computational mesh used for the fluid flow simulation contains *351* thousand nodes and *2 million* elements; the mesh skewness is used as the mesh metric with minimum *1.57* $\times 10^{-5}$, maximum *0.84*, average *0.24* and standard deviation *0.12*.

Boundary conditions

The following boundary conditions (*B.Cs.*) were used, see Figure A.3 below:

- 'No-slip' at all walls,
- 'Inflow' at the duct exit, note that the duct exit was set relatively far from the entrainment boundary
- 'Entrainment' at the top of the domain
- 'Opening' on the right of the domain and at the plane of this page, going through the blocking and sensitive elements center-line as well as through the air duct. This boundary condition allows the flow to enter and exit while keeping the global mass continuity conserved.

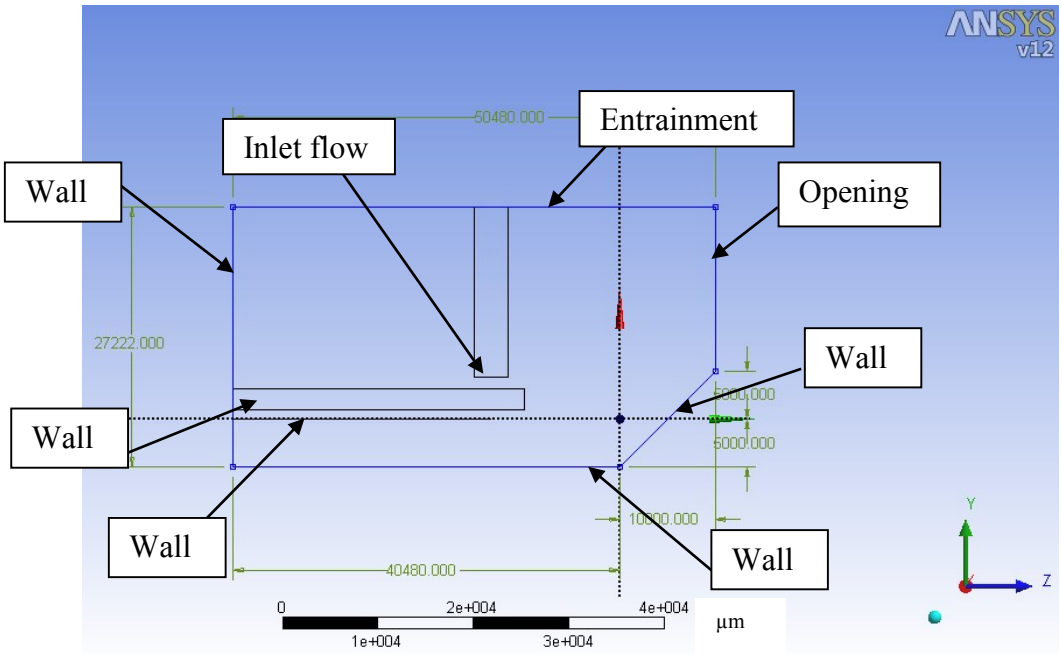

Figure A.3: Boundary Conditions.

Initial conditions and temporal resolution

In steady state cases all velocities are initialized to zero except for the vertical component of velocity at the duct exit, which is set as inlet *B.C.* In unsteady cases, the steady state results are taken as the initial value.

The solution is converged when the *RMS* of the *RANS* equations residual drops below 10^{-6} or the number of iterations exceeds a value ranging from *2,500* to *10,000* depending on the case under study.

Since the success of a turbulence model in resolving turbulence depends mainly on geometry and the expected flow features, four different turbulence models were examined. One model was based on the k-ε turbulence model. The other three models were based on the Reynolds stress models (or Second Moment Closure (*SMC*)), namely the *BSL-EARSM*, *BSL* and *SSG* Reynolds stress models. These models are chosen based on the literature survey and the *ANSYS CFX-solver* User's Guide [52].

Finally, the static pressure over the *BE* and *SE* surfaces was imported into the static structure (*ANSYS*) so as to compute the static deflection of the sensitive element.

A.3.2 The mechanical loads simulation using *ANSYS*-static structure

The materials chosen were aluminum for the sensitive element and steel for the blocking element. The structure geometry is the same as the one used in the fluid flow simulation (*CFX*) but the fluid domain is removed. The computational mesh for both *BE* and *SE* contains *208K* nodes (*33k* elements); the mesh skewness is used as the mesh metric with a minimum of 1.3×10^{-10}, maximum 7.7×10^{-9}, average 5.4×10^{-9} and standard deviation *0*. The appropriate fixations were chosen for *BE* and *SE*. The pressure was imported from the fluid flow solution (*CFX*) using interpolation. High accuracy interpolation can be obtained by resizing the upper and lower surfaces of the sensitive element. Finally the deflections of the blocking and sensitive elements were computed.

A.4. Results

Figure A.4 shows the deflection of the sensitive element versus the jet velocity for several turbulence models at a given gap of *0.9 mm* value between the blocking and the sensitive elements.

As shown in Figure A.4 all turbulence models are compared in terms of the deflection that is produced on the sensitive element at several gap heights. It is also clear from Figure A.4 that the Reynolds Stress models are more suitable for curvature streamlines than the k-ε model. Among the Reynolds Stress models, the *SSG* model seems to be more accurate than *BSL* and *BSL-EARSM*. This is based on a comparison of the computational results and the experimental data, presented in Figure A.1. Hence the *SSG* Reynolds Stress was used to model turbulence in both steady and unsteady flow cases.

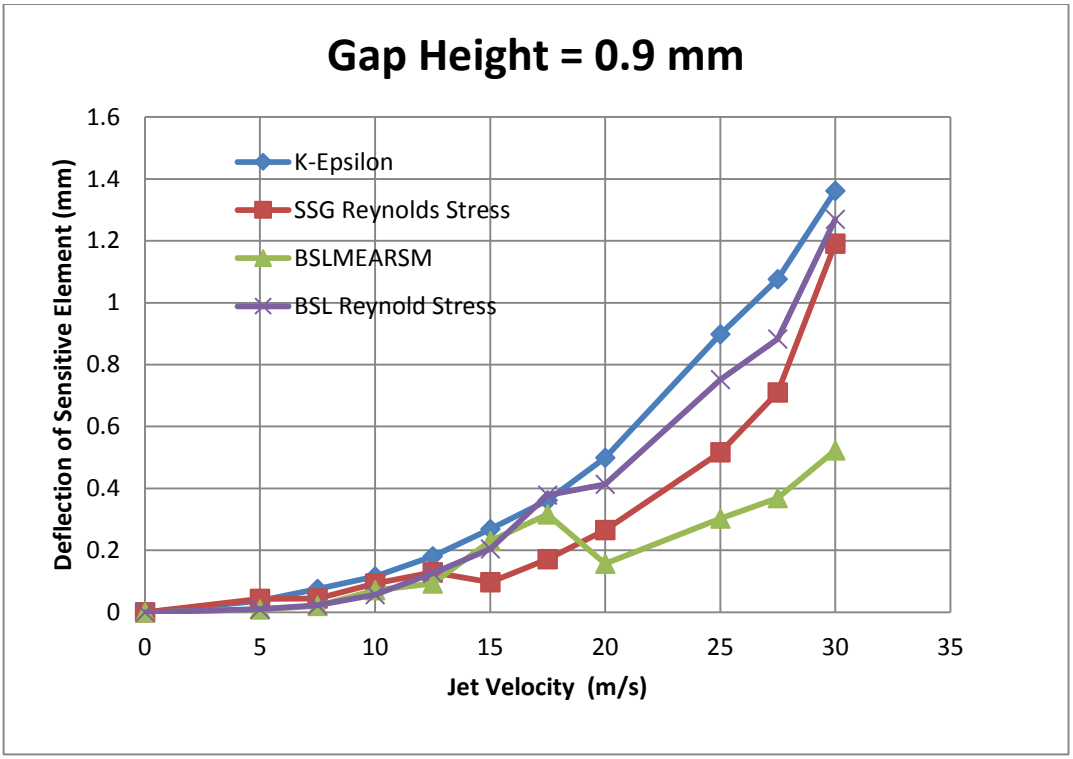

Figure A.4: Maximum deflection of sensitive element versus jet velocity.

A.4.1 Steady state

Air at *25°C* is used and is taken as an ideal gas. The deflection of the sensitive element is computed at several values of jet velocity varying from *5 m/s* to *30 m/s*.

By comparing Figure A.1 and Figure A.5, it is clear that both curves have the same trend. For the different gap heights, when the pressure in the air duct, (in Figure A.1, experiment), which corresponds to the jet velocity (in Figure A.5, numerical simulation), increases the deflection of the sensitive element increases.

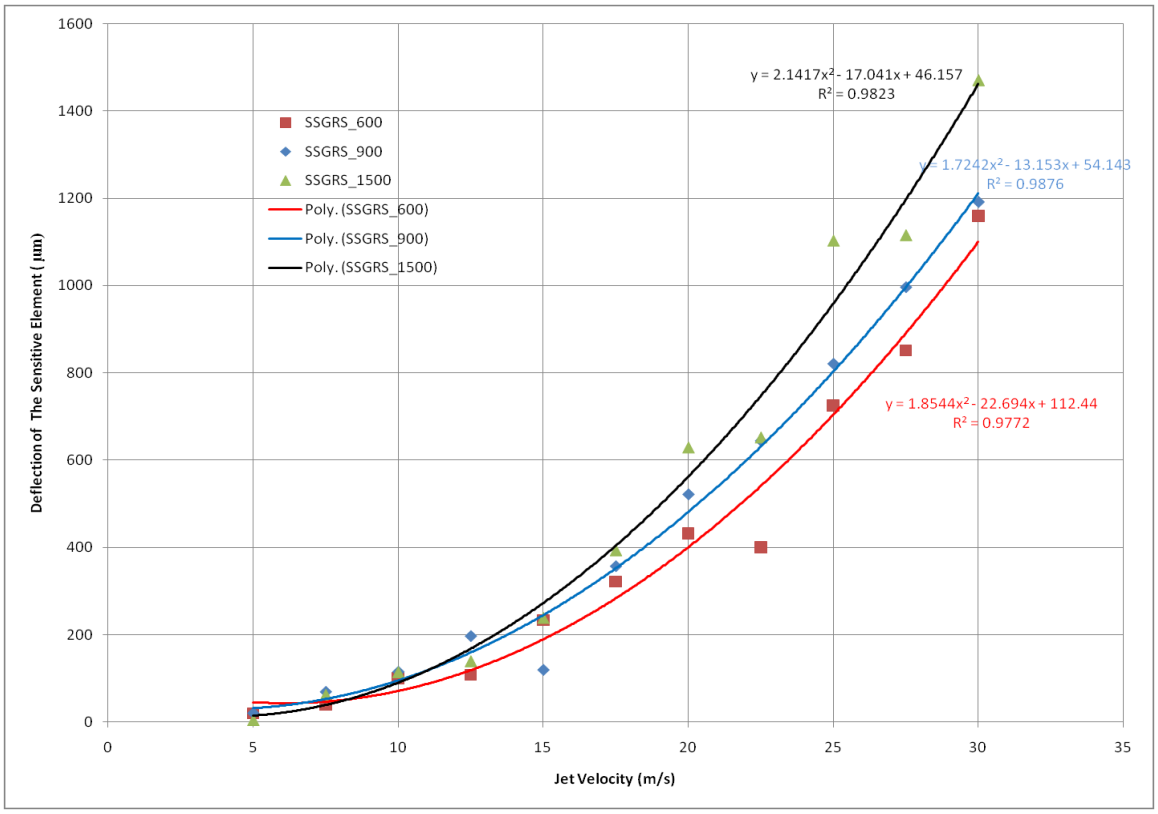

Figure A.5: Deflection of sensitive element versus jet velocity.

A.4.2 Unsteady State

Based on available information [53], the experimental work done in [10] showed that the sensitive element was undergoing a high-frequency small-amplitude fluctuation around a time average position. It is believed that this fluctuation is due to vortex shedding behind the two elements. Therefore, the flow simulations were repeated in unsteady mode to capture this vortex shedding. At the last time step of the computation, its value is 10^{-5} *s*, *RMS* of Courant number is *2.56*, and Maximum Courant number is *84.9*.

In this case seven probing points were selected in the fluid domain as shown in Figure A.6.

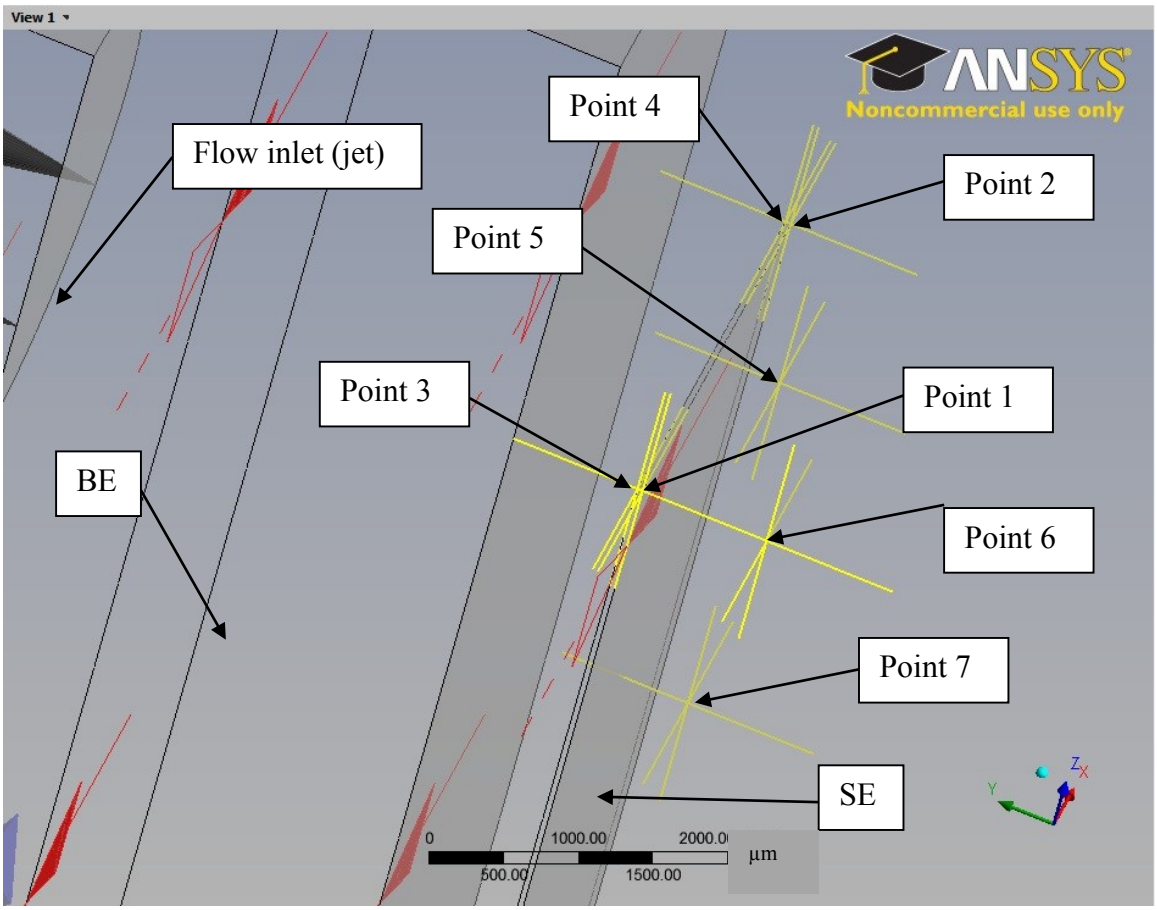

Figure A.6: Scheme of the monitoring points.

The pressure at the free boundaries is then varied from *1 atm*. to *2 atm*. and *3 atm*. The velocity at point 3 (as a sample point) is plotted versus time, as shown in Figure A.7 to Figure A.9

Both Figure A.7 and Figure A.8 have the same inlet jet velocity of *20 m/s* but the pressure at the boundary equals *2 atm*. as shown in Figure A.7 and equals *3 atm*. as shown in Figure A.8. The Mach number is equal *0.06* which is less than *0.3* meaning that the flow is effectively incompressible. It was observed that the vortex shedding frequency is the same in Figure A.7 and Figure A.8 and it equals *250 Hz*. By changing the jet velocity to *250 m/s* (i.e. Mach number equals *0.7*) the vortex shedding frequency was changed to about *450 Hz*, as shown Figure A.9 and remained the same for several pressure values. This confirms that the vortex shedding frequency is a function of Mach number, i.e. it is affected by compressibility.

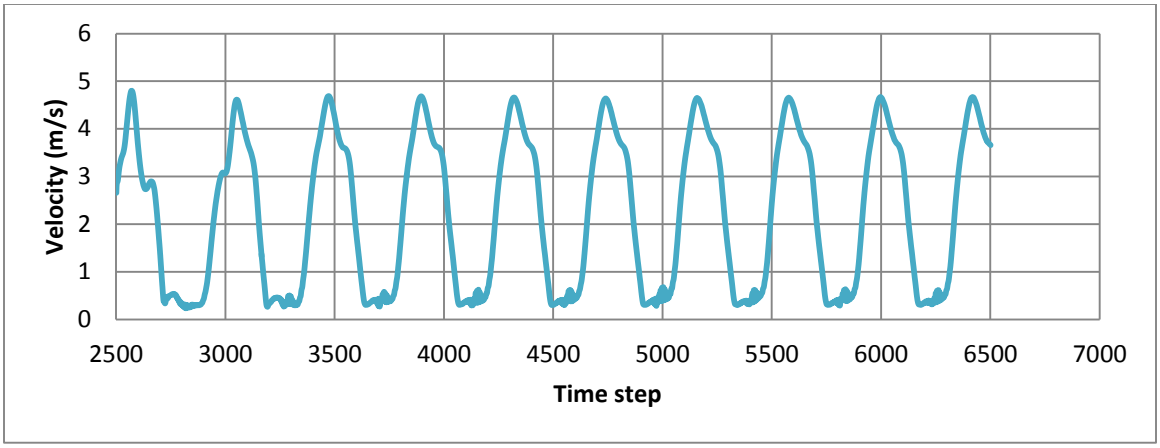

Figure A.7: Velocity at point (3) versus time for *P = 2 atm*.

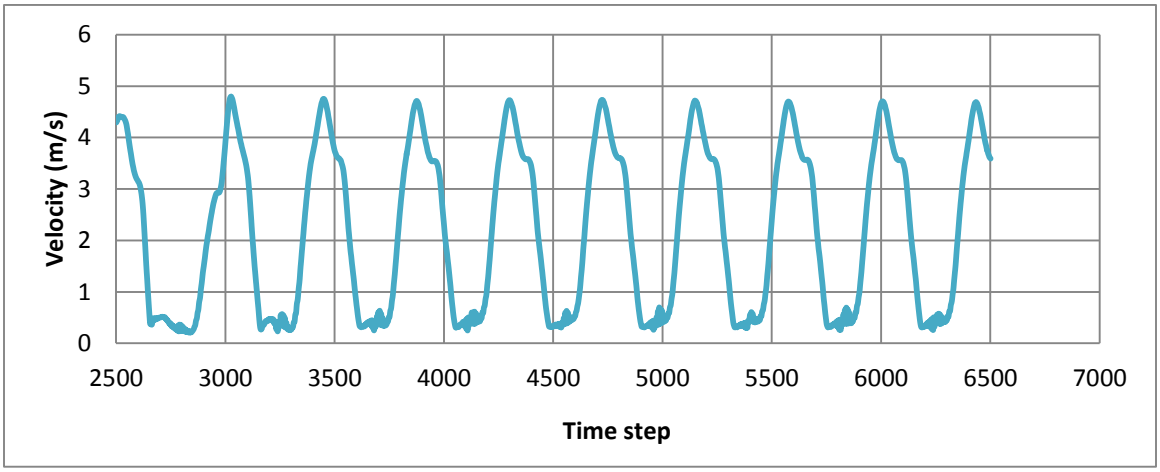

Figure A.8: Velocity at point (3) versus time for *P = 3 atm*.

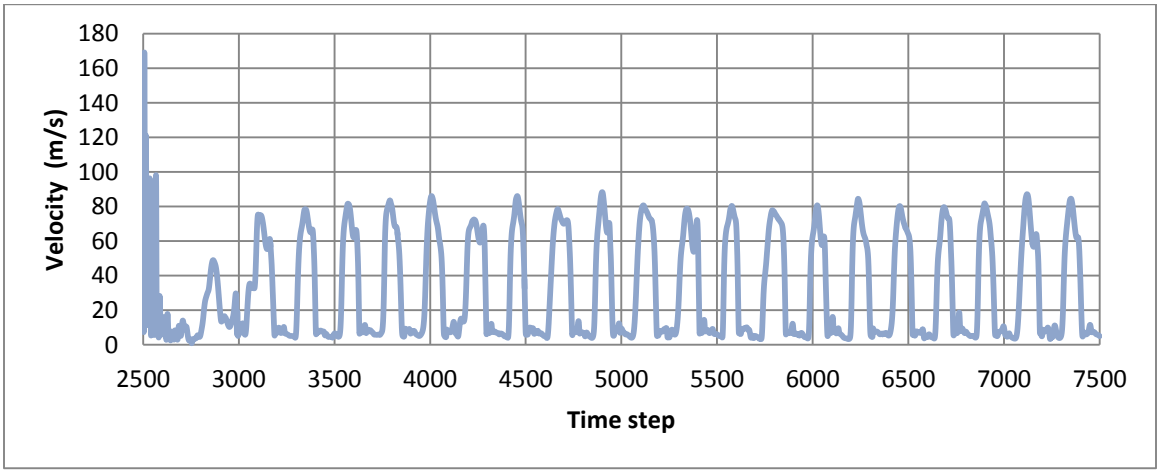

Figure A.9: Velocity at point (3) versus time for *P = 3 atm*.

Appendix B

Calculation of the boundary layer thickness

B.1. Boundary layer thickness on the two side walls in *2D* Incompressible flow

This calculation is done to ensure that there is no effect of the two sides' wall on the flow especially the wake. The calculation is done for two cases: laminar and turbulent flow over a flat plate as follows:

B.1.1 Laminar boundary layer thickness on flat plate: exact solution

The boundary layer thickness (δ) on flat plate can be obtained from [54]

$$\delta = \frac{5\,x}{\sqrt{Re_x}} \qquad \text{B.1}$$

The maximum value of δ occurs at the maximum value of x, i.e. at the plate trailing edge where $x = 23h = 9.2\times10^{-4}m$ and $U=U_\infty=177.6\ m/s$ hence

$$Re_x = \frac{U\,x}{\nu} = 163392 \qquad \textbf{B}\text{B.2}$$

So

$\delta = 1.138 \times 10^{-5}\ m = 0.28h$ for each side wall.

B.1.2 Turbulent boundary layer thickness on a flat plate

The boundary layer thickness (δ) on a flat plate can be obtained from [54]

$$\delta = \frac{0.382\,x}{Re_x} \qquad \text{B.3}$$

The maximum δ occurs at the trailing edge where x is maximum, i.e. at $x=9.2\times10^{-4}m$ hence $\delta=3.19\times10^{-5}m=0.8h$ for each side wall.

B.1.3 Conclusion

It is clear from the calculation that the boundary layer thickness is very small with respect of the size of the computational domain in the z-direction. Therefore there is no effect of the wall on the flow or vortex shedding.

This calculation is done to investigate the effect of a flat plate boundary layer on the flow especially before the cubes. In the flow over a cube (3D flow case), the boundary layer calculation is done only for the laminar flow case since the highest Reynolds number is 2000.

B.2. Laminar boundary layer thickness on flat plate for 3D compressible flow: exact solution

The boundary layer thickness (δ) on flat plate can be obtained from equation B.1. The maximum δ is at maximum x. x is maximum at $x = 10h = 10 \times 40 \times10^{-6}\ m$. For Mach number equals *0.25*, $U=U_\infty=100\ m/s$ and for Mach number equals *0.5* and *0.75*, $U=U_\infty=300\ m/s$.

Table B.1 lists the changes in ν corresponding to several pairs of Mach-Reynolds numbers.

Table B.1: Kinematic viscosity of air at all cases.

Re	*M*		
	0.25	0.5	0.75
500	0.000008	0.000024	0.000024
1000	0.000004	0.000012	0.000012
2000	0.000002	0.000006	0.000006

And from equation B2 the Reynolds number (Re_x) is

Table B.2: Reynolds number for all cases.

Re	*M*		
	0.25	0.5	0.75
500	5.00E+03	5.00E+03	5.00E+03
1000	1.00E+04	1.00E+04	1.00E+04
2000	2.00E+04	2.00E+04	2.00E+04

Hence, the boundary layer thickness (δ) is

Table B.3: Boundary layer thickness for all cases.

Re	*M*		
	0.25	0.5	0.75
500	2.83E-05	2.83E-05	2.83E-05
1000	2.00E-05	2.00E-05	2.00E-05
2000	1.41E-05	1.41E-05	1.41E-05

And for a ratio relative to the cube height, it is

Table B.4: Boundary layer thickness relative to the cube height for all cases.

Re	*M*		
	0.25	0.5	0.75
500	0.71	0.71	0.71
1000	0.50	0.50	0.50
2000	0.35	0.35	0.35

B.2.1 Conclusion

It clears from the calculation that the boundary layer thickness is mainly dependent on the Reynolds number. For *Re=500* the boundary layer thickness is the largest one of all cases and it equals *0.71h*. As the Reynolds number increases to *1000 then 2000,* the boundary layer thickness decreases to *0.5h* and *0.35h*.

Appendix C

Calculation of soap film flow velocity

This appendix presents the calculation of the soap film velocity in detail. As mentioned in section 2.5.2 the vortex lines are material lines, therefore the flow velocity can be estimated reasonably well from the vortices advance velocity by importing sequential images taken by a high-speed camera at *1ms* interval, into *AutoCAD*. As shown in Figure C.10, the center of each vortex core is determined by drawing a circle with fixed radius. This circle is then moved till it includes a high percentage of vortex (i.e. large bright area of each vortex). In these images each vortex core (circle center) is traced and the distance between its old and new positions is measured. So the velocity of each vortex core is calculated by dividing the distance between the two positions by *1ms*. The above-mention process is repeated for several times and the resulting velocities are averaged out to eliminate possible errors.

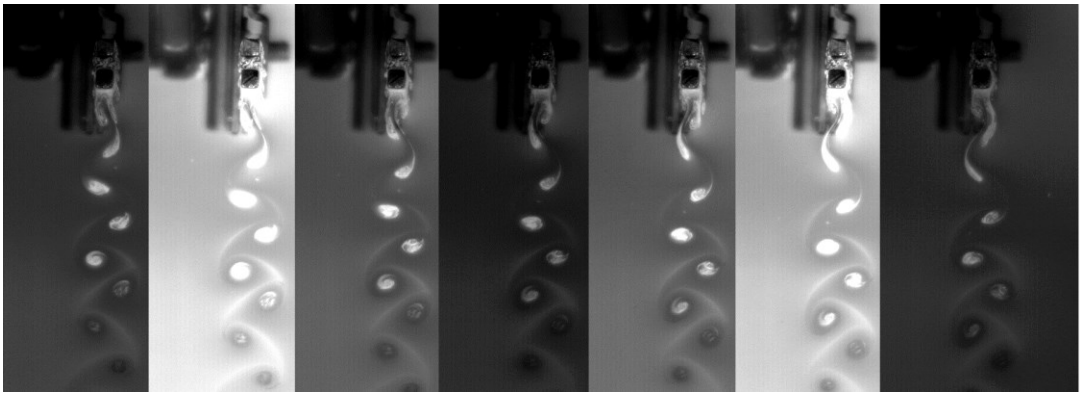

Figure C.10: Sequential images taken by a high-speed camera at 1ms interval.

Appendix D

Calculation of the flow variables for the cases given in Table 4.2

In this appendix, the calculation of the dimensional quantities involved in computing several variables and properties are described in detail.

Table 4.2 gives the Reynolds and Mach numbers for the cases considered in Chapter 4, where the cube side is set to $h=40\mu m$. Starting from this information, the following steps are executed to compute some necessary variables.

- Assume a value for the inlet flow velocity.
- Given Reynolds and Mach numbers, compute the kinematic viscosity (v) and the temperature (T), respectively.
- Given T, find the dynamic viscosity (μ) from property tables.
- Compute the density $\rho = \mu / v$, and the pressure (P) from the equation of state.

In these computations, the following values and definitions were used.

The Mach number is defined as:

$$M_\infty = \frac{U_\infty}{a_\infty} = \frac{U_\infty}{\sqrt{\gamma\, R\, T}} \qquad \text{D.1}$$

Where γ is the specific heat ratio namely, C_p/C_v ($\gamma_{air} = 1.4$), R is the gas constant ($R=287J/Kg.K$ for air), and T is the inlet flow temperature.